Charge transport in disordered organic semiconducting dendrimers studied by space-charge-limited transient currents

Marek Zdzislaw Szymanski

THÈSE

Pour obtenir le grade de

DOCTEUR DE L'UNIVERSITÉ DE GRENOBLE

Spécialité : **Physique de la matière condensée et du rayonnement**

Arrêté ministériel : 7 août 2006

Présentée par

Marek Zdzisław Szymański

Thèse dirigée par **David Djurado**

préparée au sein **du Laboratoire d'Electronique Moléculaire Organique & Hybride, INAC/SPrAM (UMR-5819), CEA Grenoble**
et de **l'Ecole Doctorale de Physique de Grenoble**

Charge transport in disordered organic semiconducting dendrimers studied by space-charge-limited transient currents

Thèse soutenue publiquement le **15 novembre 2012**,
devant le jury composé de :

M. Alasdair Campbell
Senior Lecturer of Imperial College London, Rapporteur
M. Gilles Horowitz
Professor of Ecole Polytechnique, Rapporteur
M. Beat Ruhstaller
Professor of Zurich University of Applied Science, Examinateur
M. Jean-Pierre Travers
Directeur de recherche CNRS, CEA Grenoble, Examinateur
M. David Djurado
Directeur de recherche CNRS, CEA Grenoble, Directeur de thèse

Summary: The thesis concerns space-charge-limited transient current measurements in thin (≤ 500nm) organic films. Such films find important applications in organic electronics, where they are referred to as organic semiconductor layers. Electrical transport in such films depends on bulk charge carrier transport and trapping, as well efficiency of charge carrier injection from electrodes. These, are all in turn depend on disorder inherent to organic materials. The transient measurement approach is very attractive, as it can, in principle, deliver information on all these aspects in one single measurement. In the thesis, three main contributions are presented: 1) A transimpedance amplifier based setup for space-charge-limited current transient measurement is validated. This type of setup is superior to the widely used bridge circuit, notably because of better current sensitivity, bandwidth, no need for bridge symmetry and no need for per sample adjustment. It is demonstrated that initial displacement current spike, which saturates the amplifier at the beginning of measurement, does not introduce error in the measurement of mobility. 2) A dendrimer molecule has been investigated. Experimental current responses are shown to be in agreement with the drift-diffusion model. However, obtaining agreement requires well defined initial conditions in experiment as well as in simulation, and also complete theoretical model of the sample. In the case of dendrimer, this model had to take into account both contact barrier and trapping effects. Furthermore, better agreement was obtained when taking disorder effects into account. 3) The impossibility of obtaining any agreement without complete physical model of the sample indicates that trapping, contact barrier and mobility parameters could be fitted without ambiguity. Therefore, complete electrical characterization consistent with simulation can be obtained using the transient technique. The results obtained further increase well known usefulness of transient space-charge-limited current characterization of thin organic films.

Résumé : La thèse porte sur les mesures de courants transitoires limités par la charge d'espace dans des films minces organiques (épaisseur < 500 nm). Ce type de films est souvent utilisé dans des applications dans le domaine de l'électronique organique comme couches actives semi-conductrices. Le transport électrique dans ces films dépend en premier lieu du transport des porteurs de charge dans le milieu massif et de leur piégeage, mais aussi de l'efficacité de l'injection des porteurs de charges à partir des électrodes métalliques. L'ensemble est de plus conditionné par le taux de désordre inhérent aux matériaux organiques. L'approche qui consiste à utiliser la mesure de courants transitoires est extrêmement attractive car elle permet en principe de fournir une information sur tous ces aspects à l'issue d'un seul type de mesure. Dans ce cadre, trois contributions principales peuvent être dégagées de la thèse : 1) Tout d'abord, nous avons validé un montage expérimental qui utilise un amplificateur à transfert d'impédance pour la mesure des courants transitoires limités par la charge d'espace. Ce type de montage s'avère supérieur au circuit de pont électrique le plus largement utilisé jusqu'à maintenant car il présente une meilleure sensibilité en courant, une meilleure bande passante, et ne nécessite aucun réglage ni de la symétrie du pont ni de l'ajustement de la taille de l'échantillon. On a pu démontrer que le pic de courant de déplacement initial, qui sature l'amplificateur au tout début de la mesure n'introduit pas d'erreur dans la mesure de la mobilité. 2) Ensuite concernant l'étude plus spécifique du transport dans un dendrimère à base de tri-arylamine, les réponse en courant obtenues expérimentalement se sont avérées en bon accord avec le modèle de déplacement-diffusion. Cependant, la troisième leçon que nous avons apprise est que l'obtention d'un tel accord a nécessité que soient très bien définies les conditions initiales tant de l'expérience que de la simulation et qu'un modèle théorique le plus complet possible de l'échantillon soit considéré. Pour le dendrimère ce modèle a dû prendre en compte l'effet de la barrière au contact et les effets de piégeage. Un accord encore meilleur a été obtenu en intégrant de surcroit les effets de désordre. 3) La complète impossibilité d'obtenir un bon accord sans un modèle physique complet de l'échantillon indique que les paramètres liés au piégeage, à la barrière au contact et à la mobilité peuvent véritablement être ajustés sans aucune ambigüité. Ainsi, une caractérisation électrique complète en cohérence avec la simulation a pu être obtenue à l'issue d'un seul type de mesures. Les résultats obtenus, alliant à la fois amélioration technique et support numérique, témoignent de la grande utilité de cette technique de mesure de courant transitoire limité par la charge d'espace pour caractériser en détails le transport dans les films minces organiques.

Charge transport in disordered organic semiconducting dendrimers studied by space-charge-limited transient currents

Marek Zdzisław Szymański

This thesis is dedicated to my parents :
my mother Irena and the memory of my father,
Aleksander Bożymir.

Contents

Résumé de la thèse

Dans le domaine dénommé généralement l'électronique organique, on peut distinguer un courant qui se propose en particulier de développer des nouveaux dispositifs optoélectroniques, en particulier des écrans et des cellules photovoltaïques. Une des motivations serait un cout de fabrication par unité d'aire nettement plus bas que pour les dispositifs conventionnels. Egalement, ces dispositifs peuvent présenter des caractéristiques attractives pour leur utilisation quotidienne telle que par exemple une bonne flexibilité mécanique.

Dans ce but, une intense activité de recherche est aujourd'hui concentrée autour des matériaux organiques électroniques et des dispositifs prototypes. Une grande partie des contributions scientifiques concerne donc la synthèse de ces matériaux, ainsi que leur mise en œuvre. En parallèle, un effort constant est fait pour améliorer l'élaboration de modèles physiques du transport dans les matériaux organiques. Malheureusement, il existe encore trop peu de connexions entre ces deux champs de recherche réclamant des expertises différentes. Les théories physiques sont ainsi vérifiées et développées sur la base d'un nombre plutôt faible de matériaux parmi les plus connus. L'analyse des propriétés observées s'arrête encore trop souvent aux concepts physiques de base. Ceci bien sûr s'explique par le degré de complexité des solides organiques et le caractère inévitablement pluridisciplinaire que leur approche réclame.

Dans cette thèse, l'effort produit pour contribuer à l'électronique organique ne se situe ni au niveau de l'étude de nouveaux matériaux ni sur celui du développement de la théorie du transport, mais cherche à simplifier l'utilisation d'une des techniques les plus puissantes de mesure du transport et à rendre disponible un plus grand nombre d'options pour l'analyse des données. De cette manière, nous espérons que la technique améliorée sera plus facile à mettre en œuvre et permettra plus aisément de vérifier les modèles physiques existants en donnant accès à des paramètres physiques fondamentaux permettant de mieux comprendre les performances des dispositifs mais qui ne sont pas directement mesurables. En retour, notre démarche peut aider à l'optimisation des matériaux et de leur mise en œuvre.

La technique expérimentale dont il est question est celle de la mesure de courants transitoires limités par la charge d'espace (aussi connue sous le nom de mesure transitoire de l'injection en obscurité). C'est une des nombreuses techniques utilisées pour la caractérisation électrique des matériaux organiques mais est sans doute une des moins populaires[1]. Ses propriétés uniques apparaissent rapidement quand on la compare à d'autres techniques bien connues. Jusqu'à présent, elle a surtout été utilisée pour la mesure de la mobilité des

porteurs et la caractérisation de l'efficacité des contacts. En effet, comme cette technique permet d'obtenir une bonne estimation de la mobilité qui soit relativement peu affectée par l'efficacité des contacts, elle commence maintenant à être plus largement appliquée aux films organiques minces. A ce titre elle pourrait devenir une technique de caractérisation standard de ces matériaux. Cependant, les mesures de courants transitoires ne sont pas triviales car elles comportent des difficultés expérimentales importantes. A cause de cela, récemment dans la littérature des questions sont apparues quant à la pertinence et la précision réelle de cette méthode ainsi que sur le degré d'accord des résultats qu'elle fournit avec les prédictions théoriques [2].

Il faut d'abord considérer, qu'en dépit du caractère crucial que revêt la détermination de la mobilité des porteurs de charges, les performances des contacts sont tout aussi cruciales dans la détermination de celles des dispositifs. Jusqu'à présent, il n'existe pas à notre connaissance de technique de mesure admise définitivement ainsi qu'une approche théorique pour traiter de cette question. Puisque l'interface est enterrée en dessous de l'électrode, elle n'est pas directement accessible pour l'étude. Des performances parfois très différentes de celles prédites à partir de mesures spectroscopiques comme l'UPS peuvent être ainsi obtenues. La voltamétrie cyclique, technique d'électrochimie, souvent utilisée pour prédire le caractère ohmique des contacts est en fait non justifiée pour cette application et utilisée à mauvais escient [3]. Donc, au delà de la mesure de la mobilité, la possibilité d'une caractérisation quantitative et prédictive de ces interfaces revêt une grand importance.

La thèse s'ouvre sur deux chapitres en forme de revues.

Le chapitre 1 reprend l'approche de base du transport de porteurs de charge dans les matériaux organiques semi-conducteurs. Ces matériaux sont de manière intrinsèques des isolants, du fait qu'ils présentent une concentration négligeable de porteurs libres. Il est cependant possible de générer des porteurs libres par injection à partir d'électrodes, par dopage ou encore par excitation optique[4]. Ce travail s'intéresse exclusivement au premier cas et par conséquent ce chapitre traite exclusivement de l'injection de courant dans les isolants. Il introduit d'abord le modèle de déplacement-diffusion et le calcul de la loi de Mott-Gurney qui peut en être déduit. Les prédictions que l'on peut tirer de cette loi analytique négligeant la diffusion sont ensuite comparées avec des simulations qui prennent en compte la diffusion. Cela permet de cerner les limitations de l'expression analytique de la loi quand on considère précisément les matériaux organiques semi-conducteurs. Ensuite, toujours dans ce chapitre, la théorie qui néglige le désordre est présentée mais les effets du piégeage et de la barrière au contact sont considérés et leur influence sur les caractéristiques courant tension est discutée. La partie la plus grande de ce chapitre est consacrée à l'examen de la réponse transitoire en courant de films organiques fins. Un traitement théorique simple de ces réponses transitoires

est proposé. Des résultats de simulation des réponses transitoires affectées par l'effet de pié-geage et de la barrière au contact sont aussi présentés. On en conclut que caractériser les matériaux organiques en utilisant des techniques transitoires permet d'éviter de nombreux problèmes par ailleurs associés aux mesures courant-tension stationnaires.

Le chapitre 2 est dédié à une revue plus détaillée de l'influence des mécanismes microsco-piques du transport sur ses propriétés mesurées macroscopiquement. En général on s'accorde pour dire que le transport procède par sauts entre états localisés. Parmi les multiples théo-ries, celle du modèle du désordre Gaussien de Baessler et ses extensions s'est montré capable d'expliquer et d'unifier les observations expérimentales à la fois dans les matériaux molécu-laires et les polymères. Dans ce chapitre, ce modèle est donc d'abord introduit. Il est connu que ce modèle prédit l'influence de la température et du champ électrique sur la mobilité des porteurs dans les matériaux organiques dans l'approximation d'un porteur de charge unique. Or, cette approximation n'est pas bonne dans les conditions de limite par la charge d'espace. Cela nous amène à discuter des effets de remplissage des états des bords de la densité d'états Gaussienne. A ce point, nous introduisons la relation entre la densité de porteurs de charge et la mobilité en adoptant une approche qui utilise les équations maitresses. Un autre point im-portant que nous soulevons, est que dans le cas d'une densité d'états Gaussienne, une version généralisée de la relation d'Einstein doit être utilisée et nous discutons aussi ce point. Enfin, on explique comment la notion de désordre permet un traitement plus détaillé de l'injection des porteurs de charge aux électrodes en posant les conditions de l'équilibre thermique local.

Le modèle de déplacement-diffusion introduit au chapitre 1, même dans sa forme la plus simple ne peut pas être résolu analytiquement. Les simplifications qui pourraient permettre de le faire peuvent déboucher sur des erreurs significatives. Ainsi, nous avons été amenés pour cette thèse à développer un outil de simulation numérique. Cet outil est capable de ré-soudre des problèmes tant stationnaires que transitoires, prenant en compte tous les modèles de contact, de piégeage et de mobilité développés dans les chapitres précédents 1 et 2. Les approches possibles pour la simulation du transport électrique dans les solides organiques, ainsi que la conception du simulateur sont décrits dans le chapitre 3. Le simulateur permet de résoudre de manière couplée les équations du transport et l'équation de Poisson, en utilisant le procédé de discrétisation de Scharfetter-Gummel. Cette méthode [5] fait appel à une inter-polation exponentielle de la concentration des porteurs de charges entre les nœuds du la grille de simulation. C'est un moyen d'assurer le signe positif de la concentration des porteurs et d'assurer un profil abrupt du gradient de concentration dans les dispositifs sans nécessiter le recours à une grande densité d'échantillonnage pour la grille de simulation. L'ensemble résul-tant d'équations non linéaires est alors résolu en utilisant la méthode de Raphson-Newton à l'aide d'un Jacobien analytique. L'échantillonnage temporel est assuré par la méthode impli-cite d'Euler. Cet échantillonnage peut être automatiquement réglé, en utilisant une approche

"Proportionnel Intégrale Dérivé". C'est très pratique pour les simulations transitoires avec les effets de pièges, car l'impulsion initiale de courant est suivie ensuite par une longue décroissance du courant qui ne varie que très peu en amplitude. Le simulateur a été écrit en langage Python en utilisant PySparse pour la résolution des matrices creuses.

La partie totalement originale de la thèse est contenue dans les chapitres4, 5 et 6.

Le chapitre 4présente en détails les conditions expérimentales utilisées pour les mesures de courants transitoires. De grandes difficultés expérimentales proviennent directement de la capacité géométrique de l'échantillon. Afin de minimiser ces effets, le circuit en pont est fréquemment utilisé. Ceci permet effectivement de soustraire la contribution capacitive du courant de déplacement du signal total mesuré, ce qui rend plus facile l'identification du pic en courant limité par la charge d'espace. Nous avons pour notre part développé une approche plus simple faisant appel à l'utilisation d'un amplificateur à transimpédance. L'amplificateur à transimpédance convertit directement en tension le signal mesuré en courant. Ceci permet, et c'est de la plus haute importance, d'éviter toute introduction de résistance en série dans le circuit. Cependant, cette méthode est aussi affectée par la contribution de courant de déplacement. Cette contribution capacitive va provoquer une condition de surcharge de l'amplificateur, qui potentiellement peut conduire à un temps mort expérimental et peut être à une distorsion du signal de sortie. Dans ce chapitre on montre en particulier en s'appuyant sur une mesure des caractéristiques d'un semi-conducteur organique bien connu dans le domaine (le PCBM dérivé du fullerène C60) que ces effets n'empêchent pas la mesure. La position temporel du pic est indépendante du type d'amplificateur à transimpédance utilisé à performances équivalentes par ailleurs. Ainsi, l'approche que nous proposons s'est avérée fiable pour permettre l'extraction de la valeur de la mobilité dans le matériau. On peut également souligner que cette approche basée sur l'utilisation d'un amplificateur à transimpédance, comparée à celle utilisant un pont, supprime le besoin d'ajuster spécifiquement la taille de l'échantillon tout en offrant une meilleure sensibilité en courant, et même en permettant des mesures plus rapides. Ceci est d'autant plus intéressant qu'il a été montré que cet ajustement nécessaire de l'échantillon était une des sources principales d'imprécision de la méthode utilisant un pont [2].

Une fois cette approche expérimentale validée, nous l'avons utilisée pour caractériser le transport des trous dans un dendrimère à base de triarylamines nouvellement synthétisé par nos collaborateurs en Pologne et les résultats sont reportés dans le chapitre 5. Nous avons trouvé une valeur de $8 \times 10^{-6} cm^2/(Vs)$ pour la mobilité dans ce matériau, ce qui est très proche des valeurs obtenues dans des composés similaires [6]. A cette occasion, nous avons trouvé que l'or forme des contacts quasi-ohmiques avec le dendrimère, avec une efficacité $\eta \sim 0.4$. Cette observation a été confortée dans la suite du travail quand nous avons comparé des échantillons frais et vieillis. Dans ce dernier cas, l'efficacité du contact s'avère meilleure.

Ce résultat à l'apparence surprenante a déjà été observée dans des travaux antérieurs [7, 8]. Dans le cas du dendrimère, les résultats obtenus nous incitent à attribuer ce comportement à la formation de pièges qui modifie les conditions d'injection. D'autres effets du vieillissement peuvent inclure de manière similaire l'apparition d'impuretés ioniques à l'interface, donnant ensuite naissance à un long déclin du courant (>0.1s). Ces résultats prouvent à l'envi, que l'examen de ces transitoires de courant limité par la charge d'espace ne rend pas seulement possible une caractérisation électrique complète d'un nouveau matériau, mais permet aussi de comprendre son évolution dans le temps.

En plus de cela, nous avons essayé d'observer les effets du piégeage des charges en répétant les mesures des transitoires de courant. Les résultats que nous avons obtenus sont en accord qualitatif avec des simulations, confortant ainsi les suppositions faites pour expliquer les résultats. On a trouvé que les réponses étaient bien reproductibles, si les mesures consécutives sont séparées dans le temps par un temps d'attente suffisamment long (dans notre cas c'était $\sim 0.3s$). Si cette condition est satisfaite, même des réponses à des trains d'impulsions longs et compliqués sont très reproductibles. Ainsi, on peut sans crainte procéder à un moyennage afin d'améliorer le rapport signal sur bruit même dans des expériences transitoires de type pompe-sonde, à condition que l'état initial de la mesure soit très bien défini.

La comparaison détaillée entre expérience et simulation des résultats obtenus avec le dendrimère est ensuite présentée dans le chapitre 6.Plusieurs résultats importants sont exposés. Tout d'abord on a démontré que l'état de l'art des modèles du transport dans les matériaux organiques peut reproduire les réponses expérimentales en courant limité par la charge d'espace. Un accord bien meilleur que ceux précédemment publiés [2] a été obtenu. On a montré que pour parvenir à un bon accord entre expérience et simulation, il est nécessaire de prendre en compte tous les effets pertinents. Dans notre cas, il s'est agi du transport dans la masse du matériau, le piégeage et la barrière au contact. Tout autre modèle faisant l'impasse sur un de ces effets était en désaccord clair avec l'expérience. Ainsi, tous les paramètres liés à la mobilité, les propriétés des contacts et le piégeage ont pu être extraits de l'analyse. Notons qu'en dépit d'un accord plutôt satisfaisant, les résultats des ajustements n'étaient pas parfaits en particulier en ce qui concerne le déclin aux temps longs.

Les conclusions ainsi que l'ébauche de directions futures pour ce travail sont donnés ensuite. En résumé, nous retiendrons que nous avons montré que les mesures de courants transitoires limités par la charge d'espace peuvent être techniquement simplifiées et rendues plus faciles d'utilisation en développant un montage expérimental tirant profit des performances de circuits électroniques désormais disponibles et courants. On a aussi montré que les théories disponibles pour décrire le transport dans des films organiques fins sont capables de reproduire ces expériences et que de nouvelles connaissances peuvent être atteintes grâce à l'analyse numérique des résultats des mesures de courants transitoires.

Acknowledgments

I'm am very grateful to my supervisor, David Djurado, for being the best possible PhD thesis director. David never hesitated to support my ideas and always had time for discussion. And in the mean time, we skied together Sarenne in Alpe d'Huez. It was really a great experience to meet him.

My father, Aleksander Bożymir Szymański (1933-2011), gave me the enthusiasm and the advice necessary to start this work. I would not be able to accomplish it without him. I would equally like to thank my mother, Irena Szymańska, for all her support and help.

This work was made possible by help and advice of many people. I'm not able to thank all of them, and I honestly apologize to those omitted.

I would like to thank Heinz Baessler and Leonard Tykarski for inspiring discussions. I would also like to thank my collaborators and colleagues from CEA Grenoble: Peter Reiss, Jean-Marie Verilhac, Jérôme Faure-Vincent, Benjamin Grevin, Patrice Rannou, Jean-Pierre Travers, Frederic Chandezon, Jean-Francois Jacquot and Adam Proń. Preparation of the patent application would not be possible without help of Sylvie Guillot. Irena Kulszewicz-Bajer synthetised the dendrimer material.

I'm grateful to Beata Łuszczyńska and Magda Kucińska who visited CEA Grenoble. Certainly, the time of their stay was the most interesting and productive of the whole three years.

I would like to thank my friends seen in Grenoble: Tomek Małkiewicz, Mariusz Śliwa, Maria Bacia, Anna Lisowska, Pavol Fedorko, Magda Kucińska, Jarosław Sar, Paweł Gawryś, Jacek Loska and Rasa Sukackaite. I'm specially grateful to Teresa and Jean-Claude Charbonnel who gave me a new home in St Egreve. I spent much good time with Górski family (Tomek, Beata and Dawid) and Łuszczyński family (Sylwek, Beata, Konrad). I especially thank Tomek Górski who is responsible for some of the most interesting memories of my stay in Grenoble.

I'm grateful to the people who helped me to adapt to living in France. Geneviève Ruissec guided me to say my first words in the French language. Didier from La Charette (St Egreve) introduced me to the French cuisine.

I would also like to thank my professors from the Faculty of Physics at Warsaw University of Technology, who gave me knowledge and confidence necessary to start PhD work. I thank the staff of CEA Grenoble INAC/SPrAM for the reception, and the Commissariat à l'énergie

Introduction

Organic electronics has been proposed to develop novel optoelectronic devices, in particular displays and photovoltaic cells. These are expected to be cheaper to be manufactured, per unit of area, than the conventional devices. Also, they are expected to have desirable features for everyday use, such as mechanical flexibility.

In this aim, there is intense research concentrated on organic electronics materials and devices. Most of contributions is related to material synthesis and preparation techniques. On the other hand, there is a constant improvement in the elaboration of physical models of transport in organic materials. Unfortunately, there is still only a limited connection between these two fields of research. Physical theories are verified, and developed, on rather small amount of well known materials. On the other hand, explanation of observed properties of materials is usually based on the most basic physical concepts. This is well justified by the degree of complexity of organic matter and multidisciplinary character of the work.

In this thesis, effort is made to contribute to organic electronics neither by the investigation of new materials, nor by the development of transport theory, but by simplifying the most powerful transport measurement and extending available options of data treatment. By this way, we hope that the improved technique will be easier to be applied and will permit both verification of existing physical models, as well as the estimation of fundamental physical parameters for understanding the performances of devices, but which are not directly measurable. These may in turn help in optimizing the design and processing of the materials.

The experimental technique under consideration is space-charge-limited current transient measurement[9, 10] (also known as dark injection transient measurement[11]). It is one of many techniques used for electrical characterization of organic materials, but appears to be one of the least popular (i. e. absent in ref. [1]). Its unique properties are evident in comparison with other well known measurement techniques[12]. Up to now, it has been mainly used as mobility and contact efficiency characterization technique. As this technique permits to obtain a good estimation of mobility relatively unaffected by contact efficiency, it starts to be more widely applied to thin organic films. Because of these, it could be a standard organic semiconductor (insulator) characterization technique. However, transient measurements are not straightforward, and considerable experimental difficulty is associated with it. Also, recently, some questions have been raised about the real accuracy of this method as well as the agreement of obtained results with theoretical predictions[2].

It is important to consider, that despite charge carrier mobility is considered as a critical material parameter, contact performance is equally important for device performances[3]. Up to now, it seems there is no definite measurement technique or theoretical approach to deal with this issue. As the interface is buried beneath the electrode, it is not directly accessible for investigation. Performances differing with that predicted from spectroscopic measurements(UPS) are observed[13] due to interfacial dipole formation[3]. Cyclic voltammetry, very frequently used to predict ohmic contact, is in fact unjustified for this application[3] because of different timescale of electrochemical experiment. Then, in addition to mobility measurement, possibility of quantitative and predictive characterization of such interfaces is of great interest.

As original contributions the reader may find in this thesis we can offer the following ones. In the chapter 4, it is considered if current generation of transimpedance amplifiers is suitable for space-charge-limited current transients in organic thin films. Their application can greatly simplify the measurement, but might be impossible due to initial displacement current contribution at the beginning of the measurement. Therefore, this simplified experimental design has been validated on an example of a well known material: the PCBM.

In the chapter 5, the results of the characterization of one new material (a triaryl based dendrimer) are presented. In particular, it is shown how slow evolution of the material (aging) can be further characterized by using the transient technique. Also, experimental issues that may in general cause problems with theoretical interpretation of the measurements are identified and investigated.

In the chapter 6, a detailed comparison of experimental and simulated transient responses is presented. This comparison allows to answer to the following questions: does the simple drift-diffusion theory explain the experimental results and which physical parameters beyond classical analysis can be extracted. Their values obtained from dendrimer measurements are given. Although the approach taken is completely general, the obtained results are considered as only valid for the dendrimer.

In order to accomplish data analysis, an unipolar simulator of charge carrier transport in organic materials was independently developed for the thesis based on well known models. It is detailed in section 3.

In the preceding sections, review of space-charge-limited current theory, as well as its development to account for the effects of disorder is reviewed in sections 1 and 2 respectively.Feedback

The author can be contacted by email[1]. All feedback will be appreciated.

---

[1]poczta@marekszymanski.com
mzszym@gmail.com

CHAPTER 1

Charge carrier transport in organic layers

In this section, the basic approach of charge carrier transport in organic semiconducting materials is considered. These materials are inherently insulators, because they have negligible concentration of free charge carriers. Free charge carriers can however be generated by injection from electrode, by doping or by optical excitation. This work is concerned exclusively with the first case. Therefore, in the section injected current in insulators[10] are under consideration.

1.1. Transport model

The simplest description of charge carrier transport is obtained using the so-called drift-diffusion model. Drift-diffusion equations are partial differential equations, where space is treated in a continuous way. The model is derived from Boltzmann transport equations using assumption of thermal equilibrium[14]. Therefore, the model applicability depends on the existence of quasi-thermal equilibrium and on the characteristic lengths of the problem far exceeding the size of one single molecule. It is in general difficult to take into account the possible percolative effects which may be important in transport in organic materials. Surprisingly, despite these limitations, the drift-diffusion model has been successfully applied for modeling transport in organic semiconductors[15, 16, 17, 18, 19, 20, 21]. This is partly because the effects of disorder can be taken into account in the variables occurring in the equations (i. e. mobility)[22, 23]. Neglecting molecular scale nonuniformity and percolation have been shown to cause no problem provided that the considered lengths in the problem under consideration are much greater than typical molecular sizes[19].

The drift diffusion model in its general form is composed of the following equations[10].

$$(1.1.1) \qquad \Delta\phi = -\frac{q}{\epsilon_0\epsilon_r}\left(n\right)$$

$$(1.1.2) \qquad \frac{\partial}{\partial t}\left(n\right) = -\frac{1}{q}\triangle\mathbf{j_n}$$

$$(1.1.3) \qquad \mathbf{j_n} = -q\left(D\triangle n - \mu n\triangle\phi\right)$$

5

1.1. TRANSPORT MODEL

The Poisson equation (1.1.1) relates electrostatic potential ϕ to charge carrier density n. q denotes elementary charge and ϵ_0, ϵ_r are the vacuum and relative dielectric permittivity respectively. Equation (1.1.2) establishes the charge continuity , $\mathbf{j_n}$ denotes the charge(particle) current. In (1.1.3), the electric conduction current due to the charge carrier transport is written as the sum of diffusion and drift contributions. The diffusion coefficient D is related to the mobility μ by Einstein relation.

We note that, if we assume n independent of space position, then equation (1.1.3) is reduced to the well known form

$$(1.1.4) \qquad \mathbf{j_n} = -q\mu n \mathbf{F}$$

where $\mathbf{F} = -\triangle \phi$ is the electric field. The expression $\sigma = -q\mu n$ is the electrical conductivity. However, the concept of conductivity is of little use as a macroscopic quantity if charge carrier concentration is changing. Therefore, charge carrier mobility is a much better reliable macroscopic quantity for characterizing transport properties of organic films.

In many cases, thin ($< 0.5\mu m$) layers of organic materials are sandwiched between electrodes. Normally, characteristic dimensions of electrodes are much larger than organic film thickness. In such cases, it is fully justified to simplify space dependence in the above system of equation to the one dimensional case. By assuming that the electric potential is both a function of time t and position inside sample x, the above system of equations is simplified to the following form:

$$(1.1.5) \qquad \frac{d^2\phi}{dx^2} = -\frac{q}{\varepsilon_0 \varepsilon_r}(n)$$

$$(1.1.6) \qquad \frac{\partial}{\partial t}(n) = -\frac{1}{q}\frac{\partial j_n}{\partial x}$$

$$(1.1.7) \qquad j_n = -q\left(D\frac{\partial n}{\partial x} - \mu n \frac{\partial \phi}{\partial x}\right)$$

The set of equations (1.1.5), (1.1.6), (1.1.7) is a starting point for analyzing electrical transport in thin organic films. While the above equations describe the transport inside the film, application to any physical situation requires the definition of boundary conditions. One possible choice of boundary conditions specification may be as follows:

(1.1.8)
$$\phi(x = 0) = 0$$

(1.1.9)
$$\phi(x = L) = V$$

(1.1.10)
$$n(x = 0) = n(x = L) = n_0$$

where L denotes the sample thickness, V the applied voltage and n_0 the charge carrier density at electrode.

More complex situations would require to add terms to this model for accounting for charge-carrier trapping[10] effects, dual system for transport of electrons and holes, photo-carrier creation or charge carrier recombination.

1.2. Space-charge-limited current

Let's consider the simple case of one stationary current flowing through a layer equipped with ideal ohmic contacts. As in almost all analytical treatment of drift-diffusion model, we shall start by omitting the diffusion term from equation (1.1.7). Because steady situation is considered, the particle current j_n is the observed current j. Using substitution $-d\phi/dx \rightarrow F, \frac{\partial}{\partial t} \rightarrow 0, j_n \rightarrow j$ we obtain

(1.2.1)
$$\frac{dF}{dx} = \frac{q}{\epsilon_0 \epsilon_r} n$$

(1.2.2)
$$j = q\mu n F$$

By combining above equations, we get

(1.2.3)
$$F\frac{dF}{dx} = \frac{j}{\mu \epsilon_0 \epsilon_r}$$

(1.2.4)
$$\frac{dF^2}{dx} = \frac{2j}{\mu \epsilon_0 \epsilon_r}$$

Injecting electrode at $x = 0$ is assumed to be ohmic, leading to the following boundary condition[10]

(1.2.5)
$$F(0) = 0$$

7

By taking into account this boundary condition it comes

$$(1.2.6) \qquad F = \left(\frac{2j}{\mu \epsilon_0 \epsilon_r} x \right)^{1/2}$$

The voltage drop across the sample is equal to

$$(1.2.7) \qquad V = \int_0^L F(x)dx = \left(\frac{8j}{9\mu\epsilon_0\epsilon_r} \right)^{1/2} L^{3/2}$$

From eq. (1.2.7), the well known Mott-Gurney law is then recovered

$$(1.2.8) \qquad j = \frac{9}{8}\epsilon_0\epsilon_r\mu \frac{V^2}{L^3}$$

The equation above gives the current density j flowing across a sample of thickness L upon application of voltage V. It is notable that it is proportional to the square of voltage ($j \propto V^2$) and inversely proportional to the cube of the sample thickness ($j \propto L^{-3}$). The first property ($j \propto V^2$) is universal for diffusion neglecting space-charge-limited current[24]. It is interesting to calculate space-charge density

$$(1.2.9) \qquad n(x) = \frac{1}{2} \left(\frac{L}{x} \right)^{1/2} \langle n \rangle$$

$$(1.2.10) \qquad \langle n \rangle = \frac{1}{L} \int_0^L n(x)dx = \frac{3}{2} \left(\frac{\epsilon_0\epsilon_r V}{qL^2} \right)$$

Therefore, in presence of a perfectly ohmic contact, the current flowing through the sample is limited by the space-charge buildup inside the sample.

One very important consequence of 1.2.8 is that the current density is proportional to the mobility ($j \propto \mu$). This explains the critical influence of the charge carrier mobility when considering the electric performance of a given device. Because organic materials are characterized by low mobility, the current they will be conducting in devices, in particular OLEDs, will usually be a space-charge-limited current.

When performing experimental material characterization, it is tempting to interpret obtained currents as space-charge-limited ones. Indeed, in many works, mobility is deduced by comparing observed current magnitude with formula (1.2.8). Developments of the above formula taking into account field dependent mobilities exist (i.e. [25]).

1.3. Importance of diffusion

Now, let's evaluate the importance of diffusion in conditions typical for thin organic layers. In analytical treatment of space-charge-limited current theory, diffusion term cannot be taken into account and its importance is unclear. Obviously, diffusion is important when applied voltage is less than thermal voltage ($V_T = k_B T/q$, approximately 26mV at room temperature). Also, the importance of diffusion term increases with decreasing layer thickness[10]. This is because charge concentration gradients are higher in thinner layers. Furthermore, below certain layer thickness, the assumption of well separated electrodes is questionable. Unfortunately, full treatment including diffusion can be only performed using numerical calculation.

Fig. 1.3.1 shows the impact of diffusion on current-voltage characteristics of films of thickness of 100nm and 1μm. Diffusion causes an increase of the current density for small applied voltages far exceeding that predicted by Mott-Gurney law. Current-voltage curves converge to Mott-Gurney law for higher field magnitudes. Importantly, the thinner the sample, the higher field required to obtain agreement. From the plot, it can be seen that for organic films with a 100nm thickness, neglecting diffusion causes significant error for fields lower than 10^5V/cm.

1.4. Metal-organic interface

Previously assumed ohmic contact is characterized by zero electric field at the interface(eq. (1.2.5)) and infinite charge carrier density(eq. (1.2.9)). Such a contact is an infinite reservoir of charge carriers. Obviously, this is an idealized case. Real contacts are characterized by finite charge carrier density and non zero electric field at the interface.

Currently, almost all measurements and application of organic semiconducting materials utilize electrodes made of various materials. These highly conducting materials are usually either metals, such as gold, or exhibit metal like conduction, like indium-tin-oxide or PEDOT:PSS. The performance of metal organic junction can be critical for the overall performance of the device.

The electrical properties of one junction between two materials are governed by their respective work functions, defined as the energy needed to move one electron from the Fermi level to vacuum (fig. 1.4.1)[3]. When both materials are put in contact, their Fermi levels align at the interface. This is achieved by accumulation of built-in charges on both sides of the junction.

In the case of metal-organic junctions, this simple picture may be complicated by the fact that organic material may be completely devoid of charge carriers in the first place. In such a case, its Fermi level is undefined and the concept of Fermi levels alignment is not really applicable[3].
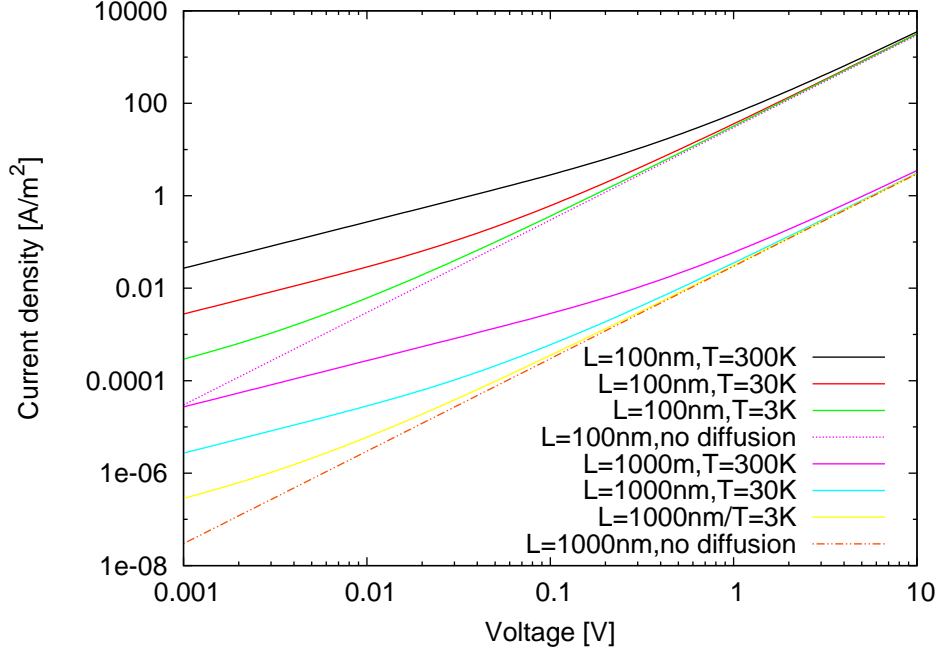
FIGURE 1.3.1. *Space-charge-limited current including and neglecting diffusion for two values of sample thickness. Assumed charge carrier mobility is $\mu = 10^{-5} cm^2/(Vs)$, dielectric permittivity $\epsilon_r = 3$. Lines described as no diffusion were calculated according to formula 1.2.8. Other curves calculated using equations (1.1.5), (1.1.6) and (1.1.7), with ohmic contact approximated by assuming $n_0 = 2.44 \times 10^{20}/cm^3$.*

Then, in order to obtain one ohmic contact it is necessary to use one electrode that would inject charge carriers into the material[10]. The contact is therefore characterized by an injection barrier, which is usually approximated as the difference between the metal work function and the state energy level (highest occupied molecular orbital (HOMO) or lowest unoccupied molecular orbital (LUMO)) to be filled in the material. Physics of metal organic junctions is in development and numerous models have been proposed[3, 26]. Problems include discrepancies between expected and obtained contact barriers, and the effects of bulk and surface states. Physically, a correct injection model must take into account effects of the image potential attracting charge carriers back to the electrode and the distribution of states inside the organic material as well(fig. 1.4.2).

Due to the image potential contribution, the electrical potential $U(x)$ in the intermediate neighborhood of the electrode is given by the following formula[27, 26]

$$(1.4.1) \qquad U(x) = \phi_B - qFx - \frac{q^2}{16\pi\epsilon_0\epsilon_r x}$$

10

where F denotes the applied electric field, q the elementary charge and ϕ_B the barrier height. Taking into account thermionic emission and surface recombination at the interface, a model of contact can be obtained[26]

$$(1.4.2) \qquad J(F) = 4\psi^2 N_0 \exp\left(-\phi_B/kT\right) \exp\sqrt{f}$$

$$(1.4.3) \qquad f = eFr_c/kT$$

$$(1.4.4) \qquad \psi = f^{-1} + f^{-1/2} - f^{-1}\left(1 + 2f^{1/2}\right)^{1/2}$$

$$(1.4.5) \qquad r_c = \frac{q^2}{4\pi\epsilon_0\epsilon_r kT}$$

Above, r_c denotes Coulomb radius and f is reduced electric field. $J(F)$ is total net injected current corresponding to the externally applied electric field F. The above model was used successfully in works concerning the study of effects of contacts[16, 17]. However, this model is not suitable for predicting equilibrium conditions for zero applied voltage, because it implies sample devoid of charge carriers in such a case. Therefore, later in the thesis, a model assuming local equilibrum conditions(section 2.4) is used exclusively.

1.5. Effects of traps

Real organic materials usually have large concentration of structural and chemical defects which are likely to act as trapping centers. Trap states are isolated localized states with low energy. Once entering a trap state, a charge carrier is immobilized until thermally excited to the transport energy[10].

In order to demonstrate the effects of trapping, we assume the existence of concentration N_t of trap states with a fixed energetic depth E_t with respect to transport energy. Existence of traps is incorporated into the model by providing the drift-diffusion equation system with a new variable, n_t, which is the concentration of trapped charges. Trapping kinematics is then given by the following equation

$$(1.5.1) \qquad \frac{dn_t}{dt} = r_t n\left(N_t - n_t\right) - r_r n_t(N - n)$$

Above r_t denotes trapping rate, r_r denotes detrapping rate and N is the density of transport states. Note that in the above equation, the following inequalities hold
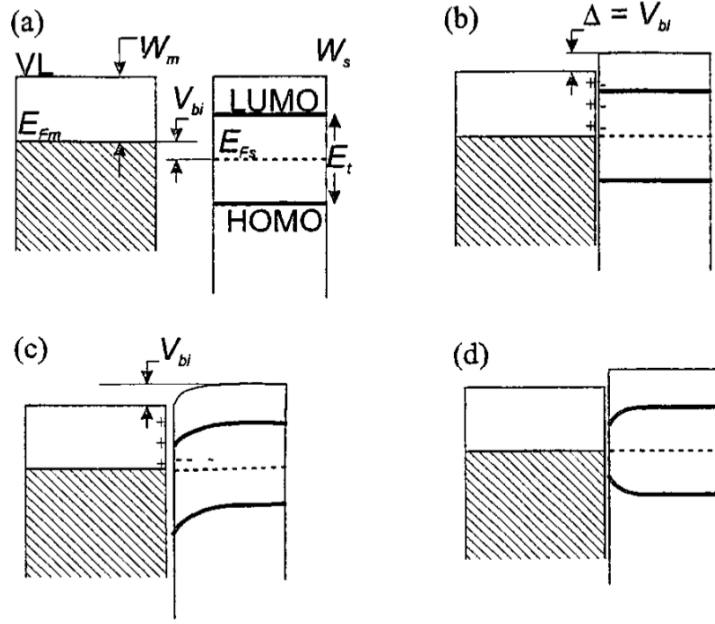
the so

FIGURE 1.4.1. *Metal insulator junction. a) Nonequilibrium situation, before contact is made. VL denotes vacuum level, E_{Fm} is metal workfunction. HOMO,LUMO denote energetic levels of localized states in organic semiconductors available for hole and electron transport respectively. b) Situation is which energy level difference is accommodated by formation of interfacial dipole layer. c) Situation in which energy level difference is accommodated by formation of charged depleted zone. d) Same as (b) including the effects of image potential. From [3].*
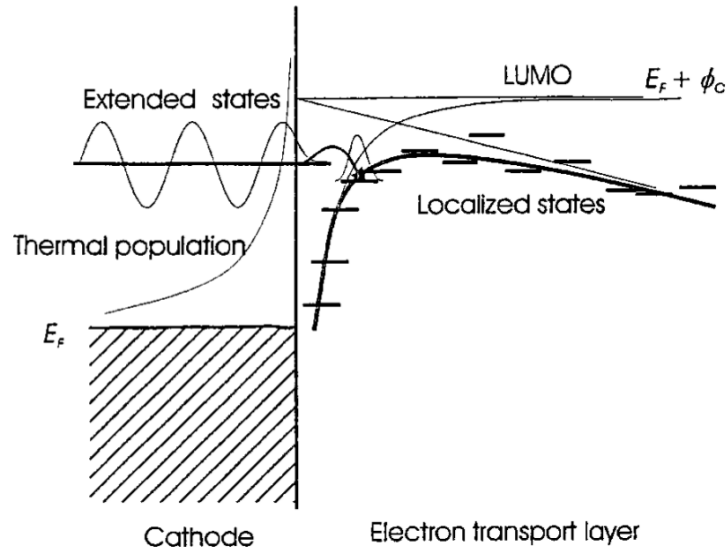

FIGURE 1.4.2. *Energetics of charge(electron) injection into organic insulator(from [3]). Charge carriers occupy extended states in metal, and localized states in organic semiconductors. Energy of localized states is determined by energetic position of molecular orbital level and potential given by eq. (1.4.1).*

(1.5.2)
$$n_t < N_t$$

(1.5.3)
$$n \ll N$$

(1.5.4)
$$N_t \ll N$$

The last relation is satisfied because trap states are isolated by definition. Using the inequality (1.5.3), approximation $N - n \approx N$ can be made in the equation (1.5.1), resulting in the simpler form

(1.5.5)
$$\frac{dn_t}{dt} = r_t n \left(N_t - n_t \right) - f_r n_t$$

where f_r is the trap release frequency

(1.5.6)
$$f_r = r_r N$$

The existence of trapped charges must be taken into account in the Poisson equation (1.1.5), which takes the following form:

(1.5.7)
$$\frac{d^2 \phi}{dx^2} = -\frac{q}{\varepsilon_0 \varepsilon_r} \left(n + n_t \right)$$

and the charge continuity equation, must be written as

(1.5.8)
$$\frac{\partial}{\partial t} \left(n + n_t \right) = -\frac{1}{q} \frac{\partial j}{\partial x}$$

Equations (1.5.7), (1.5.8), (1.1.7), (1.5.5) describe unidimensional drift-diffusion transport in presence of one trap level. Extension to take into account multiple trap levels or distribution of traps in energy is straightforward.

We should note that, in the steady state($\partial / \partial t = 0$), equation (1.5.1) is reduced to

(1.5.9)
$$r_t n (N_t - n_t) - r_r n_t (N - n) = 0$$

1.5. EFFECTS OF TRAPS

It is justified to assume thermal equilibrium. Then, Fermi-Dirac distribution function $f(E)$ can be used to express mobile n and trapped n_t charge carrier concentrations:

$$(1.5.10) \qquad f(E) = \frac{1}{1 + \exp(E - E_F)/kT}$$

$$(1.5.11) \qquad n = N f(E_c)$$

$$(1.5.12) \qquad n_t = N_t f(E_t)$$

where E_c and E_t denote conduction and trapping energy levels, respectively. E_F denotes Fermi level assuming thermal quasi-equilibrium. This means that occupation distribution of states under injection is similar to that in thermal equilibrium. This is valid for low injection level and is discussed in depth in[10]. Substitution into previous equation yields

$$(1.5.13) \qquad \frac{f(E_c)(1 - f(E_t))}{f(E_t)(1 - f(E_c))} = \frac{r_r}{r_t}$$

After calculation, the following property is obtained

$$(1.5.14) \qquad \frac{r_r}{r_t} = \exp\left[-(E_t - E_c)/kT\right]$$

. The quasi thermal equilibrium conditions links trapping and release rates by energetic trap depth $E_c - E_t$. Therefore, the influence of traps on steady state characteristics is completely described by trap concentration and trap depth. Example I-V characteristics taking trapping into account are presented in fig. 1.5.1.

Figure 1.5.1 shows sample simulation of space-charge-limited current-voltage characteristics affected by trapping. The plot reproduces some significant results from the theory of space-charge-limited currents[10]. In the case of shallow traps, the shape of current-voltage characteristics in unchanged, but current magnitude is lowered. This corresponds to a decrease of the effective mobility. Then, as trap depth increases, a region of very steep increase of current is emerging in current voltage characteristics. This region is due to trap filling. Interestingly, the height of trap filling step in the current voltage curve is directly related to the trap depth while its voltage position is directly related to the trap concentration[10].

Single trap level model, while illustrative, may be unrealistic in some cases. Various distribution of traps have been used in literature to explain observations of space-charge-limited conduction in organic materials. Very often, exponential trap density distribution gives excellent results[28, 29, 30].
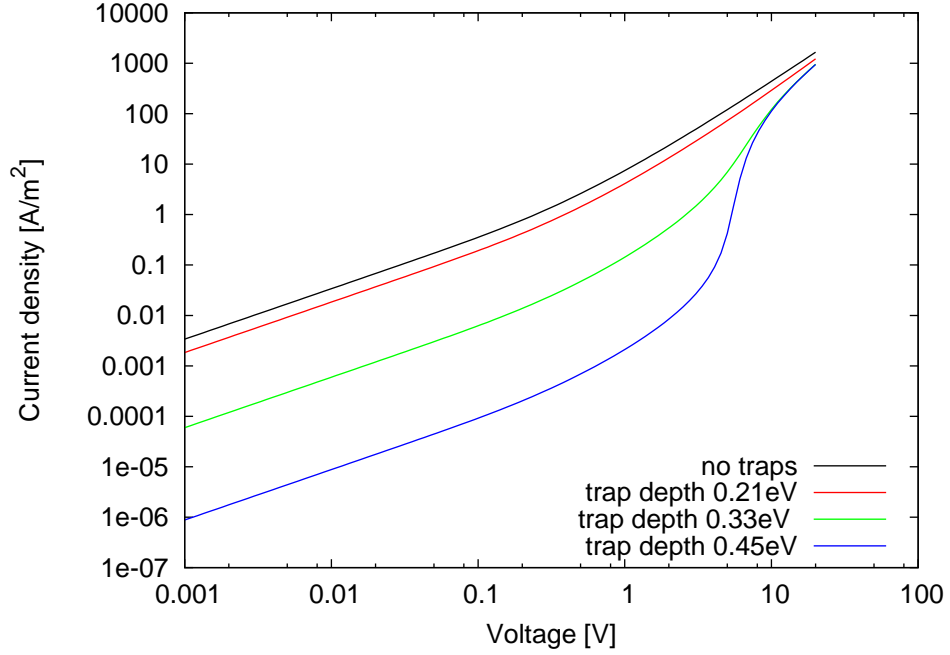
is

FIGURE 1.5.1. *Effects of traps on space-charge-limited current-voltage curve. Fixed simulation parameters are: mobility $\mu = 10^{-5} cm^2/(Vs)$, sample thickness $L = 200nm$, trap concentration $N_t = 6.2 \times 10^{16} cm^{-3}$. Room temperature and density of conduction states $N=2.4 \times 10^{20} cm^{-3}$ are assumed. Illustrated data calculated using equations (1.5.7), (1.5.8) and (1.1.7) with trapping kinematics equation (1.5.1).*

1.6. Injection-limited current

So far, the situation of space-charge-limited current was considered. Another possibility is injection-limited current, where flowing current magnitude is limited by contact efficiency. In such a case, any analysis assuming space-charge-limited situation does not apply. Injection-limited conduction takes place when electrodes does not form ohmic contacts. This happens when the injection barrier ϕ_B is high enough to prevent ohmic injection of charge carriers from the electrode to the organic layer.

Examples of injection limited current-voltage characteristics are given in fig. 1.6.1. The current is calculated using contact model given by formula (1.4.2). The different curves correspond to fixed layer parameters but for different contact barriers. It can be seen that below some value of its height, the contact barrier has no effects. This happens when the barrier height is sufficiently small with respect to the thermal energy. For higher barrier heights, the existence of contact barrier leads to a drastic decrease of the current. In presence
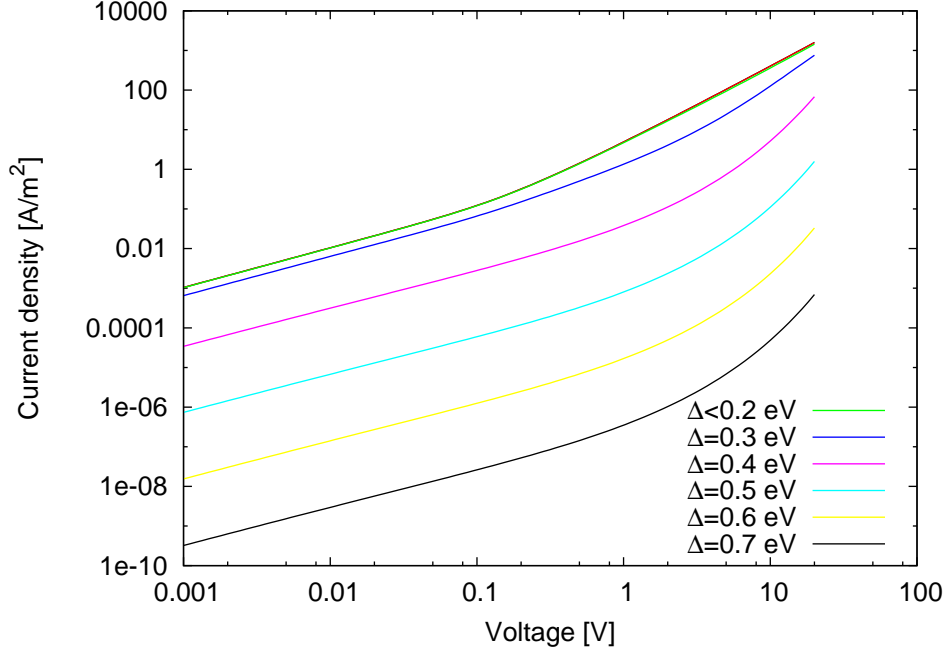
FIGURE 1.6.1. *Comparison of injection limited and space-chage-limited current, assuming charge carrier mobility is $\mu = 10^{-5}cm^2/(Vs)$, sample thickness L=200nm and dielectric permittivity $\epsilon_r = 3$. Illustrated data calculated using equations (1.1.5), (1.1.6) and (1.1.7) with charge injection from metal modeled according to model described in section 2.4.*

of a contact barrier, current would increase toward its barrier-less value in the high field region only.

Normally, presence of contact barrier is undesired for charge carrier which should be injected to the material. Unfortunately, in the organic case it is difficult to predict with complete certainty if ohmic contact will be obtained. Obtaining quasi-ohmic contact is very likely[16]. Therefore, the performance of the material or device will be degraded with respect to the purely space-charge-limited situation.

Distinguishing between space-charge-limited and injection-limited case is of great practical importance. Unfortunately, it cannot be reliable done from current voltage characteristics[17]. Injection-limited current voltage curves are similar to space-charge-limited current voltage curves corresponding to an effective mobility smaller than the material mobility.

1.7. Transient response

Very often, charge carrier mobility is the main value of interest to be obtained from current-voltage characteristics. As seen before, charge carrier mobility is generally proportional to the current magnitude, which may be affected by contact barrier and trapping in a complex way. Their effects may lead to an underestimation of charge carrier mobility. Therefore, mobility estimation from analysis of steady state current voltage curves is not regarded as reliable and different methods for mobility estimation are preferred. Additionally, from steady state current-voltage characteristics no complete information about trapping kinematics is obtained, as the shape of the curve depends only on the ratio of trapping and detrapping rates.

Reliable mobility measurement methods are based on direct measurement of charge carrier drift velocity under applied field. At relatively early stage of space-charge-limited current research[9], it was discovered that time resolved space-charge-limited current response contains signature of charge carrier drift velocity. When voltage step is applied to insulator and conditions for space-charge-limited current conduction are satisfied, time dependent current response contains peak at time close to the transit time $L^2/(\mu V)$ (fig. 1.7.1). This makes observation transient space-charge-limited current responses a very important tool for study of transport in organic insulating materials.

In order to explain this phenomena, we start by writing time resolved observed current

$$(1.7.1) \qquad\qquad j(t) = j_n(x,t) + j_d(x,t)$$

as sum of particle conduction current $j_n(t)$ and displacement current $j_d(t)$.

$$(1.7.2) \qquad\qquad j_n(x,t) = q\mu n(x,t)F(x,t)$$

$$(1.7.3) \qquad\qquad j_d(x,t) = \epsilon_0\epsilon_r \frac{\partial F(x,t)}{\partial t}$$

Total current $j(t)$ is independent of x as a consequence of Maxwell equations ($\nabla \times H = j \Rightarrow \nabla \cdot (\nabla \times H) = \nabla \cdot j \Rightarrow 0 = \partial j/\partial x$). As usual in the case of analytical treatment of drift-diffusion system, diffusion term was dropped from equation (1.7.2). Let's denote by $Q(t)$ the total charge per unit of area inside insulator at given instant of time. $Q(t)$ is related to electric field at electrodes $F_0(t) = F(x = 0, t)$ and $F_1(t) = F(x = L, t)$ by Gauss law:

$$(1.7.4) \qquad\qquad F_0(t) = F_1(t) - \frac{1}{\epsilon_0\epsilon_r}Q(t)$$

1.7. TRANSIENT RESPONSE

By combining above with Poisson equation (1.2.1), the following expression for total current is obtained:

$$(1.7.5) \qquad j(t) = \epsilon_0 \epsilon_r \left(\frac{\mu}{2} \frac{\partial F^2(x,t)}{\partial x} + \frac{\partial F(x,t)}{\partial t} \right)$$

The above is to be integrated over $x (\int_0^L (\cdot) dx)$, yielding

$$(1.7.6) \qquad j(t) = \frac{\epsilon_0 \epsilon_r \mu}{2L} \left(F_1^2(t) - F_0^2(t) \right)$$

. The above result is obtained considering a constant voltage at time $t > 0$

$$(1.7.7) \qquad \int_0^L \frac{\partial F}{\partial t} dx = \frac{\partial}{\partial t} \left(\int_0^L F dx \right) = \frac{\partial}{\partial t} (V) = 0$$

In order to demonstrate the existence of a current peak, it is sufficient to calculate the evolution of the current in function of time $j(t)$ and to compare with steady state current given by formula 1.2.8. At time $t = 0$ the layer is completely devoid of charge carriers and first carriers arrive to the electrode at time t_1. It implies that

$$(1.7.8) \qquad j_n(x = L, t < t_1) = 0$$

because before t_1 there is no charge carriers at $x = L$.
Therefore, eq. (1.7.1) evaluated at $x = L$ takes form:

$$(1.7.9) \qquad j(t < t_1) = \epsilon_0 \epsilon_r \frac{\partial F_1(t)}{\partial t}$$

Using ohmic contact assumption $F(x = 0) = 0$, eq. (1.7.6) takes form:

$$(1.7.10) \qquad j(t < t_1) = \frac{\epsilon_0 \epsilon_r \mu}{2L} F_1^2(t)$$

Combining these, the following differential equation is obtained

$$(1.7.11) \qquad \frac{\partial F_1(t)}{\partial t} = \frac{\mu}{2L} F_1^2(t)$$

The equation has separable variables and the solution is

$$(1.7.12) \qquad -\frac{1}{F_1} = \frac{\mu}{2L} t + C$$

18

1.7. TRANSIENT RESPONSE

Integration constant is obtained by noting that at time $t = 0$ voltage V is applied and layer is free of charge carriers. Therefore, $F(t = 0) = V/L$ is satisfied everywhere within the sample. After introducing transit time $t_0 = \frac{L^2}{\mu V}$, F_1 takes the following simple form

$$(1.7.13) \qquad F_1(t < t_1) = \frac{V}{L} \frac{1}{1 - (t/2t_0)}$$

Using again eq. 1.7.1 for $x = L$, leads immediately to the current magnitude

$$(1.7.14) \qquad j(t < t_1) = j_0 \frac{1}{[1 - (t/2t_0)]^2}$$

$$(1.7.15) \qquad j_0 = \epsilon_0 \epsilon_r \frac{V}{L} \frac{\mu V}{L^2}$$

By Gauss law, electric field at destination electrode $E_1(t)$ is the same as electric field at charge carrier front. Therefore, arrival time of the front t_1 is simply given by equation

$$(1.7.16) \qquad \int_0^{t_1} \mu F_1 dt = L$$

From here, value $t_1 \simeq 0.786 t_0$ is obtained. Therefore, in space-charge-limited conditions the most rapid charge carriers arrive at the target electrode at time shorter that transient time t_0 assuming linear electric field.

In order to demonstrate the existence of a peak, current magnitudes at times $t = 0$ and $t = t_1$ have to be compared with stationary current magnitude j_∞ calculated using eq. (1.2.8). This gives

$$(1.7.17) \qquad \frac{j_0}{j_\infty} = 0.5$$

$$(1.7.18) \qquad \frac{j_1}{j_\infty} \simeq 1.21$$

This proves nonmonotonic behavior of transient space-charge-limited current and existence of the current peak. More complete discussion[9] shows that the maximum occurs at time t_1.

The theory of transient space-charge-limited currents is used for mobility estimation using the formula

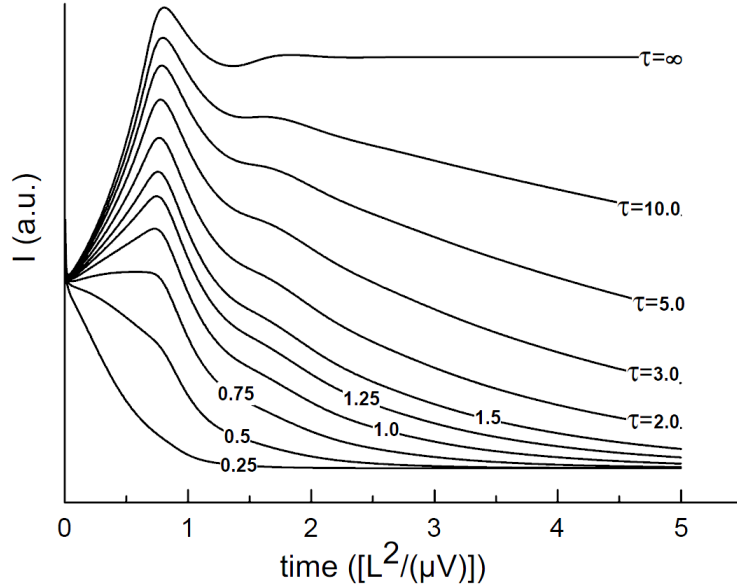$$(1.7.19) \qquad t_{max} = t_1 = 0.786 \frac{L^2}{\mu V}$$

19

FIGURE 1.7.1. *Simulated theoretical current profiles obtained for different trapping times τ (expressed in $L^2/(\mu V)$ transit time units). After [9].*

. The fact that the time position t_{max} of current maximum depends only on mobility μ, sample thickness L, and applied voltage V renders the use of space-charge-limited current transient responses very attractive. As thickness and voltage are easily known, the mobility value is more straightforward to be extracted that from current-voltage characteristics.

Further advantage is that the position of maximum is relatively independent of other factors not taken into account in the simple theory presented here. Figure 1.7.1 presents simulated curves obtained for different trapping times. It can be seen that peak time position is almost independent of trapping. If trapping time is smaller than transit time, the peak disappears. However, mobility estimation, if successful, is mostly independent of the trapping effects. This is in contrast with mobility extraction from current-voltage characteristics, which can be affected by trapping in a complex way. The fig. 1.7.1 is somewhat classical demonstration of reliability of material characterization using space-charge-limited current transients from[9]. In order to reproduce classical diffusion-neglecting result, very low diffusion coefficient was used in the simulation.

The effects of contact barrier on space-charge-limited current transient response is also of great interest. Simulated evolution of transient response in function of barrier height is presented in fig. 1.7.2, presenting results similar to those published in ref. [26]. It may be seen that the peak disappears for barrier heights preventing formation of ohmic contact. However, in the quasi-ohmic range, the position of the peak is almost unaffected by injection barrier. This is in sharp contrast with stationary current magnitude.

Disappearance of the maximum when contact barrier is significant is very useful for using transient space-charge-limited current for verification of contact ohmicity[11, 31, 32, 33].

The classical theory of transient space-charge-limited currents neglects diffusion. Diffusion affects observed transients in two ways. Firstly, diffusion of charge carriers from contacts changes actual value of current at the time of application of voltage step($t = 0$)[34]. Initial decay of current can be seen in all figures presented here referring to the case of ohmic contacts. In the case of existence of contact barrier, current magnitude may be growing at time close to $t = 0$, as predicted by the analytical theory neglecting diffusion. The other effect is smoothing of the current peak, in such a way that current at peak time approaches stationary current. In practice, this effect is reduced by trapping and is observed only in trapless insulators. Representative example of this type of curve is published in ref. [35].

Figure 1.7.3 gives another example of evolution of transient responses in presence of barrier, for different voltages. Again, if current maxima are observed, they appear at the same time.

Further information about material are obtained by looking at transient responses at times longer than transit time. From current decay, information about trapping kinematics can be obtained[36, 37]. Another interesting possibility is to performing transient measurements on a preexcited sample[37].

Therefore, using transients permits, in principle, separate observation of electrode, bulk transport and trapping.

1.8. Conclusions

In this chapter, important aspects of space-charge-limited transport in insulators were briefly reviewed. The importance of space-charge-limited current transport is twofold. Firstly, many organic electronic devices would utilize space-charge-limited current transport in organic electronic materials. Secondly, measurements of space-charge-limited currents are very sensitive to material properties and interface properties. This is especially true with respect to defects, which act as trapping centres. In fact, before rise of importance of organic electronics, space-charge-limited current measurements were considered to be sensitive defect spectroscopy applicable to insulating solids[10].

The review presented here was as short as possible. Purposefully, all discussion taking into account transport states distribution was postponed to next chapters. They give rise to field and charge carrier concentration dependent mobilities, which further complicate analysis of experimental results. Despite these, the most important concerns for application in organic material characterization were demonstrated.

In the first approximation, magnitude of stationary current density is proportional to charge carrier mobility. Unfortunately, trapping and contact barrier affect notably observed current densities. Distinguishing between these effects is difficult. It would require multiple measurements at different temperatures and utilizing different sample thicknesses. Situation
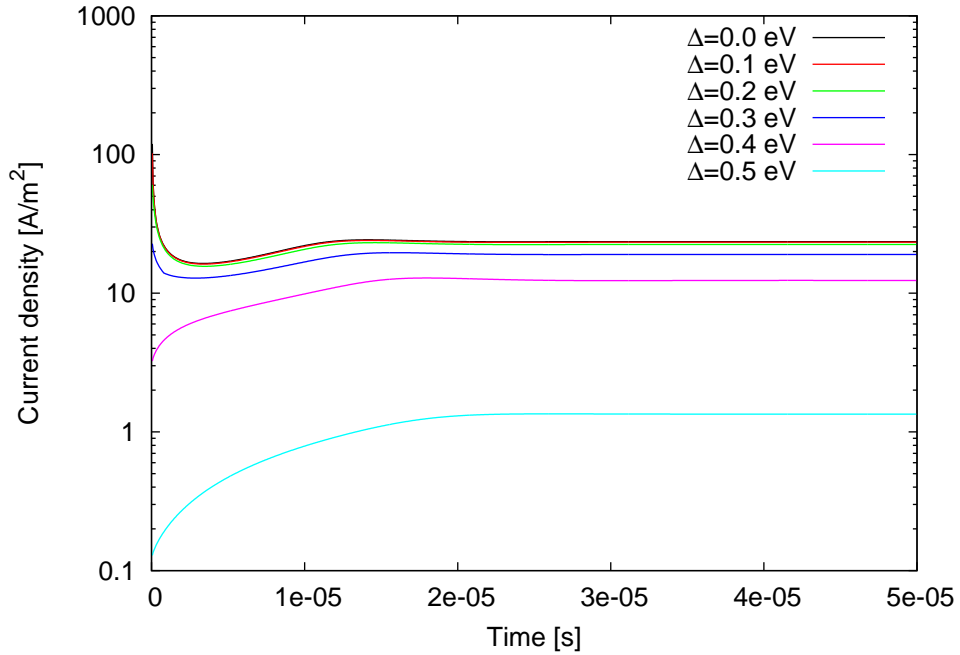
FIGURE 1.7.2. *Evolution of transient response in function of contact barrier height. Fixed simulation parameters: mobility $\mu = 10^{-5} cm^2/(Vs)$, sample thickness $L = 200nm$, applied voltage $2V$, room temperature. Charge injection from metal is modeled according to model described in section 2.4.*

is further worsened by importance of diffusion effects which invalidate simple analytical models for layer thickness typical for organic electronic devices and preparation procedures. It seems indispensable to use numerical simulation to correctly extract information from current voltage characteristics[15]. Because of all of this, it is difficult to use stationary current measurements only to study electrical transport in organic materials. Usually, complete studies tend to use time-of-flight for mobility measurement and transient space-charge-limited current measurement for contact ohmicity check (i. e. [38, 6]).

There are practical difficulties associated with performing stationary measurements. Current may be decaying very slowly, making performing steady-state measurement impractical. This may be explained by trapping kinematics. The lower the voltage and the deeper the trap levels, the more time it takes the current to reach the stationary value. In has been perfectly illustrated in the classical textbook[10], in the section 7.3 on thermal equilibration times (see fig. 1.8.1) . Stabilization of current requires balance between trapping and detrapping processes, but detrapping time grows exponentially with trap depth. In their example, it is not feasible to reach stationary state if traps at depth below 0.9eV are significant.
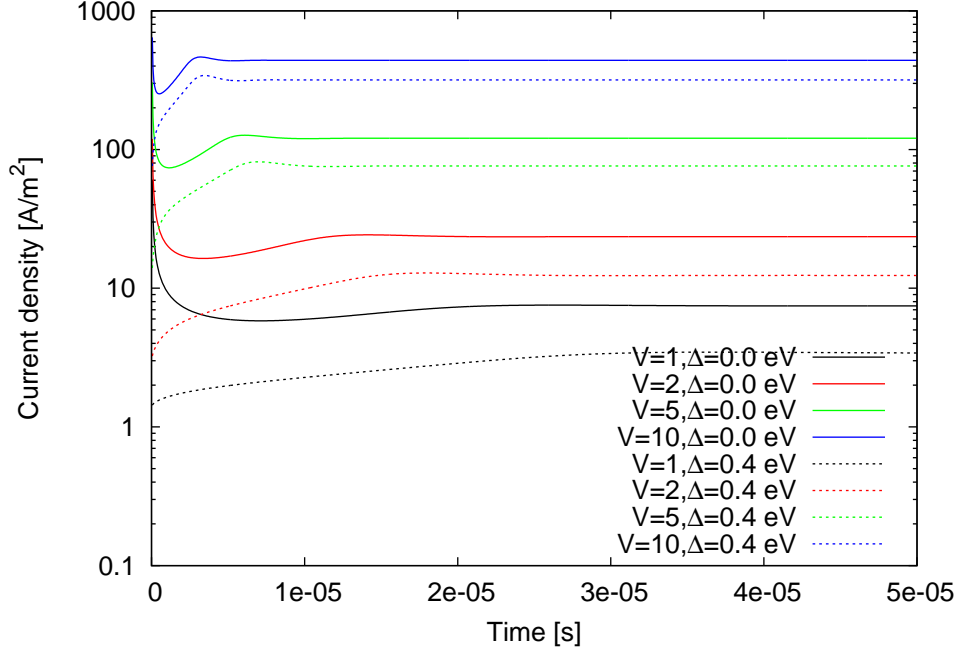
FIGURE 1.7.3. *Evolution of transient response in function of voltage for two contact barrier heights. Fixed simulation parameters: mobility $\mu = 10^{-5} cm^2/(Vs)$, sample thickness $L = 200nm$, room temperature. Charge injection from metal is modeled according to model described in section 2.4.*

Example of another difficulty is shown on fig. 1.8.2. The figure shows fits of an experimental dataset to several simulation models. The dataset exhibits similar agreement to three rather different models associated with different interpretations of the measurement. Although fitting of experimental curves with simulation is now possible, the choice of good model requires a priori good knowledge of material and contact properties.

Transient current measurements is mostly free from these difficulties. Transient measurements naturally provide much more information about material. The application of technique is limited by the quality of contact and trapping[10, 40]. However, when applicable, very good estimation of mobility value is obtained[38]. This removes the need of using time-of-flight to characterize new materials. Furthermore, characterization may take place in configuration close to that of material application. This makes space-charge-limited transient measurement a technique of choice for characterization and optimization of organic materials.

23

TABLE 7.1

THERMAL RELEASE TIMES FROM TRAPS AT ROOM TEMPERATURE

$$\tau_e = 10^{-11} \exp[(E_c - E_t)/kT], \, kT = (1/40) \, eV$$

$E_c - E_t$	τ_e
1.6 (1.61)	1 ae[a]
1.1 (1.09)	3 yr
1.0 (0.98)	10 days
0.9 (0.92)	1 day
0.8 (0.81)	$\frac{1}{4}$ hr
0.75 (0.75)	2 min
0.7 (0.69)	10 sec
0.6 (0.58)	10^{-1} sec
0.5 (0.52)	10^{-2} sec
0.4 (0.40)	10^{-4} sec

[a] 1 ae $= 3 \times 10^9$ yr $\approx$ the age of the earth.

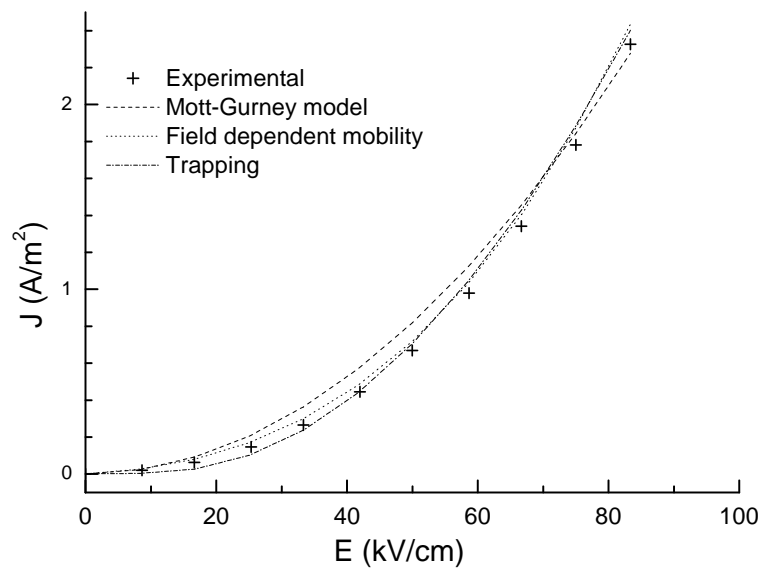FIGURE 1.8.1. *Thermal release time from traps in function of trap depth. Taken from [10], table 7.1.*

FIGURE 1.8.2. *Stationary space-charge-limited current-voltage characteristics and fits with different models, from reference [39].*

CHAPTER 2

Gaussian disorder model and its application to space-charge-limited case

In the previous chapter, macroscopic transport in organic material was considered. It was done without concern for the microscopic mechanisms involved. The material was assumed to be characterized by charge carrier mobility μ. The charge carrier mobility would relate electric field to charge carrier drift velocity. Knowing mobility, and assuming thermal quasi-equilibrium conditions, it was possible to draw many conclusions on stationary and transient electric properties of the material. The effects of microscopic structure of the material can be taken into account by using a functional form of μ.

This chapter is dedicated to a more detailed overview of the influence of microscopic transport mechanisms on macroscopic transport properties. Microscopic transport mechanisms in organic insulators were subject for research for a very long time. It is generally agreed that the transport takes place by hopping between localized states. Multiple theories and models were proposed[41]. Among them, the Gaussian Disorder Model by Baessler and its extensions were proven to be successful for explaining and unifying the experimental observations.

2.1. Gaussian disorder model

The Gaussian disorder model[42, 4] is likely the most successful theory in explaining observations of transport in organic materials. It was widely used to interpret time-of-flight experiments and for explaining temperature and electric field dependences of the charge carrier mobility.

The Gaussian Disorder Model in its basic form assumes that all states are localized on a Cartesian grid. The grid defines sites separated by a distance a; therefore, the total density of states is $N_0 = a^{-3}$. At a given time, each state can be either occupied by charge carrier or not. State energies are random according to a Gaussian distribution to introduce the diagonal(energetic) disorder. The standard deviation σ of such a Gaussian density-of-states is simply called disorder. For convenience, normalized disorder is introduced, defined as

(2.1.1) $$\hat{\sigma} = \sigma/k_B T$$

. Practical values of disorder are in between $50 meV$ and $150 meV$. At room temperature, that corresponds approximately to a $3 \leq \hat{\sigma} \leq 6$ normalized disorder

2.1. GAUSSIAN DISORDER MODEL

Charge carrier transport proceeds by hopping. The Gaussian disorder model assumes a Miller-Abrahams hopping rate. The jump rate from site i to site j is given by the formula

$$(2.1.2) \qquad v_{ij} = v_0 \exp(-2\gamma_{ij}a\frac{\Delta r_{ij}}{a})B(\varepsilon(j) - \varepsilon(i))$$

. In the above, v_0 is the hop attempting frequency, γ_{ij} is the electronic wavefunction overlap factor and Δr_{ij} is the geometric distance between sites i and j. $\varepsilon(i)$ is the total energy of site i

$$(2.1.3) \qquad \varepsilon(i) = E(i) - q\phi(i)$$

where $\phi(i)$ denotes electrostatic potential at site i and q denotes the charge of the carrier. $E(i)$ denotes the random site-specific energy of site i taken from the Gaussian distribution

$$(2.1.4) \qquad p(E) = \frac{1}{\sqrt{2\pi}\sigma} \exp \frac{-(E - E_0)^2}{2\sigma^2}$$

where E_0 denotes the average site energy. In the formula (2.1.2), $B(x)$ is the Boltzmann factor

$$(2.1.5) \qquad B(x) = \begin{cases} \exp\left(-x/k_bT\right) & x \geq 0 \\ 1 & x < 0 \end{cases}$$

. The factor reflects that hops upward in energy require energy from heat bath, while hops downward are unaffected by this condition.

To take off-diagonal(positional) disorder into account, it may be assumed the overlap parameter $2\gamma_{ij}a = \Gamma_{ij}$ to be a statistical quantity. In such a case, the following form was proposed in the original model[42]

$$(2.1.6) \qquad \Gamma_{ij} = \Gamma_i + \Gamma_j$$

. In the sum above,Γ_i and Γ_j are site-specific contributions randomized from Gaussian distribution with variance $\Sigma^2/4$, Σ being off-diagonal disorder parameter. The transport model parameters are therefore either (a, v_0, σ, γ) or (a, v_0, σ, Σ).

This model is built on several implicit physical assumptions[42]. Firstly, the polaronic effects are considered as negligible, yet coupling to heat bath is assumed to be good enough to permit jumps upward in energy. This assumption was only confirmed in some cases, where polaronic effects were shown to have no influence on transport[42, 4]. Secondly, the energetic distribution of states is assumed to take a Gaussian form. This is somehow an

application of the central limit theorem to the case of molecules in disordered solids[4]. At the time of introduction of the model, it was not clear if this assumption is correct or not. Direct measurement of density of states in organic solids is not possible[4]. However, since birth of the theory there has been an increasing number of experimental facts indicating that density of states has indeed the form of a Gaussian curve. These experimental arguments have contributed to the current wide acceptation of the theory outlined here. However, we must stress that Gaussian density of states is best justified for the case of amorphous solids. In the case of polycrystalline solids, exponential density of states instead is often evoked. However, it was demonstrated that both would result in similar electrical properties in typical conditions[43].

Geometric localization of the sites on a cubic Cartesian grid is clearly a simplification of the physical situation. Therefore the model parameter a corresponds to a renormalized intersite distance. This renormalized distance usually does not agree well with typical intermolecular spacings. The parameter takes typical value of order $a \sim 1$nm. In the original Gaussian disorder model, the intersite correlations are neglected. However, introduction of the off-diagonal disorder in the form (2.1.6) implies some correlation. The so called correlated disorder model attempts to remove this limitation[44]. It was shown on some examples that correlated disorder does not agree with experiment[45].

The original Gaussian Disorder Model is for one particle only. Any interactions between charge carriers are thus neglected.

The model involving Gaussian density of states in unsuitable for analytical treatment in the unsimplified form. The most of the original solutions were obtained by Monte-Carlo simulation[42]. Closed form predictions were obtained by fitting analytical formulas to the simulation results. Original Gaussian disorder model gives the following prediction of dependence of charge carrier mobility on temperature T and electric field E:

$$(2.1.7) \qquad \mu(\hat{\sigma}, \Sigma, E) = \mu_0 \exp\left(-\left(\frac{2}{3}\hat{\sigma}\right)^2\right) \begin{cases} \exp C \left(\hat{\sigma}^2 - \Sigma^2\right) E^{1/2} & \Sigma \geq 1.5 \\ \exp C \left(\hat{\sigma}^2 - 2.25\right) E^{1/2} & \Sigma < 1.5 \end{cases}$$

where C is a constant. Since hopping transport is thermally activated, increase of mobility with temperature is predicted. In the zero electric field limit, $\mu \propto \exp\left(-\left(\frac{2}{3}\frac{\sigma}{k_b T}\right)^2\right)$. One of the most interesting properties of the Gaussian disorder model is related to the dependence of mobility on the magnitude of electric field. For values of Σ smaller than 1.5 or $\hat{\sigma}$, an increase of mobility with electric field is expected. That corresponds to the well known Frenkel-Poole effect and is related to barrier lowering by electric field. In the Gaussian density of states, jumps in the field direction are more likely to be downward when strong electric fields are applied. Interestingly, for large off diagonal-disorder Σ, the mobility is expected to decrease
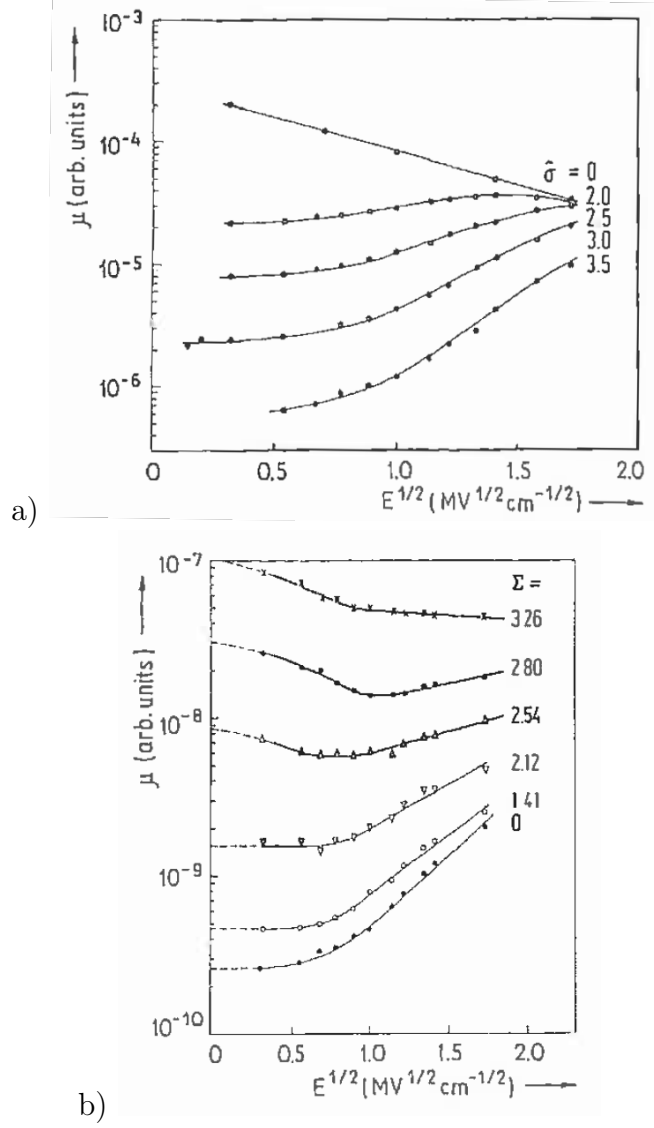
FIGURE 2.1.1. *Simulated mobility dependence on electric field in Gaussian disorder model. a) effects of disorder σ, for $\Sigma = 0$; b) effects of off-diagonal disorder Σ, for fixed σ. From [42].*

with electric field. The effect is explained as reminiscent of percolation. Strong electric field favors jumps which are in the field direction. That reduces the possibility for charge carriers to take an easier path which would be required by a jump perpendicular to the field. Overall field dependency predicted by Gaussian disorder model is presented on fig. 2.1.1.

As already stated above, the Gaussian disorder model was used very successfully for interpretation of time-of-flight experiments. When considering temperature and field dependences, one estimation of disorder was possible for many materials.

2.2. Effect of tail states filling: Master equation approach

Applications of previously introduced Gaussian disorder model to analyzing current-voltage characteristics of devices have had only a limited success. This is in sharp contrast with applications to the analysis of time-of-flight experiments. This is due to the fact that in a well performed time-of-flight experiment, the charge concentration inside the device is negligible. Therefore, the single charge carrier approximation is very well satisfied. This is not true in the case of devices operating under space-charge-limited conditions. It means that charge carrier concentration would be significant. Charge carrier concentration in the space-charge-limited conditions is much higher than in the time-of-flight ones.

Charge carrier concentration is expected to affect mobility in the case of Gaussian density of states. One single state can be only occupied by one single charge carrier. If the charge carrier concentration is significant, it can be expected that low lying states will be occupied by a small fraction of charge carriers. Consequently, the transport of the majority of charge carriers will not be affected by the presence of states with low energy, which will be occupied. Indeed, because time necessary for one upward hop from a state of low energy is exponentially related to its energetic depth, it is the tail of states distribution function that is impeding the drift velocity. But, in the high charge carrier concentration situation, the tail is expected to be filled and does not impede transport of most of the charge carriers. Therefore, the mobility is expected to increase with increasing charge carrier concentration.

Thus, taking into account the effects of charge carrier concentration on mobility allowed the unification of results obtained for the same materials in different devices characterized by different charge carrier density[43].

Master equation approach is used to study the impact of charge carrier density on mobility. Master equation for transport in Gaussian disorder model takes the following form:

$$(2.2.1) \qquad \frac{dp_i}{dt} = \sum_{j \neq i} -p_i(1-p_j)v_{ij} + (1-p_i)p_j v_{ji}$$

where p_i is occupation probability of site i, and hopping rate v_{ij} from site i to site j is defined by (2.1.2). Summing is assumed to be taken over all relevant neighboring sites. The above equation describes time dependent evolution of probability of site occupancy. In order to find the final state, time derivative is to be set to zero. Thus, for constant electric field, the above differential equations system is reduced to algebraic equations system which can be solved easily. This is in sharp contrast with Monte-Carlo simulations which are much more difficult for multiple particles.

In[22], the model above was solved assuming overlap parameter $2\gamma a$ was assumed to be 20. This assumption was considered reasonable for relevant polymer materials. Computational

grid which was used was up to 150^3 and periodic boundary conditions were assumed. Mobility is calculated from solutions of the system above as

$$(2.2.2) \qquad \mu = \frac{\sum_{i \neq j} p_i(1 - p_j)\Delta r_{ij}}{\left(\sum_i p_i\right) F}$$

where F is applied electric field. Neighbors were taken into account to a maximum distance $\sqrt{3}a$. Averages over different disorder configurations were taken until accuracy better than 10% was obtained.

It was found, that in Gaussian density of states mobility can be approximately factorized between the field dependent factor $g_2(T, E)$ and the concentration dependent factor $g_1(T, c)$.

$$(2.2.3) \qquad \mu(T, F, c) \approx \mu_0 g_1(T, c) g_2(T, F)$$

The prefactors are given in the following form[23]:

$$(2.2.4) \qquad g_1(T, c) = \begin{cases} \exp\left[\frac{1}{2}\left(\hat{\sigma}^2 - \hat{\sigma}\right)(2c)^{\delta}\right] & c \leq 0.1 \\ g_1(T, 0.1) & c > 0.1 \end{cases}$$

$$(2.2.5) \qquad \delta = 2\frac{\ln\left(\hat{\sigma}^2 - \hat{\sigma}\right) - \ln\left(\ln 4\right)}{\hat{\sigma}^2}$$

$$(2.2.6) \qquad g_2(T, F) = \begin{cases} \exp\left\{0.44\left(\hat{\sigma}^{3/2} - 2.2\right)\right\}\left[\sqrt{1 + 0.8\left(\frac{qaF}{\sigma}\right)^2} - 1\right] & F \leq 2\sigma/ea \\ g_2(T, 2\sigma/qa) & F > 2\sigma/ea \end{cases}$$

In the equations above, $c = n/N_0$ is the normalized density and q the elementary charge. Note that above function have a cut-off value of argument above which they lose validity. Figure 2.2.1 shows plots of these mobility enhancement functions for several disorder values. It can be seen clearly that the influence of electric field and charge carrier concentration of mobility increases with increasing disorder. In the absence of disorder, mobility would be constant. The functions g_1 and g_2 as given above are components of the so called Extended Gaussian Disorder Model, which will be discussed later.

There is some difference in nature between the enhancement factors. Regardless of disorder, electric field enhancement factor g_2 is close to unity for low electric field. This is in contrast to the charge carrier density enhancement factor g_1 which, for big disorder values $\hat{\sigma} \gtrsim 5$, exceeds unity even for low carrier concentrations $c \approx 10^{-10}$. This implies that for disordered materials, charge carrier concentration dependent effects can be expected to be important in all situations, even for low charge carrier concentrations.
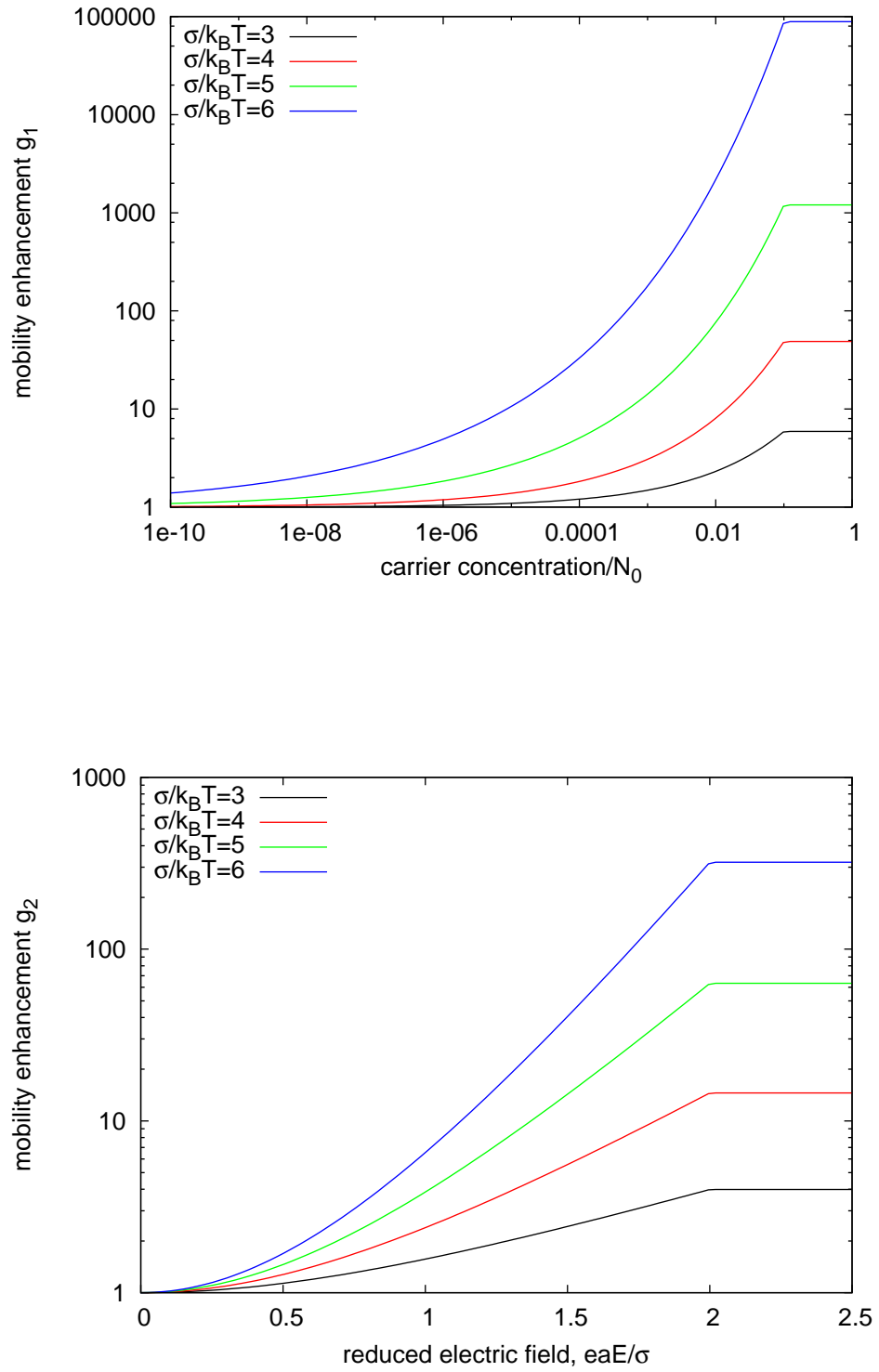
FIGURE 2.2.1. *Mobility enhancement factors on charge carrier mobility in extended Gaussian disorder model. After [23].*

2.3. Generalized Einstein relation

Einstein relation relates the charge carrier mobility μ to the diffusion coefficient D. It is derived by requiring zero electric current $j = 0$ in thermal equilibrium. At the equilibrium, the equation (1.1.7) takes the form

$$(2.3.1) \qquad D\frac{dn}{dx} - \mu n \frac{d\phi}{dx} = 0$$

In this situation, one may expect that Boltzmann statistics would be satisfied. Then, the occupation of states n, at potential ϕ, would be written as

$$(2.3.2) \qquad n(x) = A \exp\left(-q\phi/k_B T\right)$$

giving

$$(2.3.3) \qquad Dn(x)\frac{-q}{k_B T}\frac{d\phi}{dx} - \mu n \frac{d\phi}{dx} = 0$$

$$(2.3.4) \qquad D = \mu \frac{k_B T}{q}$$

The formula (2.3.4) is known as the Einstein-Smoluchowski relation. It was used quite extensively with regard to organic materials. However, it was pointed out[46] that in the case of a Gaussian density of states, a generalized version must be used in which the electric field is replaced by the Fermi level $\eta : \frac{d\phi}{dx} \rightarrow \frac{d\eta}{dx}\frac{1}{q}$. Then the equation takes the form:

$$(2.3.5) \qquad D\frac{dn}{dx} - \mu n \frac{1}{q}\frac{d\eta}{dx} = 0$$

$$(2.3.6) \qquad \left(D\frac{dn}{d\eta} - \mu n \frac{1}{q}\right)\frac{d\eta}{dx} = 0$$

The above formula is obtained by chain rule ($\frac{dn}{dx} = \frac{dn}{d\eta}\frac{d\eta}{dx}$). Since the equation must hold everywhere, this gives

$$(2.3.7) \qquad \frac{D}{\mu} = \frac{n}{q\frac{dn}{d\eta}}$$

The formula (2.3.7) is called the generalized Einstein relation. In the case of Gaussian density of states(eq. (2.1.4)), relation between charge carrier concentration and Fermi level is given as follows:

(2.3.8)
$$n(\eta) = \int_{-\infty}^{+\infty} p(E) f(E, \eta) dE$$

where $f(E, \eta)$ denotes the Fermi-Dirac distribution and $p(E)$ denotes the Gaussian function (eq. (2.1.4)). Combining these equations gives the generalized Einstein relation in the case of a Gaussian density of states:

(2.3.9)
$$\frac{D(\xi)}{\mu} = \frac{k_B T}{q} \frac{\int_{-\infty}^{+\infty} \exp\left[-\frac{E^2}{2\hat{\sigma}^2}\right] \frac{1}{1+\exp(E-\xi)} dE}{\int_{-\infty}^{+\infty} \exp\left[-\frac{E^2}{2\hat{\sigma}^2}\right] \frac{\exp(E-\xi)}{1+\exp(E-\xi)} dE}$$

. This equation has to evaluated numerically.

It is interesting to consider the importance of this correction. It is shown on fig. (2.3.1). Evidently, if disorder is insignificant($\hat{\sigma} = 1$), classical Einstein relation is valid up to very high charge carrier concentration ($c \approx 10^{-2}$). However, in the case of significant disorder($\hat{\sigma} = 7$), using invalid form of Einstein relation introduces a significant error for charge concentrations even as low as $c \approx 10^{-10}$. Because of its importance, the generalized Einstein relation is a part of Extended Gaussian Disorder Model, specified as follows $g_3(T, c)$ (fig. (2.3.2)):

(2.3.10)
$$g_3(T, c) = \frac{q}{k_B T} \frac{D(T, E, c)}{\mu(T, E, c)}$$

It was recently pointed that the generalized Einstein relation can be considered as being invalid in some cases[47], in favor of the classical relation. This is possible if for example low energy tail of the density of states is discharged by recombination.

2.4. Metal-organic interface(2)

Knowledge of the density of states function within insulator gives the possibility of a better description of charge carrier injection from the electrode. Charge injection process can takes place in two steps. Firstly, a pair charge/image charge is generated; then initial jump from the Fermi level in the metal to the organic material takes place . Then, the charge injected is transported by hopping into a potential given by eq. (1.4.1). The potential has a maximum resulting from the superposition of external and image potentials. The maximum (for electric fields from $10^5 \sim 10^6 V/cm$, and dielectric constant ~ 3) amounts to $60 \sim 280$meV and lies $0.7 \sim 3.2$nm from the interface. This exceeds the site dimension and it may take several jumps for charge carrier to exit the electrode region. In conclusion, for high electric fields and high barrier values the first step is the most significant one and dominates the current magnitude. In other cases, both steps are of importance.
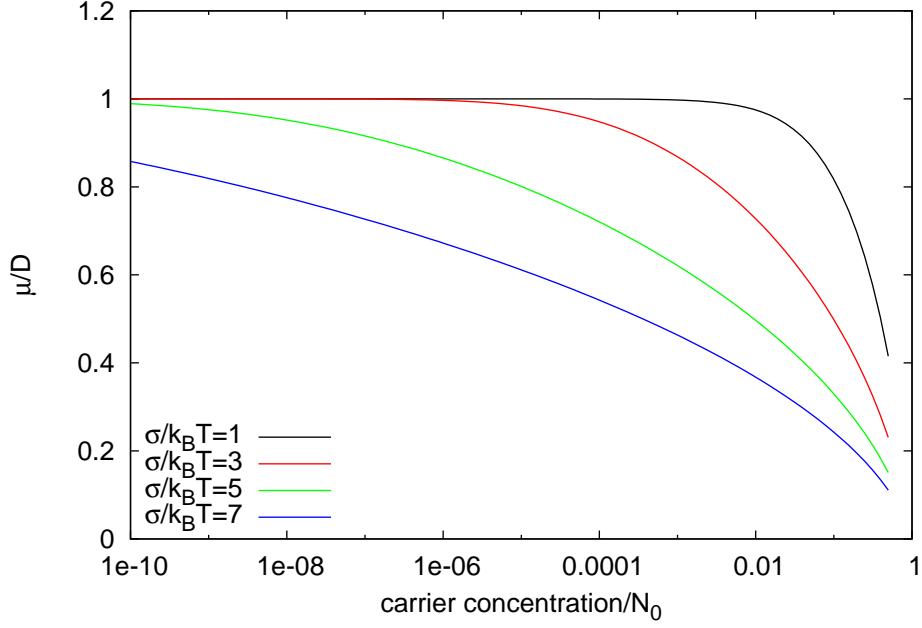
FIGURE 2.3.1. *Inverse Einstein relation in Gaussian density of states. After [46]..*

Early work on charge injection in Gaussian density of states[48], injection limited case was considered and formulas for the current were given. Later, it was suggested that charge carrier concentration near the electrode can be obtained from the condition of local thermal equilibrium. The charge carrier concentration at the interface can be written as

$$(2.4.1) \qquad n_{lte} = N_0 \int_{-\infty}^{+\infty} \frac{p(E)}{1 + exp\left[(E + \Delta')/kT\right]}$$

where Δ' is the electrode barrier Δ corrected with the image-charge term in the form

$$(2.4.2) \qquad \Delta' = \Delta - q\sqrt{\frac{qF}{4\pi\epsilon_0\epsilon_R}}$$

. Above, F denotes electric field at interface and $p(E)$ denotes the density of states function. This model relating the density of states at electrode to the density of states, the barrier height and the electric field fits very well the drift-diffusion model. Consequently, it is now very popular, although it neglects discrete nature of charge carriers[49].

Further investigation was done in [19]. Using master equation approach on three dimensional grid, current flowing through one layer was calculated and compared with predictions
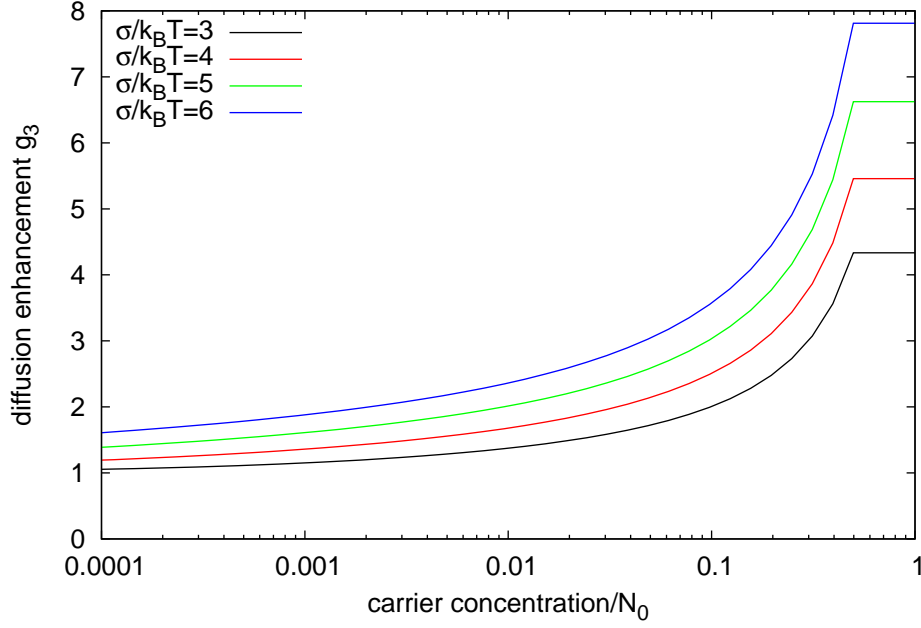
FIGURE 2.3.2. *Diffusion enhancement factor in extended Gaussian disorder model. After [46].*

on drift-diffusion model using above boundary conditions. In the master equation approach, the total site energy was assumed to be a sum of random site-specific energy taken from Gaussian density of states and electrostatic energy. The electrostatic energy contribution was due both to applied field $q\phi_i$ and to image-charge effect $q\phi_{im}$.

$$(2.4.3) \qquad\qquad q\phi = q\left(\phi_i + \phi_{im}\right)$$

Electrostatic potentials in electrode planes were given by boundary conditions for voltage.

$$(2.4.4) \qquad\qquad q\phi(i_x = 1) = qV$$

$$(2.4.5) \qquad\qquad q\phi(i_x = m_x) = 0$$

ϕ_i was calculated using Poisson equation. Image-charge contribution ϕ_{im} was calculated using the formula

35

FIGURE 2.4.1. *Dependence of the current density on injection barrier, from [19] (fig. 2). Device thickness was $L = 22nm$, voltage $2V$, room temperature and lattice constant $a = 1.6nm$.*
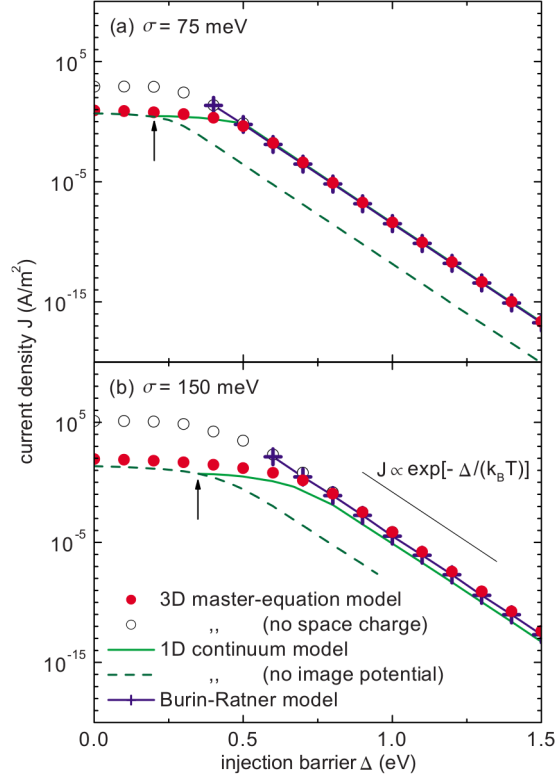
$$(2.4.6) \qquad q\phi_{im}(i_x) = \frac{-q^2}{16\pi\epsilon_0\epsilon_R a} \left(\frac{1}{m_x - i_x} + \frac{1}{i_x - 1} \right)$$

where i_x denotes the layer index($1 \le i_x \le m_x$). The equation above takes into account only the first order expansion term[19]. Importantly, despite the grid is three-dimensional , the electrostatic potential ϕ is assumed to be one function of only one coordinate. The Poisson equation was solved using layer averaged charge carrier concentration. Since electrodes Fermi levels were chosen to be 0, the mean of the Gaussian density of states was equal to the electrode barrier Δ. The same hopping rate to/from electrodes and between sites as well was assumed.

The very interesting conclusion was that the results obtained from one dimensional drift-diffusion model are in very good agreement with detailed master equation, provided that image potential barrier lowering term (2.4.2) is included. The comparison is presented on fig. 2.4.1.

2.5. Conclusions

The Gaussian disorder model applies well to a wide class of organic materials. In order to obtain useful predictions on electrical transport in organic layers, it is then necessary to take into account all the consequences implied when using the Gaussian density of states. These include nonlinear dependences of drift mobility and diffusion on charge carrier concentration, electric field and temperature.

Another important consequence of Gaussian density of states is described in ref. [19]. Charge carriers would prefer easiest paths of transport. In the simulation, percolative effects are apparent in layer of thickness around 22nm. It is demonstrated that charge injection takes place through hotspots. Current density becomes more uniform with distance from the electrodes. While the percolative effects can be expected to be less important for thicker samples, clearly they are an important factor.

The important results on transport in presence of a Gaussian density of states were obtained using Monte-Carlo and master equation simulations. These are still prohibitively expensive from computational point of view to be applied for a wide variety of applications. Fortunately enough, it has been demonstrated [19, 23] that the drift-diffusion model can be extended for the case of Gaussian density of states. By using functional forms of diffusion and mobility, together with appropriate contact model, it is possible to obtained predictions in agreement with master-equation simulations. By using so-called Extended Gaussian Disorder Model, good agreement with experimental current-voltage curves can be obtained[45].

CHAPTER 3

Drift-diffusion simulation

In the chapter 1, the drift-diffusion transport model was introduced. Unfortunately, the model even in its most basic form cannot be solved analytically. In order to obtain analytical solution, diffusion has to be neglected. However, in the case of thin organic films diffusion plays a rather important role. Although analytical results on space-charge-limited current are very useful, it must be stressed that neglecting diffusion may lead to significant errors.

Further effects are even more important, but also difficult to be treated analytically. These are charge carrier trapping and electrode barrier effects. In addition to them, if disorder is important, drift mobility and diffusion coefficient cannot be regarded as constant. Their influence on transport is analytically intractable. Therefore, numerical solutions must be sought for giving a reasonable description of transport in organic solids.

In this aim, numerous approaches have been used . Probably, the first successful attempt was a Monte-Carlo simulation of time-of-flight experiments[42]. The Monte-Carlo method is a powerful and versatile approach for many simulations. Unfortunately, it comes with large computational cost. The simulation is stochastic and the solution contains noise. In order to reduce the amount of noise, many samples must be taken. In the case of transport simulation, all particles have to be treated separately. Thus, the cost of simulation can be expected to grow linearly with the number of particles. In the case of simulations of time-of-flight experiments, the importance of these was limited. It was because the simulation was for one isolated charge carrier particle. The simulation was run for only one particle and with known electric field. These assumptions are in agreement with the physical situation prevailing only in a well performed time-of-flight experiment.

Because Monte-Carlo is expensive for transport problems involving multiple charge carriers, other approaches were preferred. Master equation approach[22] provided useful results when the charge carrier concentration is non-negligible. The master equation approach can be seen as an approximation of the Monte-Carlo simulation, since it involves average quantities and it is continuous in terms of state population. However, the method is considered to be similarly correct as the original Monte-Carlo simulation, but the noise and dependence of cost on number of particles are removed. Using the master equation approach, it was possible to calculate mobility up to very high carrier concentrations($n \sim 0.1N_0$). From a technical point of view, the simulation is done by solving the matrix equation arising from eq. (2.2.1). In the case of device simulation, it is coupled with the Poisson equation. This approach

was taken in[19], where the potential and the site occupancy were alternately updated until obtaining convergence.

Master equation approach is still demanding in terms of computing resources. This is due to the fact that even if one layer is simulated, a three dimensional grid of sites must be used. In order to sample the Gaussian distribution of states well, the grid must have tens of elements in each lateral dimension. For example, a $\sim$50x50x13 grid size was used in[19] to simulate one 22nm thick layer. Each grid site corresponds to one equation, involving tens of neighbors. They all contribute to a nontrivial matrix problem by today standards. Especially in the case of device simulation, where multiple iterations have to be carried out, the approach is still impractical for popular use.

Some authors have sought to reduce the computational cost by making the simulation truly one dimensional[50, 51]. Then, master equation describes transport rates between layers. The approach has had a limited success. It does not correspond to the Gaussian disorder model anymore, as a distribution of states in energy is not taken into account.

The fastest and the best developed method for one dimensional electrical transport simulation is by solving discretized drift-diffusion system. Spatial discretization is introduced, but cell size is not a physical quantity. Since drift-diffusion model was used in electronics since the beginning[5], very efficient numerical methods have been developed. Because of its efficiency, it is best suited for parameter extraction by fitting. At the same time, agreement with more accurate and resource consuming simulation methods was proved[19]. Therefore, in order to simulate charge carrier transport we decided to create state-of-the art implementation of the drift-diffusion simulation.

3.1. Overview

The governing equation for the simulation were introduced in the previous sections. We will recall them for convenience (eqs. 1.1.5, 1.1.6, 1.1.7, (1.5.5)):

$$\frac{d^2\phi}{dx^2} = -\frac{q}{\varepsilon_0\varepsilon_r}\left(n + n_t\right) \tag{3.1.1}$$

$$\frac{\partial}{\partial t}\left(n + n_t\right) = -\frac{1}{q}\frac{\partial j_n}{\partial x} \tag{3.1.2}$$

$$j_n = -q\left(D(F,n)\frac{\partial n}{\partial x} - \mu(F,n)n\frac{\partial \phi}{\partial x}\right) \tag{3.1.3}$$

(3.1.4)
$$\frac{dn_t}{dt} = r_t n \left(N_t - n_t \right) - r_r n_t n$$

(3.1.5)
$$\phi(x = 0) = 0$$

(3.1.6)
$$\phi(x = L) = V$$

(3.1.7)
$$n(x = 0) = n_{lte}(F(x = 0))$$

(3.1.8)
$$n(x = L) = n_{lte}(-F(x = L))$$

Above, $F = -d\phi/dx$ denotes electric field and n_c is given by the contact model (2.4.1). Both diffusion D and μ may depend on electric field and charge carrier concentration in order to take into account the effects of disorder.

The problem to be solved consists in coupling the Poisson (3.1.1) and the charge continuity equations(3.1.2,3.1.3). Figures 3.1.1, 3.1.2 present general block diagrams for electrical transport simulations. In the remaining part of this section, it will be discussed how these steps are realized for the above governing equations. The simulation always starts with an initial state. This state may correspond either to initial guess or initial condition. The simulation normally proceeds iteratively. At each step, solution should be either improved or advanced in time.

The two schemes for solving the type of problem considered here are the decoupled(3.1.1) or the coupled way(3.1.2). In the first case the voltage and the charge carrier concentrations are updated separately, while in the second they are updated simultaneously.

The decoupled approach is flexible and simple to be implemented. The most of simulations on organic electronic materials were performed in such a way. Monte-Carlo simulations as well as many other simulations fill this scheme. However, the decoupled method has very important drawbacks. In the case of simulation of transient responses, some restriction on timestep must be imposed. The time step must be such that solution does not change significantly; otherwise, after one timestep the potential and charge carrier concentration will not agree anymore. If solution variables are strongly coupled, this time will be unacceptably small. In the case of stationary simulation, there is no guarantee that iteration will converge to a self consistent solution. If the coupling is strong, solution may not be converging.

Furthermore, even if the solution is converging, improvement of the solution at each iteration can be small. This would need a large number of iterations and a long computation time.

For its part, the coupled approach requires that the simulation can be discretized as a system of nonlinear equations. This is true in the case of drift-diffusion model. Then, such a system of non-linear equations can be solved to obtain simultaneous update of both charge carrier concentration and voltage. Although each iteration is much more complicated, computation is usually more efficient. The solution variables are self-consistent after each update.

Because simulations of transport discussed here will lead to a stationary situation, it is desirable to use implicit timestepping. Implicit timestepping does not enforce maximum timestep. As simulation is approaching the stationary solution, timestep can be arbitrarily extended. This is in sharp contrast with explicit timestepping, where Courant–Friedrichs–Lewy condition is imposed on the maximum timestep. The implicit time stepping is contained in the coupled scheme.

The first version of the simulator we developed used the decoupled scheme. We found it practically unsuitable to solve even the simplest problems. Although the simulation was correct, the number of iterations necessary to obtain stationary solution was unbearably big. This situation worsened with increase of charge carrier density at boundaries and lack of convergence was frequent. Transient responses could be calculated, but with very large number of time steps. This was undesirable both from point of view of accuracy (cumulative error) and from the point of view of the computation time. Furthermore, because of the aforementioned Courant–Friedrichs–Lewy limit for timestep, it was not feasible to calculate the long decay due to trapping and following the Many-Rakavy peak.

In the current version, coupled scheme has been used. It turned out it worked very reliably in a small fraction of time otherwise needed for the decoupled approach. According to our experience, it is hard to understand why the decoupled solution continues to be given as a viable solution in some references[14]. Thus, the simulator we developed was implemented according to fig. 3.1.2. In the remaining part of this section, it will be explained how the various blocks are realized.

3.2. Scharfetter-Gummel discretization

The discretization grid we used is shown in figure 3.2.1 . The cells are assumed to have the same length Δx. Discrete charge carrier concentration $n_i, n_{t,i}$ and discrete potential ϕ_i are defined in the centres of cells. Discrete current $j_{i+1/2}$ and discrete electric field are defined between the cells.

The Poisson equation 3.1.1 is straightforward to be discretized using finite difference scheme $df/dx \rightarrow (f_{i+1} - f_i)/\Delta x$:
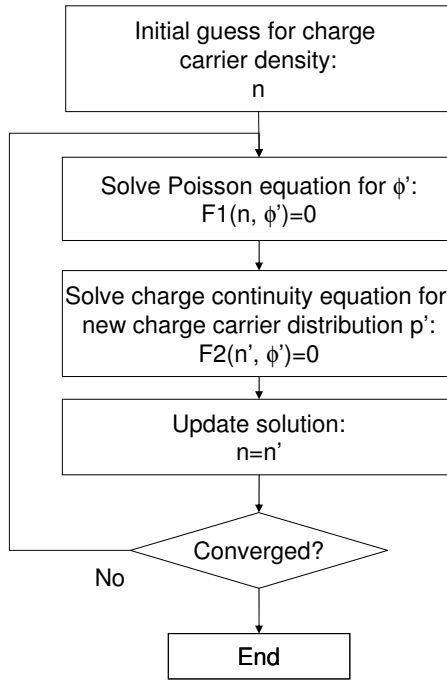
a)
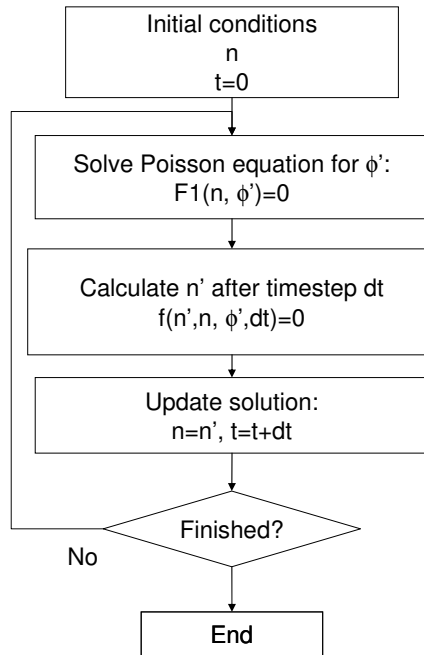
b)

FIGURE 3.1.1. Decoupled simulation scheme: a) applied to a stationary problem (ie. Gummel's iteration scheme); b) applied to a transient problem. F1 and F2 denote discretized Poisson and charge continuity equations (3.3.2), (3.3.3) respectively. $f(n', n, \phi, dt) = 0$ denotes arbitrarily chosen explicit time integration scheme.

a)

b)

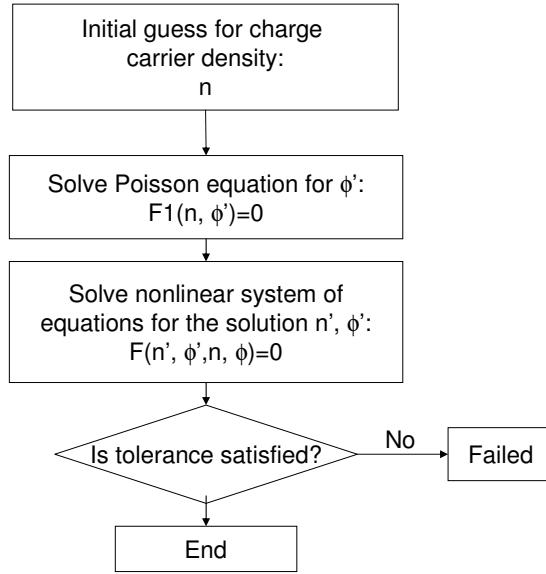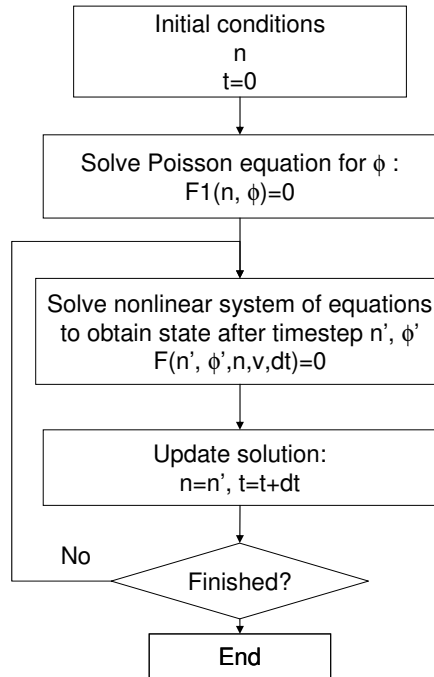FIGURE 3.1.2. Coupled simulation scheme: a) applied to a stationary problem; b) applied to a transient problem. F1 denotes discretized Poisson equation (3.3.2). F denotes the complete discretized drift-diffuson equation system (3.3.5).

43

3.2. SCHARFETTER-GUMMEL DISCRETIZATION

$$(3.2.1) \qquad \frac{\phi_{i-1} - 2\phi_i + \phi_{i+1}}{\Delta x^2} = -\frac{q}{\varepsilon_0 \varepsilon_r}\left(n_i + n_{t,i}\right)$$

It is tempting to proceed in the same way with the charge continuity equation 3.1.2. However, it is much better to do differently by using the so called Scharfetter-Gummel discretization.

When discretizing the charge continuity equation, two problems are important. The charge carrier concentration is a nonnegative quantity and one sharp gradient of concentration can exist in devices. Simple discretization by direct application of finite-difference scheme does not ensure the positivity of the solution. In order to account for sharp charge carrier gradients, dense grid (small Δx) must be used . These requirements are elegantly solved by the Scharfetter-Gummel discretization method[5]. The method effectively uses an exponential interpolation of charge carrier concentration in between nodes. Thus, the solution positivity is ensured and very large gradients can be supported independently of Δx. The Scharfetter-Gummel discretization is known to be optimal for the drift-diffusion problem.

Let's consider the term $\frac{\partial j}{\partial x}$ in the eq. 3.1.2. By applying finite difference

$$(3.2.2) \qquad \frac{\partial j}{\partial x} \rightarrow \frac{j_{i+1/2} - j_{i-1/2}}{\Delta x}$$

In order to derive the Scharfetter-Gummel scheme, we will assume that the current is constant over the interval $x \in [x_i, x_{i+1}]$. The diffusion coefficient D and the charge carrier velocity $v = -\mu \partial \phi / \partial x$ are also assumed to be constant in this interval. The following differential equation

$$(3.2.3) \qquad j(x) = -D\frac{\partial n}{\partial x} + vn(x) = const = j_{i+1/2}$$

holds in each interval $x \in [x_i, x_{i+1}]$. Constant current conditions require spatially changing charge carrier concentration. Boundary values for n are known:

$$(3.2.4) \qquad n(x_i) = n_i$$

$$(3.2.5) \qquad n(x_{i+1}) = n_{i+1}$$

The solution of the equation above is obtained by multiplying both sides by $e^{-v(x-x_i)/D}$

(3.2.6)
$$j_{i+1/2}e^{-v(x-x_i)/D} = \left(-D\frac{\partial n}{\partial x} + vn\right)e^{-v(x-x_i)/D}$$

(3.2.7)
$$= -D\frac{\partial}{\partial x}\left(ne^{-v(x-x_i)/D}\right)$$

and then by integrating both sides of the equation

(3.2.8)
$$\int_{x_i}^{x_{i+1}} j_{i+1/2}e^{-v(x-x_i)/D}dx = -D\int_{x_i}^{x_{i+1}} \frac{\partial}{\partial x}\left(ne^{-v(x-x_i)/D}\right)dx$$

. Using $x_{i+1} - x_i = \Delta x$

(3.2.9)
$$j_{i+1/2}\int_0^{\Delta} e^{-vx'/D}dx' = -D\left(ne^{-v(x-x_i)/D}\right)|_{x_i}^{x_{i+1}}$$

(3.2.10)
$$j_{i+1/2}\frac{D}{v}\left(e^{-v\Delta/D} - 1\right) = D(n_i - n_{i+1}e^{-v\Delta/D})$$

Finally

(3.2.11)
$$j_{i+1/2} = v\frac{n_i - e^{-v\Delta/D}n_{i+1}}{1 - e^{-v\Delta/D}} = v\left(B_1\left(-v\Delta/D\right)n_{i+1} - B_0\left(-v\Delta/D\right)n_i\right)$$

where the auxiliary functions are

(3.2.12)
$$B_0(x) = \frac{1}{e^x - 1}$$

(3.2.13)
$$B_1(x) = \frac{e^x}{e^x - 1}$$

It is interesting to consider the limiting cases:

(3.2.14)
$$\begin{cases} v \to 0 & vB_0 \to D/\Delta, vB_1 \to -D/\Delta, j_{i+1/2} = D\frac{n_i-n_{i+1}}{\Delta} \\ v \to -\infty & B_0 \to 0, B_1 \to 1, j_{i+1/2} = vn_{i+1} \\ v \to \infty & B_0 \to 1, B_1 \to 0, j_{i+1/2} = vn_i \end{cases}$$

.

As expected, if drift velocity is negligible, only the diffusion term is reproduced and conversely, in the very high velocity limit, only the drift term is reproduced.
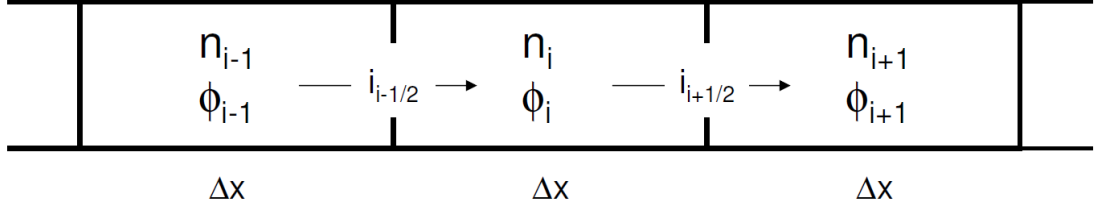
FIGURE 3.2.1. *Discretization grid used. n_i denotes discretized charge carrier concentration in cell i. ϕ_i denotes discretized electrical potential. $j_{i-1/2}$ denotes current flowing from cell $i-1$ to cell i. Δx denotes spatial sampling.*

Formula 3.2.11 is known as the Scharfetter-Gummel formula for current density. The formula gives a form of current which is a linear combination of charge carrier densities. Finally, the following discretization of $\partial j/\partial x$ is obtained

(3.2.15)
$$\frac{\partial j}{\partial x} \to \frac{1}{\Delta x} \left(v_{i+1/2} \left(B_1(-v_{i+1/2})n_{i+1} - B_0(-v_{i+1/2})n_i \right) - v_{i-1/2} \left(B_1(-v_{i-1/2})n_i - B_0(-v_{i-1/2})n_{i-1} \right) \right)$$

where the velocity between nodes is

(3.2.16)
$$v_{i+1/2} = \mu_{i+1/2} \frac{\phi_{i+1} - \phi_i}{\Delta x}$$

3.3. Solving and convergence

To formulate the discretized version of the equation system being solved, it remains to write the time derivative. We choose backward Euler method for this purpose:

(3.3.1)
$$\frac{dn}{dt} = \frac{n - n^{old}}{\Delta t}$$

where n^{old} is charge carrier concentration before the time step, and Δt is time step duration. Using above, and rewriting the equations (3.1.2), (3.1.4), (3.2.1) in the standard form, one obtains

(3.3.2)
$$F_1(\phi, n, n_t) = \frac{\phi_{i-1} - 2\phi_i + \phi_{i+1}}{\Delta x^2} + \frac{q}{\varepsilon_0 \varepsilon_r} (n_i + n_{t,i}) = 0$$

(3.3.3)
$$F_2(\phi, n, n_t) = \frac{n_i - n_i^{old}}{\Delta t} + \frac{n_{t,i} - n_{t,i}^{old}}{\Delta t} + \frac{1}{q} \frac{j_{i+\frac{1}{2}} - j_{i-\frac{1}{2}}}{\Delta x} = 0$$

46

$$(3.3.4) \qquad F_3(n, n_t) = \frac{n_{t,i} - n_{t,i}^{old}}{\Delta t} - r_t n_i \left(N_t - n_{t,i}\right) + r_r n_{t,i} = 0$$

where $j_{i+1/2}$ is given by eq. 3.2.15. Note than all symbols above ϕ, n, n_t refer to vectors of length N, corresponding to the discretized version of the original variables on grid with N nodes. It remains a set of $3 \times N$ algebraic equations

$$(3.3.5) \qquad F(\phi, n, n_t) = \begin{bmatrix} F_1 \\ F_2 \\ F_3 \end{bmatrix}$$

. Because $F : R^{3N} \to R^{3N}$ is easily differentiable, it is optimal to use the Newton-Raphson method to obtain the solution.

The Newton-Raphson method is most easily illustrated in the one variable case. In order to solve $f(x) = 0$, one starts with initial guess of solution x_0. Then, if conditions for applicability of the method are satisfied, solution x_i is improved according to formula:

$$(3.3.6) \qquad f'(x_i)(x_i - x_{i+1}) = -f(x_i)$$

The process is repeated until convergence is obtained. Let's denote by x a vector of solution variables

$$(3.3.7) \qquad x = \begin{bmatrix} \phi \\ n \\ n_t \end{bmatrix}$$

In the multivariate case, the Newton-Raphson formula is

$$(3.3.8) \qquad J_F(x_n)(x_{n+1} - x_n) = -F(x_n)$$

where $J(x)$ denotes the Jacobian matrix of F calculated at x

$$(3.3.9) \qquad J_F(x)_{ij} = \frac{\partial F_i}{\partial x_j}\bigg|_x$$

In the case of simulation described here, $J_F(x)$ is a matrix of size $3N \times 3N$. The matrix contains only a small number of nonzero elements. It remains to define convergence criteria. For this, absolute convergence criterion

(3.3.10)
$$|x_i - x_{i+1}| < \epsilon_{abs}$$

and relative convergence criterion

(3.3.11)
$$\left| \frac{x_i - x_{i+1}}{x_i} \right| < \epsilon_{rel}$$

are used. If either is satisfied, x_{i+1} is considered to be a solution and the iteration is finished.

3.4. Timestepping

From practical point of view, the way the timestep Δt is chosen is very important. In the case of transient simulation, the initial current peak is followed by a long current decay due to trapping. When charge carrier front is traveling through the sample, the solution is changing significantly and a timestep shorter than the transit time must be used. On the other hand, during the long decay, the solution is changing very slowly and eventually a timestep much longer than the transit time may be useful. If timestep can be extended, one may arrive at stationary limit by taking $1/\Delta t \to 0$. Therefore, in order to perform the simulation efficiently, it is practical to be able to adjust Δt automatically for ensuring visible evolution of the solution. The reduction of number of timesteps not only reduces the solution calculation time, but in some cases may in fact reduce the simulation error. This is because with each iteration some amount of numerical error is produced and may accumulate.

In order to define an automatic criteria for adaptive timestepping, a local error metric ϵ is introduced . We have chosen the following form

(3.4.1)
$$\epsilon = \left| \frac{j_t (t_0 + \Delta t + \Delta t) - j_t (t_0 + 2\Delta t)}{j_t (t_0 + \Delta t + \Delta t)} \right|$$

where j_t is the observed current including the displacement current contribution. $j_t (t_0 + 2\Delta t)$ denotes the current value on the basis of a single time step of duration $2\Delta t$ and $j_t (t_0 + \Delta t + \Delta t)$ denotes the current value for the same time calculated with two time steps of duration Δt. Calculating the current value in two ways increases amount of calculation, but permits a reasonably reliable adjustment of the timestep.

Timestep is automatically adjusted to keep local error close to the goal value $\epsilon \sim \epsilon_{goal}$. A proportional–integral–derivative(PID) controller approach is used for that[52]. One typical value for ϵ_{goal} is 5×10^{-3}.

3.5. Adaptation for organic materials

To obtain correct results in the case of organic materials, the effects of disorder on mobility must be taken into account. This is done by using Extended Gaussian Disorder Model (eqs. (2.2.4), (2.2.6)).

$$\mu(T, F, n) = \mu_0 g_1(T, n/N_0) g_2(T, F) \tag{3.5.1}$$

$$g_1(T, c) = \begin{cases} \exp\left[\frac{1}{2}\left(\hat{\sigma}^2 - \hat{\sigma}\right)(2c)^\delta\right] & c \le 0.1 \\ g_1(T, 0.1) & c > 0.1 \end{cases} \tag{3.5.2}$$

$$\delta = 2\frac{\ln\left(\hat{\sigma}^2 - \hat{\sigma}\right) - \ln\left(\ln 4\right)}{\hat{\sigma}^2} \tag{3.5.3}$$

$$g_2(T, F) = \begin{cases} \exp\left\{0.44\left(\hat{\sigma}^{3/2} - 2.2\right)\right\}\left[\sqrt{1 + 0.8\left(\frac{qaF}{\sigma}\right)^2} - 1\right] & F \le 2\sigma/qa \\ g_2(T, 2\sigma/qa) & F > 2\sigma/qa \end{cases} \tag{3.5.4}$$

Lastly, the generalized Einstein relation for Gaussian density of states must be used (eq. 2.3.10):

$$D(T, F, n) = \frac{k_B T}{e}\mu(T, F, n)g_3(T, n) \tag{3.5.5}$$

where (eq. 2.3.9)

$$g_3(T, n) = \frac{n}{\frac{\int_{-\infty}^{+\infty}\exp\left[-\frac{E^2}{2\hat{\sigma}^2}\right]\frac{1}{1+\exp(E-\eta(n))}dE}{\int_{-\infty}^{+\infty}\exp\left[-\frac{E^2}{2\hat{\sigma}^2}\right]\frac{\exp(E-\eta(n))}{1+\exp(E-\eta(n))}dE}} \tag{3.5.6}$$

One specific problem is that mobility and diffusion must be evaluated between nodes $(\mu_{i+1/2}, D_{i+1/2})$ while charge carrier density is defined inside nodes(n_i). One can consider evaluating mobility and diffusion directly at half nodes by interpolating charge carrier concentration ($n_{i+1/2} = (n_{i+1} + n_i)/2$). It was found to lead to significant error and convergence problems. Thus, charge carrier density dependent factors are evaluated for nodes. Note that the Gaussian disorder model intersite distance a and simulation grid spacing Δx are unrelated quantities. The first corresponds to physical material parameter, while the other is a simulation parameter only.

$$(3.5.7) \qquad\qquad g_{1,i} \;=\; g_1(T, n_i/N_0)$$

$$(3.5.8) \qquad\qquad g_{3,i} \;=\; g_3(T, n_i)$$

and interpolated in half-nodes when necessary

$$(3.5.9) \qquad\qquad \mu_{i+1/2} = \mu_0 \left[\frac{1}{2}\left(g_{1,i} + g_{1,i+1}\right)\right] g_2(T, F_{i+1/2})$$

$$(3.5.10) \qquad\qquad D_{i+1/2} = \frac{k_B T}{e}\mu_{i+1/2}\left[\frac{1}{2}\left(g_{3,i} + g_{3,i+1}\right)\right]$$

3.6. Implementation

The simulation was implemented with Python 2.7 using Scipy. Python is a high level interpreter language and a very convenient tool for scientific calculation. Pure Python usually runs significantly(usually $\gg 10\times$) slower than the languages that were considered suitable for scientific computing(FORTRAN,C,C++,Java). The performance problem was however solved by extensions, the Numpy and Scipy in the first place. These extensions delegate computationally intensive tasks to highly efficient libraries written in high performance languages. Consequently, if the most of work can be delegated, then Python program can be almost as fast as the fastest codes. On the other hand, Python programs are much easier to write and debug. Python users are mostly free from software engineering tasks such as compilation. Integration of top scientific computing packages such as LAPACK is done by the Scipy project. FORTRAN like vector assignment are supported by Numpy.

Python equipped with scientific computing packages (Numpy,Scipy and Matplotlib) offers the same possibilities and ease as that of Matlab(registered trademark of Mathworks). On the other hand, Python solution is all free, supplier independent, open source and easily extensible.

In the section we will shortly describe the relevant numerical details of the implementation.

The simulator runs according to fig. 3.1.2. The core of the simulator is solving nonlinear system of equations (3.3.5) using Newton-Raphson iteration (3.3.8). Since the Jacobian J_F is sparse and it is not useful to treat it as dense matrix even in the case of very small problem sizes, sparse linear solver is used. Direct sparse solver is optimal. As the solver SuperLU is used via pysparse. SuperLU was checked to be more reliable than UMFPACK and the default Scipy direct solver.

3.6. IMPLEMENTATION

Solving the system $F = 0$ may take up to a predefined maximum number of iterations. Calculation is considered to be done when relative or absolute convergence criteria are satisfied. If they are not satisfied despite that maximum number of iterations was reached, calculation fails.

In the transient simulation, for a two timesteps of Δt, timestepping is performed three times to evaluate the local error(3.4.1). The main result is calculated by applying timestep Δt twice. The auxiliary result is obtained by applying single timestep of $2\Delta t$. While this may be not optimal, additional computational cost is acceptable having result in a form of reliably defined local error. Update of Δt is calculated by the PID controller.

In the case that either the timestep failed or the local error ϵ is too big, the timestep is rejected and simulation is restarted using much (i.e. $\Delta t \times 0.1$) smaller Δt. This may be repeated several times. If minimum reasonable time step is reached, simulation is considered to have failed.

In the case of stationary simulation, initial guess is currently assumed to be empty device($n = 0$) and linearly changing potential. This is probably not optimal[15], but works fine. If stationary simulation does not converge, transient simulation is used instead. Since in such a case the values of current are ignored, timestep is enlarged geometrically for each iteration until $1/\Delta t \approx 0$. If a I-V curve is calculated, stationary state for previous voltage serves as the initial guess.

In the case of transient simulation initial guess is assumed to be the equilibrium conditions by default. Equilibrium conditions are calculated for zero externally applied voltage. Transient simulation finishes when simulation termination time is achieved.

The user can choose which model to use. It is possible to use constant mobility model $\mu = const, D = const$; Frenkel-Poole effect mobility and the Extended-Gaussian disorder model. Metal insulator contact may be modeled using condition of local thermal equilibrium, with or without image potential, or using Scott model[26].

For the conditions of local thermal equilibrium, the integral(2.4.1) is calculated using Gauss-Hermite quadrature. This particular choice of quadrature is caused by the prefactor of Gaussian density of states $\exp{-\alpha E^2}$. The integral is evaluated for finite number set of barriers. Then, it is interpolated using corrected barrier height. As derivative, interpolation derivative is used.

Similarly, the diffusion enhancement factor(3.5.6) is calculated using Gauss-Hermite quadrature, for a finite set of positions of Fermi level. For each value of the Fermi level η, the charge carrier density $n(\eta)$ is evaluated by numerical integration. Because the relation $n(\eta)$ is monotenous, the inverse relation $\eta(n)$ is obtained trivially. In the main simulation, the precalculated pairs (η, n) are interpolated to obtain the continuous functions. Again, as the derivative, the interpolation derivative is used.

3.7. Conclusions

Using simulation approach presented here, stationary and transient space-charge-limited current characteristics can be calculated numerically. This is done only assuming validity of the drift-diffusion model. The effects of diffusion, electrode barrier, trapping and disorder can be taken into account using well established theories.

The simulator was initially intended as a small tool to help in planning and understanding the transient experiments. The first version was based on the advertised Gummel iteration decoupled scheme 3.1.1. Although the program was certainly correct, it was working quite badly. Enormous number of iterations was necessary for completing the calculation. The second version, based on the coupled scheme turned out to be much more efficient and reliable. This result seriously questions the wide use made in the literature of the decoupled approach unless if needed for the underlying simulation method (ie. Monte-Carlo).

Moreover, the big lesson which can be taken from implementing the simulation is that it can run very quickly. A full stationary current voltage curve can be calculated in a time around one second. One transient response, with adaptive timestepping, can be calculated in a time also not exceeding one second on an ordinary computer. This opens real possibilities of using this kind of simulation for analyzing experimental data, especially in the transient case. This possibility has been of course explored and is shown in detail in section 6.

CHAPTER 4

Transient current measurements using transimpedance amplifier

In the section1.7, transient space-charge-limited current response of thin organic layer was considered. It was shown that, in the space-charge-limited case, the response is nonmonotonic function of time with a distinct peak. From the time position of the peak, charge carrier transit time through the sample can be deduced. By analyzing the transient response curve, information on contact performance and trapping can be obtained[12]. It was concluded that transient responses are in fact easier to interpret correctly than the results from stationary characterization. Therefore, their use is of great interest for characterizing organic electronic materials.

Despite the obvious advantages, transient response characterization is seen much less frequently than stationary current voltage characterization. It may be because performing transient experiment is more difficult.

In this chapter, experimental aspects of registering transient responses of thin organic films are considered. The measurement is symbolically illustrated on fig. 4.0.1. Before the measurement, sample is equilibrating with zero voltage applied to it. Then, at time $t = 0$, voltage step is applied to the sample. Simultaneously, starting at the time $t = 0$, current flowing through the sample is measured.

The most important transient current feature to be recovered is the peak time. The peak occurs at time $t_{max} \approx 0.786L^2/(\mu V)$, where L denotes sample sample thickness, μ the charge carrier mobility and V the applied voltage.

The first difficulty with this type of measurement is related to the timescale of peak time t_{max} in thin organic films. In typical experimental conditions, the peak time is of order $1 - 100\mu s$. Although the mobility in films under consideration is small and not expected to exceed $10^{-3}cm^2V^{-1}s^{-1}$, together with typical layer thickness (~ 200nm) and typical applied voltage ($\sim 2V$) they would produce space-charge-limited current peak in that range. Putting these parameters into the formula, $t_{max} \approx 0.15\mu s$ is obtained for mobility $10^{-3}cm^2/(Vs)$. Even for very low mobility $10^{-6}cm^2/(Vs)$, $t_{max} \approx 150\mu s$ is obtained. For a given charge carrier mobility value in a material, the peak time cannot be adjusted arbitrarily with sample thickness and voltage. The manufacturing processes (ie. spin-coating) put practical limitations on maximum layer thickness and there is a minimal voltage for which the peak is visible. This minimum voltage limit results in the first place from trapping effects.

The current measurement speed must be much faster than t_{max} in order for peak to be registered. This puts practical requirement on time of single current measurement being not more than $\sim 1\mu s$. This measurement speed exceeds capabilities of an usual, commercial current measurement devices such as source-measure units and amperometers.

The next problem comes from limited mobilities in thin organic films. For a given mobility value, the maximum possible current density is well approximated by Mott-Gurney law (eq. 1.2.8). The current peak overshoots stationary current value only slightly. Therefore, the device must be adapted to measure rather low currents. Increase of voltage and sample area may be thought as remedies for this. Indeed, increase of voltage would increases current density $\propto V^2$. However, at the same time power dissipation would increase as $\propto V^3$, potentially leading to sample heating. Sample breakdown voltage also has to be taken into account. Depending on material properties, certain samples should be able to withstand considerable voltages, while others will fail much more quickly.

In order to understand the main difficulty for this type of measurement, it must be taken into account that sample has geometrical capacitance. Sample capacitance effects are unseen in the case of stationary measurement. However, in the case of transient measurement the capacitance introduces RC constant and the displacement current contribution. The geometric capacitance is given by formula

$$(4.0.1) \qquad\qquad\qquad\qquad C_0 = \epsilon_0 \epsilon_r \frac{A}{L}$$

where A denotes sample area. Taking typical relative dielectric permittivity $\epsilon_r = 3$ and sample thickness $L = 200nm$, capacitance for sample of surface $A = 1cm^2$ is $\approx 13 \times 10^{-9}$F. Using a typical signal generator with output impedance 50Ω, it takes approximately $1.5\mu s$ to charge such a capacitor to 0.9 of desired voltage.

The measured space-charge-limited current

$$(4.0.2) \qquad\qquad\qquad\qquad i = Aj$$

is also proportional to the sample area, with j denoting the current density. The ratio of current to capacitance is therefore independent of the sample area. Increasing the sample area, while permits to increase the observable current, has a drawback the capacitance and its effects are proportionally increased. Furthermore, it is easier to produce uniform samples of smaller area.

The generalized form of the measurement circuit is presented on fig. 4.0.2. The following contributions affect the measurements. R_s denotes serial resistance of the voltage source. It includes the source output impedance (ie. 50Ω for typical signal generator) as well as

resistances of all connections. Small evaporated connections may have nonnegligible resistance. C_s denotes distributed parasitic capacitances in the circuit. If coaxial cable is used, 1 metre will contribute approximately 70pF. Amplifier input capacitance (i.e. oscilloscope) may be also contributing negligibly to C_s. R is the shunt resistance. The resistances and capacitances present in the circuit affect the measurement in two ways. Firstly, they limit the current measurement speed with time constant RC_S. Also importantly, they limit the speed of voltage settling on the sample itself, with time constant $(R + R_s)C_0$. The latter must be much shorter than t_{max} in order to make the assumption of voltage step correct.

The requirements for proper space-charge-limited current transient measurement are specified in ref. [40]. There, the collective time constant is introduced

$$(4.0.3) \qquad\qquad \tau = (R + R_s)(C_0 + C_s)$$

as well as a parameter

$$(4.0.4) \qquad\qquad \alpha = 2t_r/\tau$$

to quantify space-charge-limited current distortion. There responses undistorted for $\alpha > 100$, distorted for $20 < \alpha < 100$ and indistinguishable for $\alpha < 20$. Above t_r denotes space-charge-free transit time

$$(4.0.5) \qquad\qquad t_r = \frac{L^2}{\mu V}$$

Even for very small timeconstant $\tau = 10^{-8}$s, obtained by assuming $R_s = 50\Omega$ of generator output impedance, $R = 50\Omega$ of oscilloscope input impedance and $C_0 + C_s = 100\times10^{-12}$F, the smallest ideally reproduced t_r is just 500ns. These optimistic conditions correspond to thin film sample area below $1mm^2$, yet current measurable with a 50Ω shunt resistor. If the current of interest is small, then R must be increased. This will increase the time constant and the limit on minimum t_r.

The presence of sample geometric capacitance C_0 introduces displacement current contribution i_0 , which adds to the current of interest i. Taking it into account, the total observable current i_{total}:

$$(4.0.6) \qquad\qquad i_0 = C_0 \frac{dV}{dt}$$

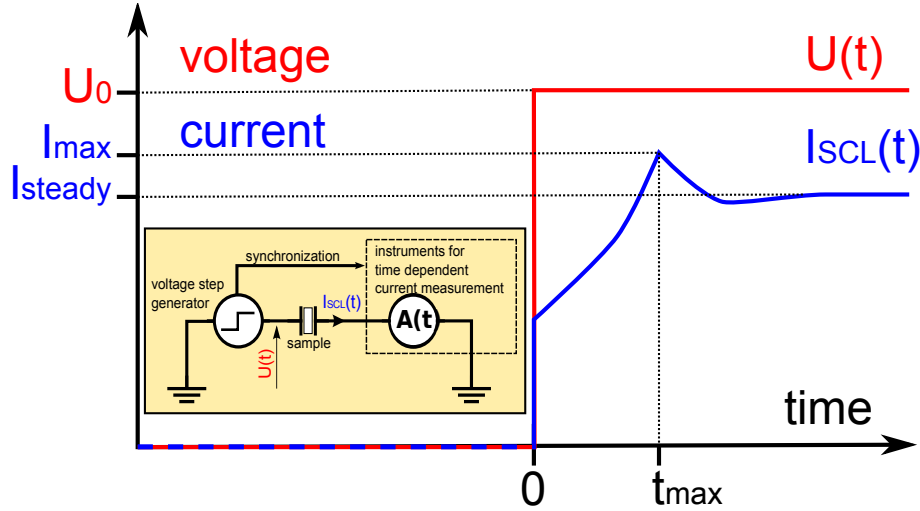$$(4.0.7) \qquad\qquad i_{total} = i + i_0$$

FIGURE 4.0.1. *The concept of space-charge-limited current transient measurement. Inset: simplified scheme of the experimental setup.*
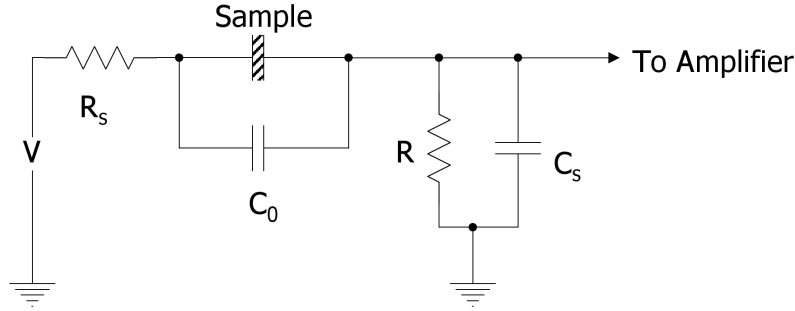

FIGURE 4.0.2. *Generalized circuit for observing transient space-charge-limited currents.*

Around $t = 0$, the capacitive displacement current contribution can be expected to be much larger than transient space-charge-limited current at any time. This introduces dynamic range problem in the measurement. At the beginning of the measurement, signal at amplifier exceeds signal of interest by orders of magnitude.

4.1. Bridge circuit

Certain authors use the setup outlined on fig. 4.0.2 directly. In such a case, sample can be literally connected between the signal generator and the oscilloscope. If chosen to do so, R is simply the oscilloscope input impedance. Then, oscilloscope input must be switched to the low impedance mode (universally 50Ω). If such a low value of shunt resistance is not acceptable, oscilloscope input can be switched to the high impedance mode (universally $1M\Omega$) and shunt resistor can be inserted in parallel to it, ie. between the oscilloscope input and ground.

4.1. BRIDGE CIRCUIT

This approach, although very simple, has important drawbacks. In order to ensure sufficient bandwidth and low voltage burden, R must be small. This, by ohms law $u_{total} = R \cdot i_{total}$, potentially implies small voltage signal. Authors who use this approach may need to average multiple measurements in order to get acceptable signal to noise ratio[2]. The oscilloscope input circuitry must deal with the dynamic range of input signal directly.

More sensitive measurements, such that $t_{max} \sim 10^{-6}$s, are performed using a form of bridge circuit. The function of the bridge circuit is to subtract displacement capacitive current contribution i_0 from the input signal. After this, the input signal is free from the displacement current decay with time constant $(R_S + R)C_0$. This way, even if the sufficient bandwidth condition is not well fulfilled, the current peak may be well visible. Additionally, the dynamic range of signal is reduced to that of space-charge-limited current response.

The bridge circuit is widely used since the first works on transient space-charge-limited current measurements[10]. The circuit, in its modern form is presented on fig. 4.1.1. It still remains in use[53].

One arm of the bridge contains the sample and the shunt resistor R. The other arm contains adjustable resistance and capacitance, along with the same shunt resistance. The adjustable elements are to be matched to the geometric capacitance of the sample and its equivalent serial resistance. When matched, upon application of voltage step, the same capacitive displacement current i_0 flows in both arms of the bridge. Then, voltage due to capacitive displacement current flowing through shunt resistance R is subtracted by the difference amplifier. In theory only the contribution due to the current of interest is obtained at output of the difference amplifier.

Although elegant, the circuit has some practical limitations and difficulties in use. Firstly, the subtraction of displacement current signals relies critically on the circuit symmetry. Attention must be paid to realize both arms of the bridge as symmetrically as possible. This includes apparently minor details like cable lengths[53]. Even with perfect symmetry of the electronic parts, the compensation cannot be done perfectly. Certain degree of mismatch cannot be eliminated because of difference of dielectric properties of the sample and that of the adjustable capacitor. Although the measurement itself is very quick, the adjustment of the resistor and capacitor are sample specific. The use of auxiliary sinusoid signal generator is recommended for this[12].

Another practical advantage of this type of circuit is that parasitic capacitances can be better controlled when separating sample circuit and oscilloscope with the difference amplifier. The current measurement bandwidth of this circuit can be determined by just by shunt resistance R and difference amplifier input capacitance. For given value of R is is therefore easier to obtain better bandwidth than by using oscilloscope directly.
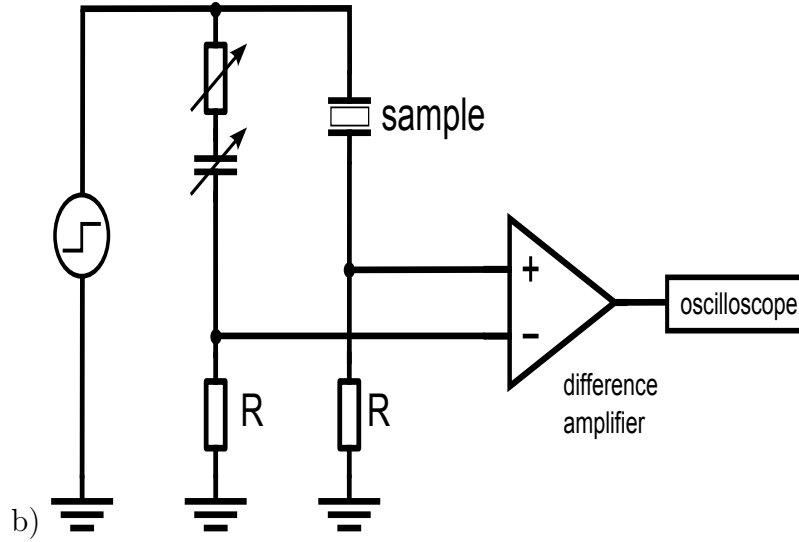
FIGURE 4.1.1. *Current version of the bridge circuit widely used[12, 38, 53] for space-charge-limited current transient measurements.*

On the other hand, it must be understood that sample charging time is still determined by the time constant $C_0(R + R_S)$. Even if the current can be measured much faster, and displacement current contribution can be subtracted, the voltage step settles on the sample with this time constant. This detail may be a reason for reported influence of bridge circuit on transit time uncertainty[2].

4.2. Transimpedance circuit

Previously outlined simple solutions utilizing either shunt resistor alone or bridge circuit have applicability limited by the maximum value of shunt resistance R. Too large value will unacceptably increase rise times both for voltage step and for current measurement. The necessity to keep R small, on the other hand, requires sample that would conduct sufficiently large space-charge-limited current. Otherwise, voltage drop on shunt resistor R may be to small to be observed without being dominated by noise. This in turn puts requirements on the sample area. The bridge indeed makes simpler the observation of the space-charge-limited current peak, but must be used carefully and has its own deficiencies.

In the work presented, a different approach for measurements of transient space-charge-limited currents is used. The circuit is presented on fig. 4.2.1. Instead of measuring current as voltage drop on shunt resistor, transimpedance amplifier is utilized. Transimpedance amplifier consists in an operational amplifier and a feedback resistor R. Input is delivered to the inverting input of the operational amplifier(-), while the noninverting input(+) is grounded. Output signal is given at operational amplifier output terminal.

The proposed circuit differs fundamentally from that on fig. 4.0.2 by the potential level at which sample electrode on the current measurement side is kept. In the case of fig. 4.0.2,
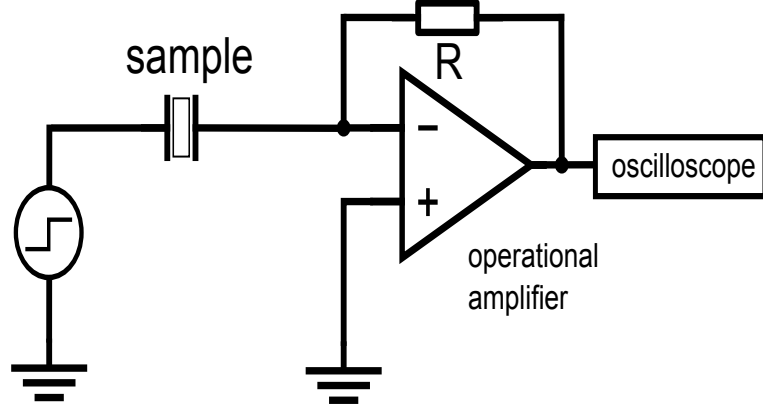
FIGURE 4.2.1. *Proposed circuit for transient space-charge-limited current measurements of mobility using transimpedance amplifier[54].*

this potential is $i_{total} \cdot R$ and it is the same as the measured voltage signal. In the proposed solution, this potential is (attempted to be) kept at zero voltage by the operational amplifier. Output voltage signal equals is -$i_{total} \cdot R$ and is present only at the operational amplifier output.

This has some practical implications. Now R does not contribute to voltage rise time on sample. Therefore, current measurement gain and voltage step setting time are independent. This permits improving measurement accuracy by better defining t_{max}. At the same time, the current measurement rise time becomes not directly dependent on the capacitances present in the circuits (ie. C_s), but only on the feedback impedance R.

These properties are easiest to understand using the ideal operational amplifier model. Ideal operational keeps both inputs at the same voltage, and does not source or sink current through them. From the inverting(-) input must be kept at $0V$, and no current can flow through it, it immediately follows that the output voltage must be $-i_{total} \cdot R$.

It seems that transimpedance circuit had not been previously used for transient space-charge-limited current measurements in thin films, although such a use was suggested[55]. One may hypothesize that the reason for this may be that real operational amplifiers used to be insufficient for this application. The amplifier needs to provide sufficient current measurement bandwidth and deal with initial capacitive displacement current spike. Current measurement bandwidth in given conditions is determined by operational amplifier gain-bandwidth-product. Initial current spike is likely to cause the overload conditions, that lead to saturation. This saturation must last as short as possible. This requires fast overload recovery. Thanks to progress in semiconductor manufacturing, current generation of operational amplifier chips is much better than previous generations in these aspects. These requirements will be discussed in detail in next sections.
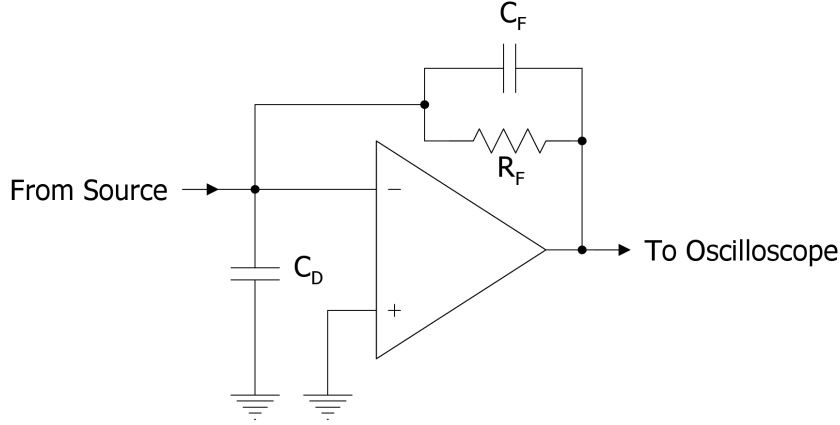
FIGURE 4.3.1. Detailed drawing of transimpedance amplifier circuit, with feedback capacitance C_F and source capacitance C_D marked.

4.3. Bandwidth and stability

The transimpedance amplifier circuit is presented in more detail on fig. 4.3.1. The elements critical for its behavior are source capacitance C_D, feedback resistance R_F and feedback capacitance C_F. In the case of application to space-charge-limited current measurement, source capacitance can be approximated as

$$C_D = C_{IN} + C_S + C_0$$

, where C_{IN} is the operational amplifier input capacitance. If cable lengths are minimized, sample geometric capacitance C_0 may be the dominating part in the sum. On the other hand, the influence of C_0 may be not so important, due to impedances present in the loop between operational amplifier inputs that contains sample (ie. R_S). Nevertheless, the worst case estimation of C_D is as given.

In this section, maximum stable bandwidth obtainable for given values of R_F and C_D is calculated. These are obtained by using Barkhausen stability criterion. Real operational amplifier is characterized by finite gain A and phase delay. This gain, multiplied by transfer function of the feedback path β, gives loop gain $|A\beta|$. If $|A\beta|=1$ and phase shift around the loop is multiple of 2π, then stable oscillation may occur. If this takes place, then the circuit behaves as an oscillator. In order to assure the amplifier function, it must be ensured that the conditions necessary for oscillation are not satisfied for any frequency f.

For the case of transimpedance amplifier, the criterion is solved graphically in most references. More accurate treatment requires numerical solution. The calculation presented here is simplified and somehow incomplete. It is intended only to illustrate the relation between the circuit conditions R_F, C_D and bandwidth f_c and feedback capacitance C_F.

Let's denote by Z_F the feedback impedance of the amplifier

$$(4.3.1) \qquad Z_F = \frac{1}{\frac{1}{R_F} + sC_F} = \frac{R_F}{1 + sR_FC_F}$$

where $s = i2\pi f$. Following ideal operational amplifier model, $U_{out} = -i_{total}Z_F$, the transimpedance cutoff frequency f_c is given by

$$(4.3.2) \qquad f_c = \frac{1}{2\pi R_F C_F}$$

. In order to investigate the stability, we look for solution of the equation $|A\beta|{=}1$. The open loop gain of a real operational amplifier can be approximated as

$$(4.3.3) \qquad A = \frac{GBW}{f}$$

where GBW denotes the gain-bandwidth-product of the operational amplifier. The transfer function of the feedback path β is

$$(4.3.4) \qquad \beta = \frac{Z_S}{Z_F + Z_S}$$

where $Z_S = \frac{1}{sC_D}$ denotes impedance due to the source capacitance.

It is common practice to look for solution of $|A\beta|{=}1$ graphically. The feedback transfer function approaches $\beta \to 1$ in the low frequency limit, and $\beta \to \frac{C_F}{C_D+C_F}$ in the high frequency limit. It can be shown that in fact, for frequencies above f_c there is

$$(4.3.5) \qquad \beta(f > f_c) \approx \frac{C_F}{C_D + C_F} \approx \frac{C_F}{C_S}$$

The second approximation comes from the fact that normally $C_F \ll C_D$. Because A is monotonously decreasing in function of frequency f, and $1/\beta$ is non decreasing, only one solution of the equation $|A\beta|{=}1$ exists. Taking the phase relations into account, it may be shown that sufficient phase margin exists at f_c. Therefore, it is safe to design the circuit in such a way that $|A\beta|{=}1$ is satisfied at the frequency f_c:

$$(4.3.6) \qquad \frac{GBW}{f_c} = \frac{C_D}{C_F}$$

This immediately leads to the following formulae for achievable bandwidth f_c and corresponding feedback capacitance C_F

(4.3.7)
$$C_F = \sqrt{\frac{C_D}{2\pi R_F GBW}}$$

(4.3.8)
$$f_c = \sqrt{\frac{GBW}{2\pi R_F C_D}}$$

The calculation above is approximate and conservative. Much larger f_c can be achieved at the cost of lower phase margin. However, the formulas illustrate well the main properties of the transimpedance amplifier. The cutoff frequency is set by circuit elements R_F and C_F. C_D has no direct effect on the bandwidth, however, it limits the maximum value, by imposing a limit on minimum C_F and maximum cutoff f_c for which stable function is guaranteed. This limit however also depends on GBW of the amplifier used. Simply using operational amplifier with larger GBW will increase bandwidth available in given conditions. As for modern devices, this parameter spans between approximately 15 to 1500MHz. Therefore, large differences in bandwidth exists depending just on the choice of the operational amplifier used. This range is even larger when taking older chips into account. Some of them are characterized by GBW well below 1MHz. These older devices were rather unsuitable to fulfill bandwidth requirements for space-charge-limited current transient measurements on thin organic films.

4.4. Initial saturation

The relation between achievable transimpedance bandwidth and source capacitance is well known. Since transimpedance circuit is very important, it can be found in most electronics textbooks and in datasheets of probably all operational amplifiers intended for transimpedance applications. Transimpedance amplifiers are usually used in conjunction with photodiodes. Photodiodes, like thin organic films, have significant capacitance, and similarly maximum bandwidth is desired. However, photodiodes are biased with constant voltage and there is no capacitive displacement current contribution. In the case considered in this work, there will be capacitive displacement current spike at $t = 0$.

The displacement current contribution will pose a problem. It must not be forgotten, that real operational amplifier are supplied by finite voltage. This voltage is $\pm 5V$ for newer designs, and does not exceed $\pm 15V$ unless for special designs. Operational amplifier output voltage is unavoidably limited by the supply voltages. Therefore, maximum current flowing through the feedback loop is limited to

$$I_{sat} = U_{sat}/R_F$$

, U_{sat} denoting saturation output voltage. Since the charge Q_0 displaced on the geometric capacitance of the sample upon application of voltage step is simply

(4.4.1)
$$Q_0 = C_0 V$$

saturation time can be estimated as

(4.4.2)
$$t_{sat} = \frac{Q_0}{I_{sat}} = \frac{C_0 V R_F}{U_{sat}}$$

. The simplest way of reducing saturation time is by reducing R_F.

The simple situation considered above neglects that the current may actually flow through real operational amplifier input. This current is however negligible as long as input node voltage is below clamp voltage U_{clamp}. The clamp voltage depends on operational amplifier input protection circuitry. If amplifier inputs are protected by enforcing maximum potential difference between them, U_{clamp} is equal to voltage drop on conducting diode ($\sim$ 0.6V). Otherwise, inputs of modern amplifiers are protected by enforcing that they won't exceed supply voltage. In such a case, U_{clamp} is close to the supply voltage. If nonnegligible current would flow through operational amplifier input, displaced charge can be estimated as $Q_0 = U_{clamp} C_D$. This is because when diodes cease to conduct, source capacitance is charged to voltage U_{clamp}.

The saturation time is dead time from point of view of the measurement. During it, no information about input signal is obtained. Saturation conditions are abnormal from point of view of operational amplifier. In fact, the real amplifier may take additional time to return to normal operation, further prolonging dead time above t_{sat}. This is the reason why physical operational amplifiers and comparators are distinguished despite being conceptually the same device. In order to ensure that the amplifier will return to normal operation immediately after t_{sat}, it is necessary to use an operational amplifier with fast overload recovery feature. Even so, in order to verify the approach presented here, it was checked that no signal distortion follows t_{sat}.

4.5. Practical realization

The transimpedance amplifiers suitable for measurements of space-charge-limited currents must be characterized maximum possible bandwidth for samples of moderate capacitance $\sim 100pF$. Commercial transimpedance amplifiers are usually maximally optimized either for bandwidth or for sample maximum possible sample capacitance at the expense of the other. Furthermore, fast overload recovery is essential. Since this feature is usually not critical, manufacturers of assembled devices usually do not even specify this in the datasheet.

It is in fact reasonably easy to build the transimpedance amplifier in-place. Since transimpedance amplifier circuit is not particularly complex, this can be done at reasonable amount of effort. By doing this, very good bandwidth-source capacitance tradeoff can be realized. Furthermore, if there are problems or unexpected behavior, these are easier to solve.

For the work presented, three transimpedance amplifiers were built with gains $R_F = 10^3, 10^5, 10^8, 10^9 \Omega$. The operational amplifiers used were ADA4817 (Analog Devices) in the first case and OPA657(Texas Instruments) in the other cases. These devices are characterized by very high gain-bandwidth-product, being 410MHz for the first and 1.6GHz for the second. This comes with excellent properties. Thanks to JFET inputs they are characterized by very low input bias current ($\sim 1pA$ at room temperature). Together with maximum input offset voltage below $1mV$ it practically eliminates the zero error in current measurement along with its possible temperature and long term fluctuations. Furthermore, the noise density is quite low. In comparison with older designs, the only one worse parameter is the supply voltage, which is $\pm 5V$ in both cases.

The devices with transimpedance $R_F = 10^3, 10^5$V/A are built according to the trivial schematic. Power supply is provided by voltage regulators. Care for power supply bypassing was taken.

It must be commented, that since the operational amplifier used are wideband devices, they are prone to oscillation. The stability analysis presented in previous section does not take neither fully into account the feedback loop or open loop bandwidth gain of the amplifier. The devices have gain at frequencies above 100MHz. In the radio frequency range, all parasitic capacitances and inductances become critical. Most of the difficulties of the amplifier construction is associated with ensuring stability. In order to do so, it is firstly important to keep the circuit geometrically as small as possible. Radio frequency practices must be observed, especially concerning the use of ground plane. Often, it is useful to ensure that minimum amount of C_D is indeed connected to the input of amplifier. Lastly, it is critical that operational amplifier power supply lines are appropriately bypassed with capacitors. Without proper bypass capacitors, the circuit may oscillate due to parasitic feedback involving power supply line.

In the case of $R_F = 10^3$V/A, C_F is provided by a discrete capacitor; in the case of $R_F = 10^5 \Omega$, the feedback capacitance is the parasitic capacitance of the resistor itself. In the cases with highest gain, effective C_F is reduced below parasitic resistance of by use of a special feedback network, shown in fig. 4.5.1. In the figure, Cf and Rf represent parasitic capacitance and resistance of the feedback resistor. If $R3 = 0$, then R2,C1 form a low pass filter and Cf,Rf form a high pass filter. R2 is chosen to be much smaller than Rf. If $R_2 C_1 = R_f C_f$, then whole network behaves as ideal resistor Rf. In practice, some effective feedback capacitance
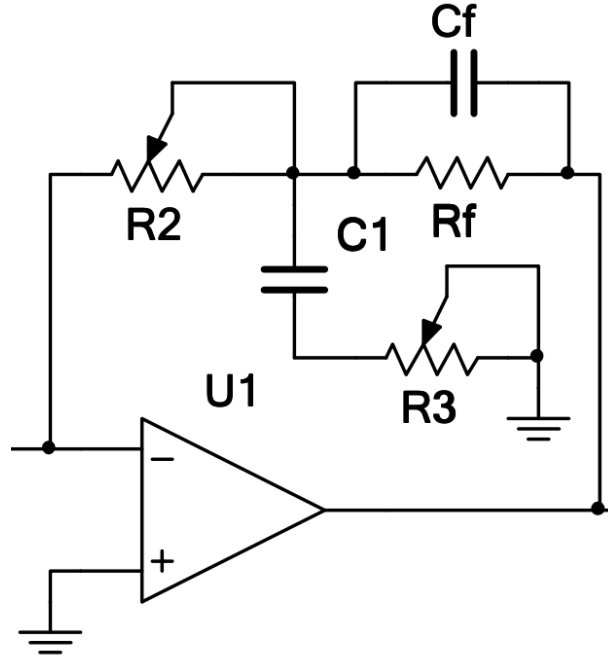
64

FIGURE 4.5.1. *Feedback loop for reducing effective parasitic capacitance Cf of the feedback resistor.*

is required for stability and the function of R3 is to permit adjustment of effective Cf to be nonzero. Such a network indeed permits great reduction of effective Cf [56].

With increase of R_F, screening of the amplifier and sample becomes increasingly important. At $R_F = 10^3\Omega$ screening can be considered as optional. However, at $R_F = 10^5\Omega$ screening provides evident improvement of signal-to-noise ratio. For R_F around $10^8\Omega$, it is not useful to turn the circuit on without screening as noise alone will suffice to saturate it. For the same reason, for $R_F \geq 10^8\Omega$, we decided to use batteries as power supply in order to avoid problems with power supply noise.

Fig. 4.5.2 presents full schematic of the transimpedance amplifiers in the general form. Since parasitic capacitance is not a problem for $R_F<10^6$, the compensation in feedback network is skipped (R2=0 and C1 is open).

4.6. Characterization

The goal of characterization of a transimpedance amplifier described here is to verify the proper functioning of the circuit, and to measure the cutoff frequency, or equivalently, the rise time.

The verification most naturally starts with DC characterization, which is made by connecting voltage source and resistor to the transimpedance amplifier input. Knowing that the input node should be kept at ground level, there must be linear relation between input voltage on resistor and output voltage of the amplifier in the operating current range of the
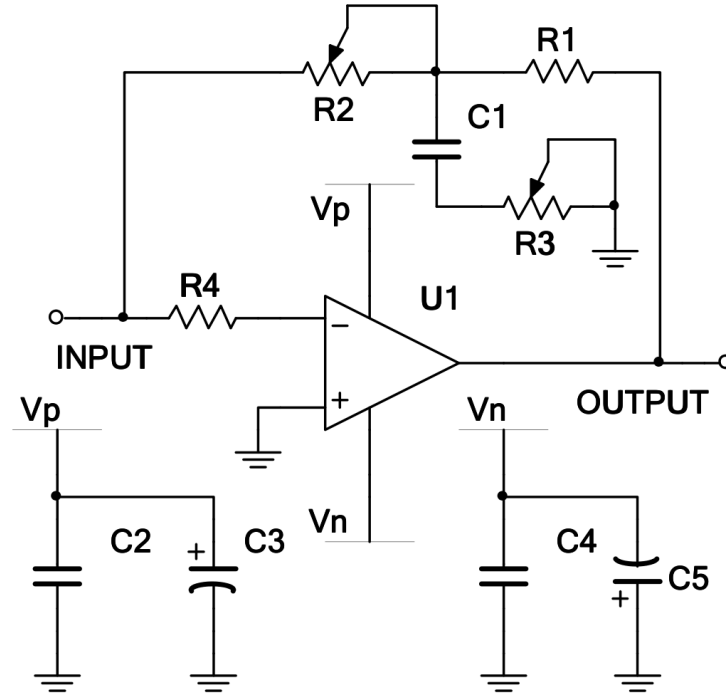
FIGURE 4.5.2. *General schematic of transimpedance amplifiers built. Vp, Vn denotes positive(+5V) and negative(−5V) voltage supplies, respectively. C2 − C5 are power supply decoupling capacitors. The ceramic high frequency capacitors, $C2, C4 = 100nF$ are be placed as close as possible to the operational amplifier. The low frequency capacitors $C3, C5 = 10\mu F$ are tantalum. The feedback network $R1 = R_F$ is the main feedback capacitor. R4,R2,R3,C1 are present only in the case $R_F \geq 10^8 \Omega$.*

amplifier. The linear relation appropriate for resistor values and operational amplifier ratings should be perfectly fulfilled.

Transient characterization is conveniently performed with a current source made of voltage signal source and a capacitor. Using capacitor is much better than using resistor, because resistors' parasitic capacitance dominates high frequency response yet is not well controlled. On the other hand, high quality capacitor has well defined value of capacitance while its resistance can be considered infinite.

Checking response to square current wave is done by applying triangular voltage wave to the capacitor. Similarly, checking impulse current response is done by differentiating square wave on the capacitor. In the case feedback loop has adjustable components for given feedback resistor, the regulation is performed to optimize the transient response.

The measurement of cutoff frequency itself is done either from rise time, or by applying sinusoidal wave through the capacitor.

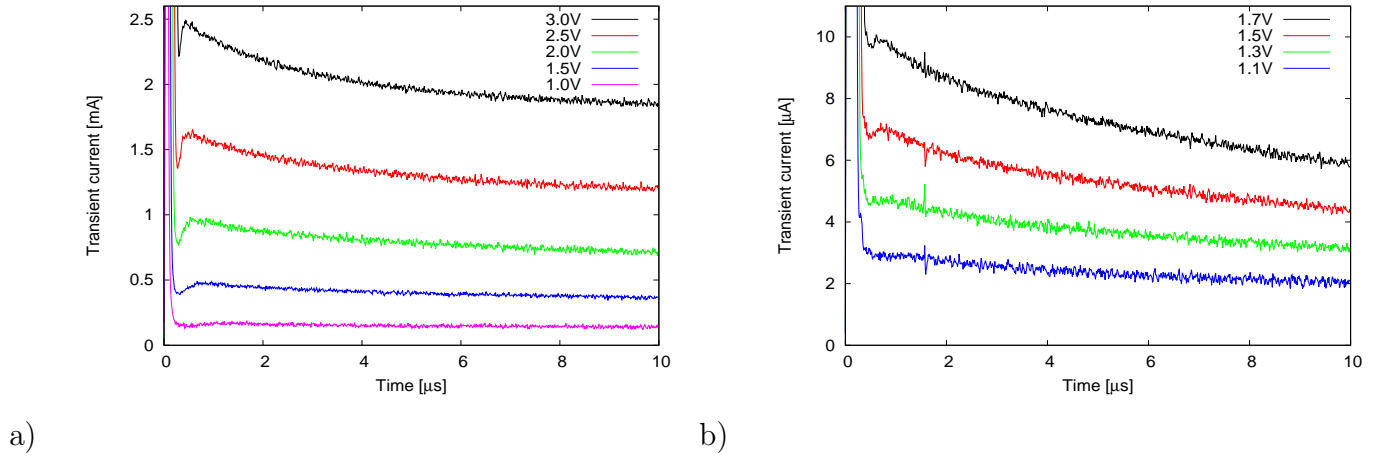a)   b)

FIGURE 4.7.1.   *Transient responses of 200nm ITO/PEDOT:PSS/60PCBM:polytriarylamine/Al sample: a) electrode area 0.8mm², recorded using transimpedance $R = 10^3\Omega$; b) electrode area 0.01mm², recorded using transimpedance $R = 10^5\Omega$.*

4.7. Verification

The main question concerning applicability of transimpedance amplifier for measurement of space-charge-limited current transients is whether transimpedance amplifier can recover from saturation quickly enough after the initial displacement current spike. In particular, it is very important if there is no output signal distortion following saturation conditions. Output signal distortion may move apparent position of the peak. Furthermore, as such a distortion is not guaranteed to be monotonous, it may even create apparent current peak coming not from space-charge-limited current response, but from the amplifier itself.

Since the effects of saturation depend critically on transimpedance gain R_F (eq. 4.4.2), we have decided to verify the approach by comparing measurements obtained on single layer but with different electrode areas using different amplifiers. The transient responses obtained are on shown fig. 4.7.1. The voltage range for which they may registered in each case was limited by amplifier sensitivity on the low side and by saturation time on the high side. Nevertheless, extracted mobilities are in perfect agreement, as seen on fig. 4.7.3.

Detailed comparison of experimental curves 4.7.2 obtained with different transimpedance values shows perfect agreement in peak position. The curves differ by the rate of decay. This can be explained by that they were taken in different parts of the sample. As spin coating process was used, these different parts could be differently affected by the trapping effects.

Initial saturation does not evolve as predicted by 4.4.2. This because the formula assumes idealized voltage step. At low times, of order 100ns and less, in our setup there were additional effects which increase voltage step setting time.
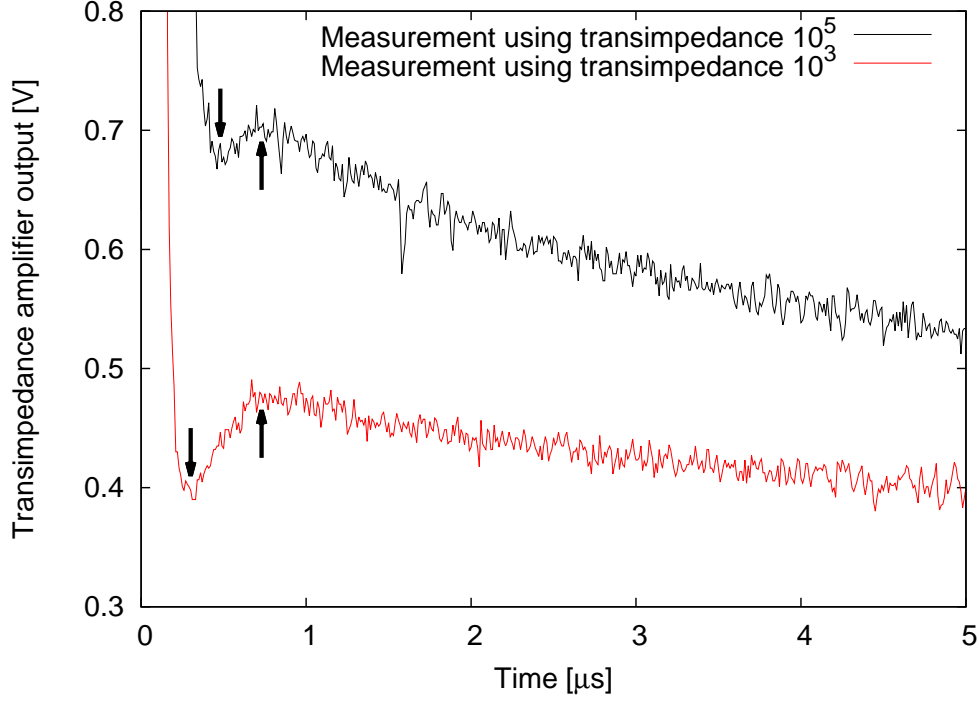
67

FIGURE 4.7.2. *Detailed comparison between transient responses of different regions of the same sample, registered using different transimpedance amplifiers . Upward pointing arrows denote Many-Rakavy peak time $t_{max} = 740ns$. Downward arrows denote end time of initial saturation, after which valid current measurement takes place.*

4.8. Conclusions

In the section, the difficulties with performing space-charge-limited current transient measurements were analyzed. These difficulties are caused mostly by sample geometric capacitance. In order to minimize its effects on the measurement, the bridge circuit (fig. 4.1.1) is frequently used. The bridge circuit permits for subtracting capacitive displacement current contribution from the measured signal, making it easier to identify the space-charge-limited current peak.

In the work, easier approach was investigated by using transimpedance amplifier circuit. The transimpedance amplifier converts measured current to voltage signal directly. Most importantly, it is doing so without introducing serial resistance into the circuit. However, the measurement using transimpedance amplifier is also affected by the displacement current contribution. The capacitive displacement current is expected to introduces overload condition, potentially leading experimental deadtime and possibly to distortion to measured
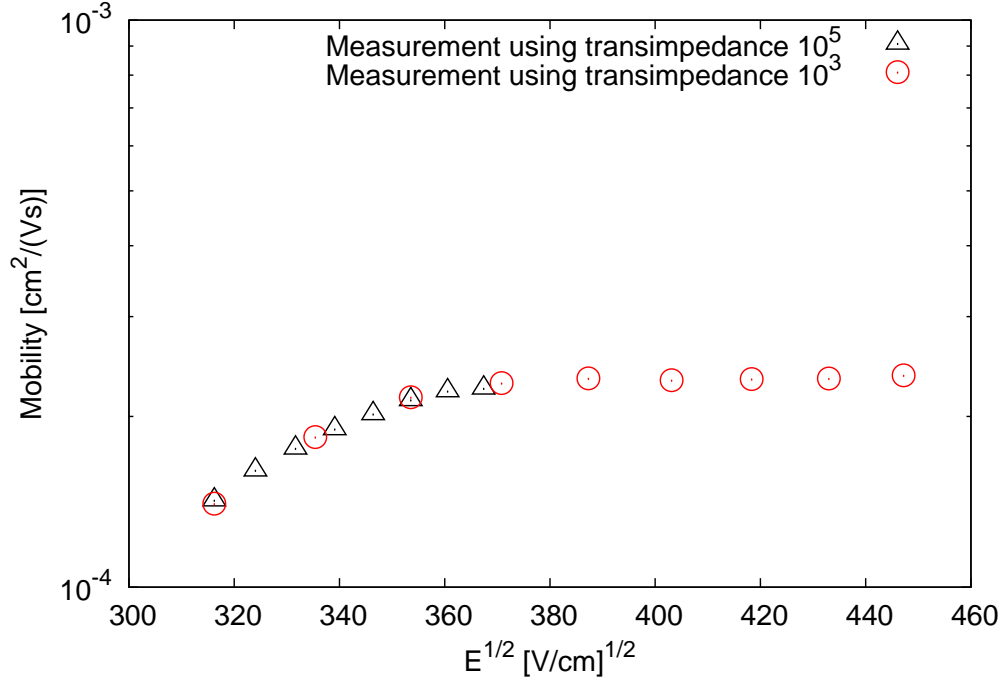
68

FIGURE 4.7.3. *Extracted mobility values in the 200nm 60PCBM:polytriarylamine blend thin film investigated.*

responses. It is shown, on example of electron transport in PCBM in a PCBM:PTAA blend device, that these effects do not prevent the measurements. The peak time was shown to be independent of transimpedance using the designs under consideration. Therefore, the approach proposed may be trusted for mobility extraction.

It is notable that the transimpedance amplified based approach, in comparison with bridge circuit, removes the needs for sample specific adjustment while offering better current sensitivity, and ultimately, permitting faster measurements. The removal of per-sample adjustment is particularly convenient, because it was reported to contribute to measurements uncertainty [2].

In the section, it was omitted that some circuit strategies permitting for reducing experimental dead-time further(ie. US patents 4623786, 6897731 and WO/2009/123845). It can be done also in the case of very high transimpedance values such as 10^8V/A[57].

CHAPTER 5

Results obtained on one triarylamine based dendrimer

The results of transient measurements presented in the previous section were obtained on the well known material PCBM in a PCBM:PTAA blend device. They were mainly intended as a proof of feasibility of our experimental approach. This section presents the results of characterization of a less known material which is a triarylamine based dendrimer. The measurements are performed using transimpedance amplifier based setup and interpreted in a classical way, based on the Many-Rakavy theory([9], section 1.7). The content of this section corresponds rather exactly to our published work, ref. [39].

Chemical formula of the dendrimer material available for this work is shown in fig. 5.0.1. Such a compound resembles to more known ones such as 2TNATA[6]. These molecules were proposed for organic electronics applications. However, they are processed by evaporation and are weakly soluble. The dendrimer under investigation (noticed as DT1Bu6 in the following) here was intended to be solution processible thanks to the presence of peripheral butyl groups absent in the similar molecule synthesized few years ago by Hartwig et coll. [58]. Moreover, we were mostly interested to investigate highly branched molecules which are not supposed to easily form crystalline phases. Thus, we should deal with molecules forming disordered layers when deposited on a substrate. This lowers the possibility to have some preferential direction for the electronic transport. Finally, it has been shown that in such materials, it is possible for charges in excess to be transported from the core to the crown of dendrimer provided some high dynamic disorder exist. This thesis is fully included in such a research framework whose ultimate goal is to understand how charges are displaced in such branched and disordered media and what order of magnitude of charge mobility can be expected. Following the results of previous electrochemical and chemical characterizations, as well as by analogy to the similar compounds, the dendrimer investigated was expected to be a hole conductor.

5.1. Sample preparation

As electrical transport in Dt1Bu6, unlike PCBM, has never been studied, there is none published work describing the best way to depositing it as a layer on a substrate. Therefore, certain amount of effort was devoted to develop a proper sample preparation method. It was decided to concentrate the efforts on the spin-coating technique to deposit the material from solution. Because we could not very accurately control the ambient conditions while
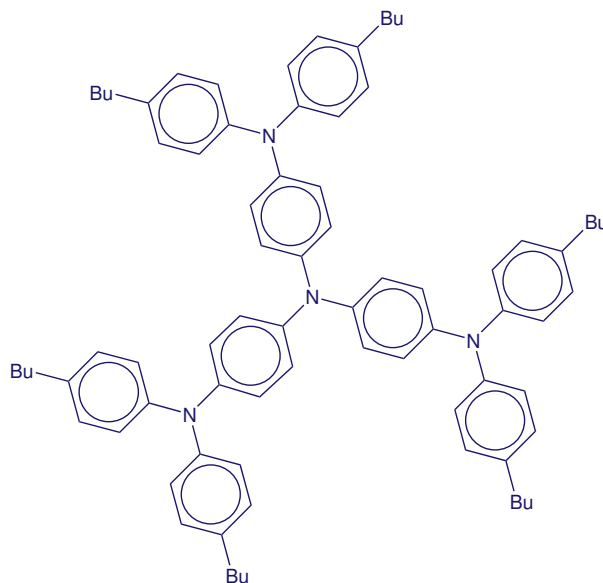
FIGURE 5.0.1. *Dendrimer molecules under consideration.*

spin-coating the material, the work of optimization of the deposition is certainly incomplete. Especially, we noticed that small changes in ambient temperature and humidity may affect the deposition process significantly. We describe below the procedure from which we have obtained the best results.

From results of cyclic voltammetry measurements(see Appendix 1), as well as by analogy to similar compounds, it was expected that the dendrimer will form ohmic contact with gold for hole injection. The estimated HOMO level (-4.9 eV) was not far from workfunction of gold, which is 5.1eV. Therefore, gold was naturally chosen as the electrode material. This is a convenient choice, as it is a metal which does not undergo oxidation in ambient atmosphere. It is reported that oxidation can significantly affect the performance of electrodes[59]. Despite this, it was reported that even the performance of gold electrodes may strongly depend on electrode treatment[6]. Therefore, in the preparation process the greatest care was given to the stages related to electrode preparation.

The samples were prepared in the following way. Firstly, glass substrates were cleaned using the standard procedure. The glass substrates were microscopy slides. After cutting, they were cleaned manually in a detergent and dried. Next, the slides were put in acetone in ultrasonic bath for 15min and rinsed with distilled water. Next, the substrate were put in isopropanol in ultrasonic bath for 15 min and after were rinsed in distilled water, and put again in fresh isopropanol. At this stage they were kept in sealed glass until actual use. They were dried only immediately before to be used with an argon gun.

Bottom gold electrodes were evaporated on the glass substrates using evaporation system under a pressure of 3×10^{-6} mbar. The electrodes were shaped as thin strips and their thickness (typically $50nm$) was controlled using piezoelectric quartz . The operating principle

of the evaporation was by Joule heating effect. The gold electrodes were evaporated directly on glass. The substrates provided with such gold electrodes were kept under vacuum until the next preparation step.

For spin-coating 1.2×10^{-2}M solution of DT1Bu6 was prepared. As a solvent, freshly distilled tetrahydrofurane (THF) was used. In order to ensure that the materials has dissolved completely, solution was bar stirred for 5 minutes at room temperature . Just before spin-coating, the glass substrates with electrodes were removed from evaporator and put under UV treatment (Novascan PSD Pro) for 5 min, at temperature of 100°C. Then, substrates were let to cool down to room temperature and deposition was performed. Spin coating was performed using SPIN150 instrument in ambient atmosphere (room temperature was ~ 24°C). The process took place in two phases. The distribution phase was programmed to last ten seconds, with an angular velocity of 500rpm to be reached under an angular acceleration of 100rpm/s. The second phase lasted ten seconds with the same angular velocity 500rpm.

By slightly varying angular velocity of the distribution phase, changes in the sample thickness were obtained. Along with the active layer with electrodes, reference layers on bare glass substrates were deposited as auxiliary samples for thickness measurement.

As the last step of the sample manufacturing process, top gold electrodes were deposited. They were in the form of gold strips, perpendicular to the bottom ones. As on top and on bottom two strips were deposited, four samples were obtained on each substrate. The evaporation took place under the same conditions as for the bottom electrodes. Top electrode thickness was 100nm and deposition speed 0.1nm/s.

Copper wires were then sticked on gold contacts using a conductive epoxy glue (Chemtronics CW2400). This way, permanent and very reliable electrical connections were obtained. The conductive epoxy was preferred over standard silver paste for its several advantages. It does not dry and no solvents are released. Unlike silver paste, it has excellent mechanical strength and very good adhesion to glass. Because insulator was measured, the contributions to the resistance by the conductive epoxy could be considered as negligible.

The samples with conductive epoxy was cured at 40°C for 4 hours. Initial electrical characterization was performed immediately after finishing the manufacturing process. The characterization of steady-state type, and was intended to give point of reference for tracking possible further aging processes. The current-voltage curves exhibited excellent repeatability and symmetry. This second property confirmed that top and bottom electrodes are equivalent despite different deposition.

Sample thickness measurements were performed using Ambios-Technology XP-2 stylus profilometer. The knowledge of layer thickness is critical for mobility estimation, yet non-trivial in the case of presence of narrow bottom electrodes. In order to ensure that the value

is as accurate as possible, two independent measurements were compared in each case. For given spin-coating conditions, thickness was measured on reference glass without electrodes and on sample surface. In the second case, the line of scan was perpendicular to the electrode strip. On the glass, the layer thickness was the same in both cases. However, in the case of layer parts on top of bottom electrodes, the layer was elevated by approximately 10nm less than thickness of the bottom electrodes. The estimated layer thickness on electrode, rather than on glass, was assumed to be sample thickness. Selected thickness measurements were confirmed using AFM (Nanosurf Mobile S).

The sample area measurements were performed on basis of low magnification microscopic images. As flexible evaporation masks were used, the shape and dimensions of evaporated electrodes did not match perfectly that of mask design. Therefore, it was desirable to use image based area estimation.

Dielectric constant measurements were done using Agilent 4294A impedance analyzer. Dielectric constant is estimated by capacitance measurement. Although impedance analyzer is perfectly suited for measuring capacitance, ac response of organic sample differs considerably from that of capacitor. It was concluded that the usual value of $\epsilon_R = 3$ may be assumed as relative dielectric permittivity. A more precise measurements would require specific sample preparation and was not performed.

5.2. Single transient measurements

The electrical characterization was started by stationary current-voltage curve measurements. The results obtained for sample of thickness 300nm are shown in fig. 5.2.2. The current voltage characteristics exhibit approximately a quadratic dependence of current on voltage, reminiscent of the Mott-Gurney law. The measurements were performed for voltages not exceeding $2.0 - 2.5V$, corresponding to a maximum electric field of order $10^5 V/cm$. At higher voltages, sample failure (by shorting) was found likely and therefore no risk was taken by applying larger bias. This kind of problem is most likely associated with electromigration of gold through the organic layer. The dendrimer layer is in fact relatively soft at room temperature. It is particularly noticeable during use of stylus profilometer, when lowest possible applied force had to be used in order to avoid damage to the organic layer.

Transient response curves are presented in fig. 5.2.1. For readability, the figures are displayed in double logarithmic scale. Logarithmic scale for time axis permits a better visualization of the long time scale evolution of the signal, due to the trapping processes. The current is scaled in arbitrary units in order to emphasize that the analysis is independent of actual current values. The actual absolute values of current density can be obtained simply by considering the stationary case (fig. 5.2.2). Initial part of transient responses, below $10\mu s$, has been discarded because at the time it was considered by us as unreliable.

5.2. SINGLE TRANSIENT MEASUREMENTS

The classical analysis starts with comparing experimental transient responses in fig. 5.2.1a with basic theoretical predictions, given in section 1.7, repeated in fig. 5.2.1b for reference. The time position of the peak corresponds to the time necessary for carriers injected at $t = 0$ to arrive on the opposite electrode. Therefore, the distinct feature of transient space-charge-limited current is a peak that occurs at decreasing times when voltage is increased. This property is very important for ensuring that indeed one transient space-charge-limited current response is being observed. Other transient effects may give rise to a maximum in the observed signal shortly after application of voltage at fixed time. Although in principle mobility can be extracted from just one current response, to prove that the transient space-charge-limited current is being observed, peak evolution with voltage has to be checked. Indeed, the current responses observed satisfy the formula (1.7.19), as shown in fig. 5.2.1a. For clarity, only three curves are drawn. Responses for intermediate voltages were measured, but transition between them is rather smooth. The curves were measured without averaging. The shape of these curves deserves some comment. The long decay following current peak is due to trapping. Theoretical prediction of current responses, ignoring thermal release of trapping carriers, is shown in fig. 1.7.1. By comparing experimental and theoretical responses, it can be seen that the effect of trapping, the duration of current decay in particular, decrease with increasing voltage. For the case of a 2V applied voltage, the experimental curve is very similar to the theoretical curve obtained for infinite trapping time $\tau = \infty$. In particular, the peak shape and the ratio of peak and stationary currents are similar. In contrast to this, the shape of the experimental curve for applied voltage of 1V reminds that of theoretical calculated for $\tau \sim 1$. We observed no peaks for lower voltages. When trapping effects become more and more significant, the shapes of the transient profiles tend to a monotonic decay as predicted by the theoretical plot 1.7.1 for $\tau < 1$.

Once the peak position obtained, it is then straightforward to deduce mobilities by using the formula (1.7.19). A mobility value of $8 \times 10^{-6} cm^2/(Vs)$ has been obtained. We found that the formula is well satisfied , giving a constant mobility over electric field range 33-83 kV/cm. It was somehow disappointing, since the theories[42, 22] predict an increase of mobility with the applied voltage. On the other hand, in the published results of transient characterization, different evolution of mobility in function of voltage is presented. Theoretically predicted increase of mobility with applied voltage in space-charge-limited current transient experiment is presented in ref. [12]. But for example, in ref. [60] the mobility is constant, and in some reports even decreases with applied voltage[61]. In fact, in ref. [61], all cases occur in one single publication. Therefore, the constant mobility can be considered as a correct result.

Having estimated the mobility from the space-charge-limited current transient experiment, it is interesting to compare steady state current j_{exp} with its predicted value j_{scl}.
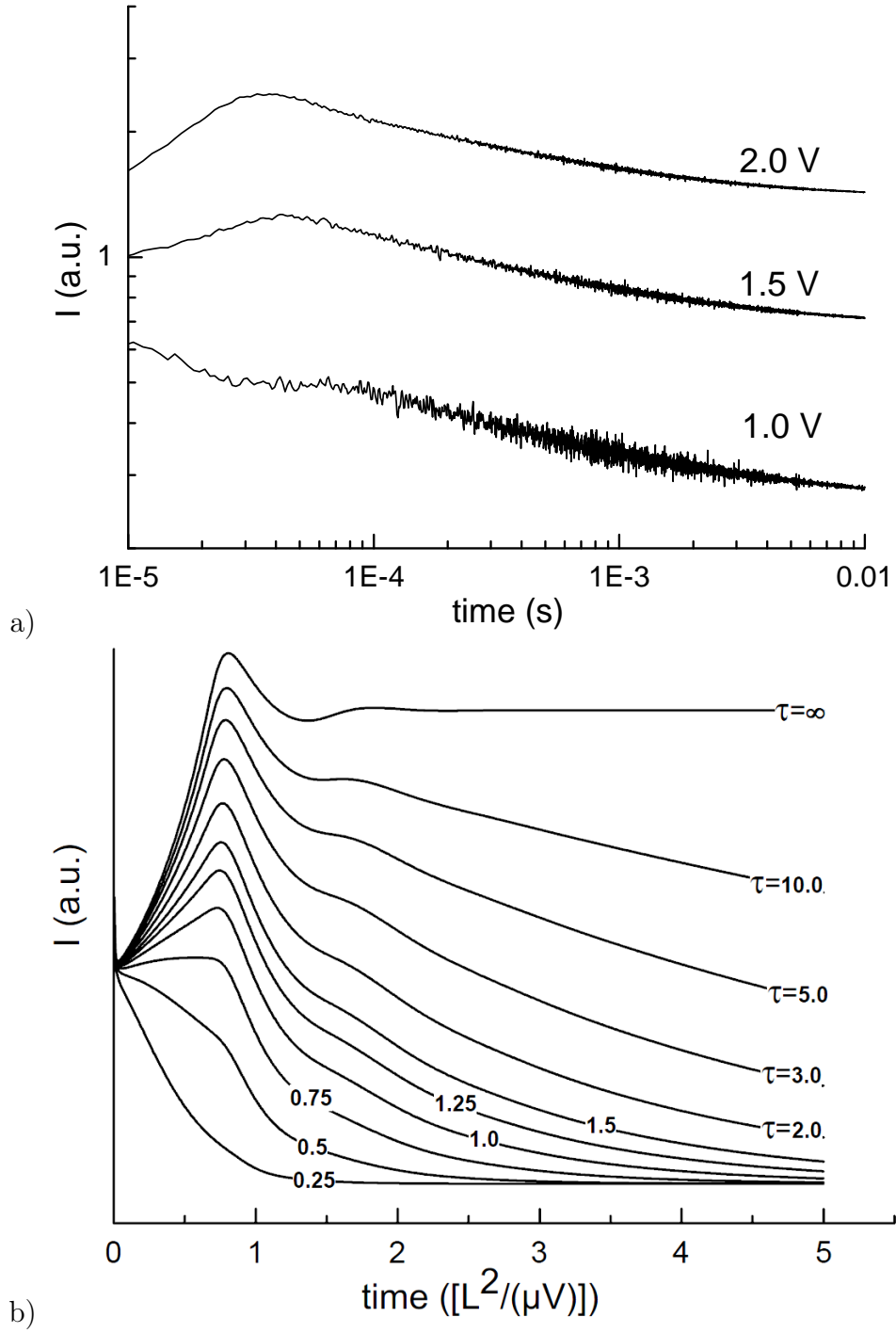
FIGURE 5.2.1. *a) Selected transient responses of the sample for voltages 1.0, 1.5 and 2.0V, obtained for a sample of thickness L = 230nm. b) Theoretical transient responses after [9](see section 1.7).*

In some works[62], contact efficiency is introduced, defined as the ratio of experimental to theoretical steady state current:
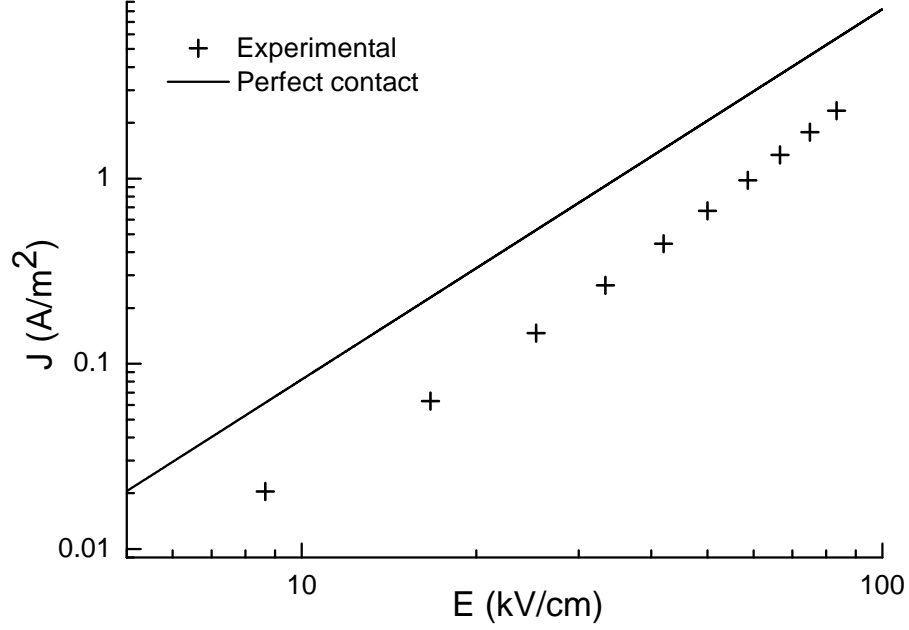
FIGURE 5.2.2. *Experimental current compared to the purely space-charge-limited current calculated from the measured mobility.*

(5.2.1)
$$\eta = \frac{j_{exp}}{j_{scl}}$$

. The theoretical current j_{scl} is usually calculated using the Mott-Gurney law. The comparison between the calculated current and the measured is shown in fig. 5.2.2.

Although simple to define, and often used as a figure of merit[63], so defined contact efficiency is not fully useful. It does not seem to have any real relation with a physically based contact or transport model, so it has limited use for predicting performance in different configuration. Also, it is difficult to properly estimate the true steady state current which would flow if the same sample was equipped with ohmic contact. Especially, the estimation of using Mott-Gurney law is inaccurate, by not taking into account diffusion, trapping etc. As a consequence, so obtained quantity is a function of voltage, as in example in ref. [61]. Therefore, although used, it may be concluded that better method of extracting contact properties from transient space-chage-limited current would be desirable.

We remark that we repeated the measurements on samples with slightly different thickness, and obtained similar mobility values. This additionally confirms both the interpretation of the current responses as space-charge-limited, as well as the estimation of the layer thickness. Although it may regarded as a trivial parameter, accurate sample thickness measurement with presence of bottom electrodes is nontrivial. Even penetration of gold into layer during evaporation may reduce effective layer thickness only below the top electrode. The current responses shown were well repeatable over time period of several weeks following
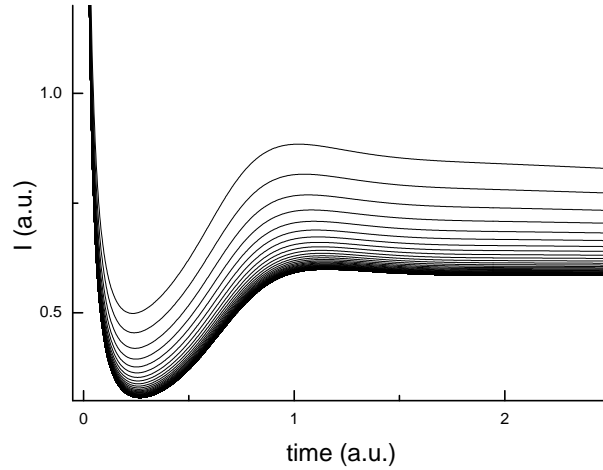
FIGURE 5.3.1. *Simulated sequence of transients obtained for fast (comparable with detrapping time) pulse sequence.*

production of samples. In spite of this, the results presented here seem to be suitable to a more advanced analysis that is presented in the next chapter.

5.3. Repeated transient measurements

Some authors have noticed, that if space-charge-limited current transients are repeated such that not enough time for sample relaxation is given, then different transient responses will evolve until dynamic equilibrium state is reached. This can be explained by the fact that after subsequent measurements, certain amount of trapped charge carrier remains inside the sample. If not enough time is given to the sample between measurements, they will accumulate. Therefore, the sample is being charged with the trapped carriers. These trapped charge carriers in turn reduce effective electric field, which causes both the reduction of the peak current and the increase of the peak time in subsequent measurements. The analysis of this phenomenon is given in ref. [37], where a formula for corrected voltage is proposed.

This effect was used to investigate trapping dynamics in iodine[37], conduction characteristics of chalcogenide thin film[64] and zinc oxide ceramics [65]. Recently it was pointed out that it pose problems for space-charge-limited current transient measurement[2] in thin organic films. In particular, if averaging is used, then trapping affects the estimation of the mobility in a complex way[66].

Importance of this effect was checked on the dendrimer samples. This was done by applying a square-wave with a 50%duty cycle at room temperature. It was found that the effect is indeed significant if square wave duration is below 300ms. The measurements are shown in fig. 5.3.2. These results were presented with sample simulation(fig. 5.3.1) in order to justify the interpretation of the evolution the responses. The detailed numerical analysis
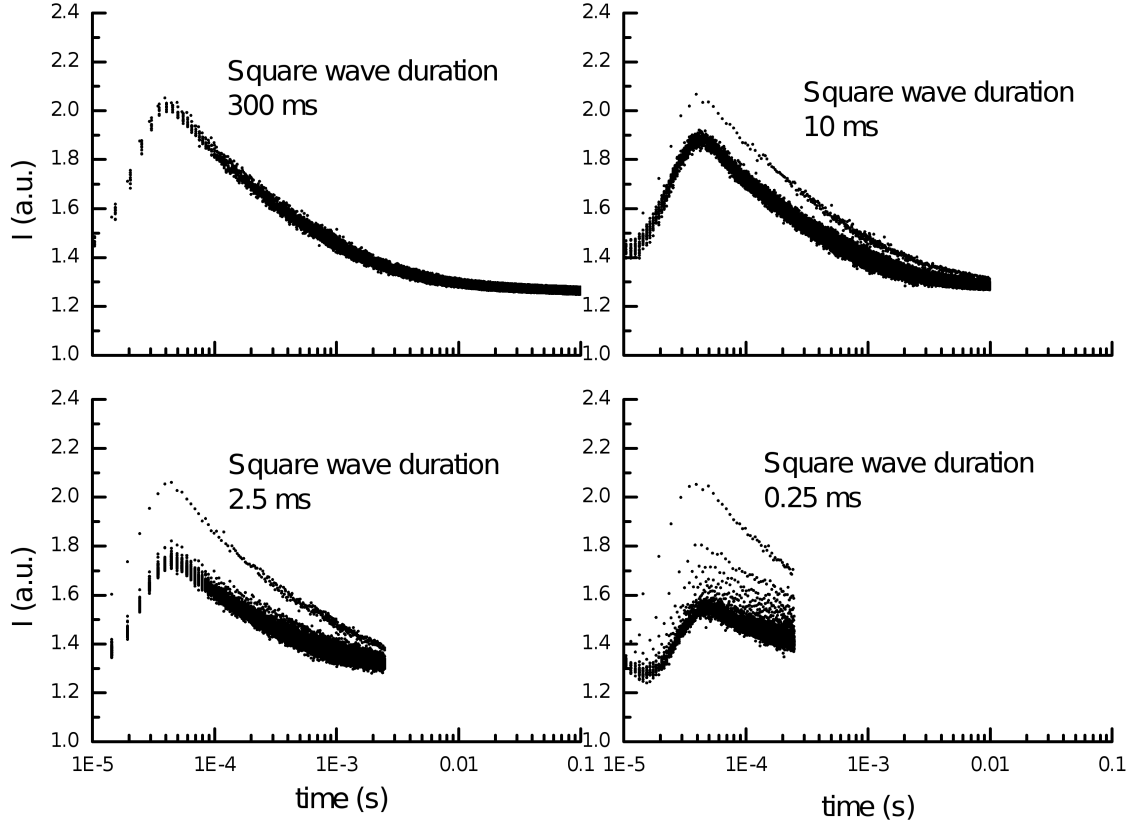
77

FIGURE 5.3.2. *Sequences of transients obtained for different square wave durations (duty cycle=50%).*

of the effect is difficult, because multiple subsequent transients must be simulated. Recently, such an analysis has been published ref. [66].

It is interesting to compare two sets of responses obtained for the same pulse trains. The sets obtained on the same sample are presented in fig. 5.3.3. With precision to measurement noise, they are exactly identical. This indicates that even sequences of space-charge-limited current transient measurements are well repeatable, provided that initial state is well defined.

5.4. Aging changes

All of the results presented so far in this chapter were obtained on fresh samples. This means, not later that two weeks after sample production and the samples were stored in atmosphere between measurements. During that period, excellent repeatability of the measurements were observed. After that, some samples were left for 5 weeks, in ambient atmosphere without any particular precautions concerning sunlight, humidity and oxygen. When they were measured again, large differences in transient response were observed. One typical example is presented in fig. 5.4.1. Both responses are for the same voltage 1V. The response of an old sample is denoted as aged.
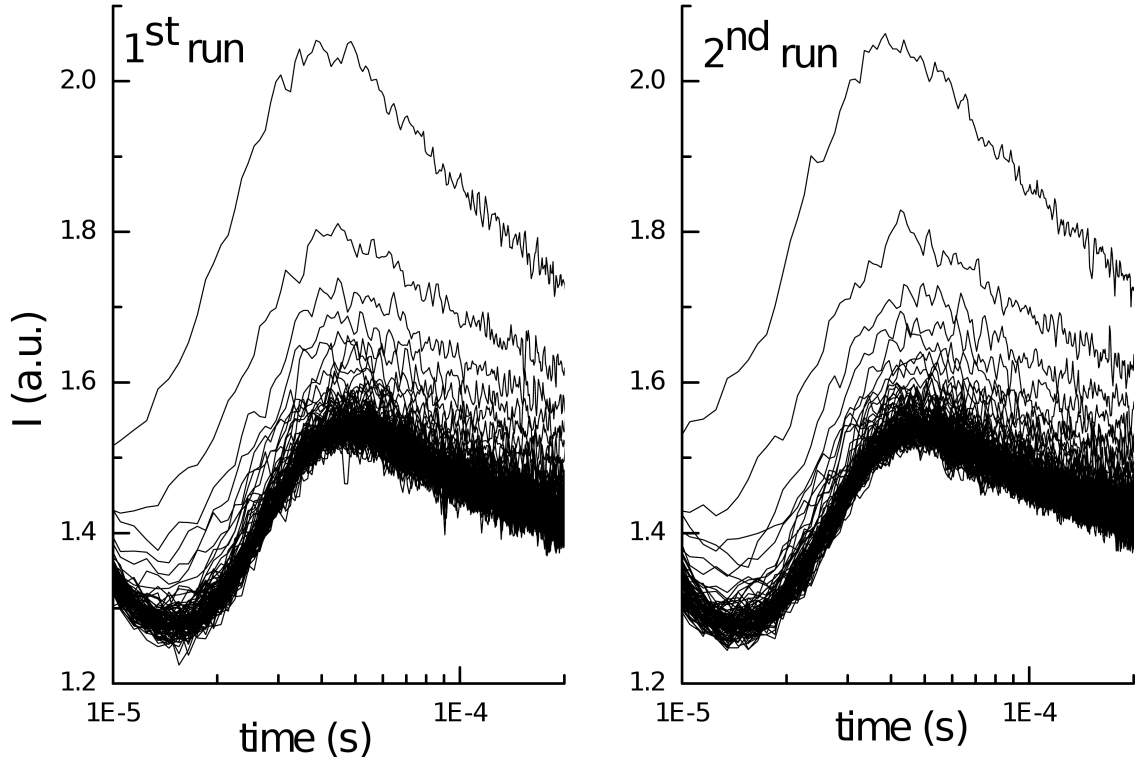
78

FIGURE 5.3.3. *Experimental sequence of transients obtained for fast (in comparison to detrapping time) square wave sequence.*

At first glance, the comparison reveals that the transient response of aged sample appears to be more affected by trapping. In the case of old sample, current decay is more profound and current peak is less visible, corresponding rather to the case $\tau/t_{max} \sim 1$ on fig. 1.7.1. This most likely indicates creation of trapping centres inside the material. Furthermore, at large timescales (>0.1s), fresh sample achieves steady state while in the case of aged sample there is still decay of the current. In fact, the decay of current in the case of old sample appears to be composed of two components, for long(>0.1s) and short(up to 0.1s) timescales respectively. The decay in short timescale seems to be similar to that of fresh sample, and is naturally introduced by trapping. The decay in long timescale does not have equivalent in fresh sample. It may be assumed that it is due to ionic conduction[12].

Note that, to the precision to which it can be estimated, the mobility has the same value. Contrary to what might be expected, there is no significant change in mobility observed due to sample aging.

Probably, the most interesting finding is that in aged sample the current density is higher. Knowing that introduction of traps reduces the current, and mobility remained unchanged, it seems that improvement of contact properties is the only possible explanation for this observation.
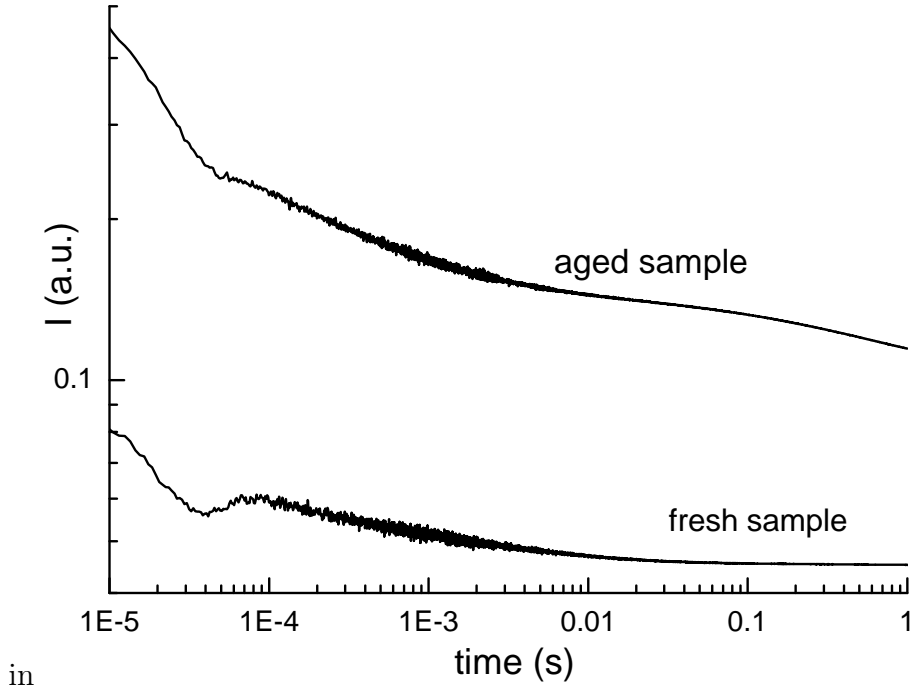
in

FIGURE 5.4.1. *Comparison between transient responses of fresh and aged samples.*

In fact, improvement of metal-organic contact electrical properties with time was reported in literature[7]. In[8], a rather chemical explanation is given, as follows. During electrode deposition, metal atoms damage top layers of organic molecules. Then, with time, molecules reorganize and better contact is obtained.

For the experimental results obtained here, another explanation is preferred, based on previously evoked theories of material metal organic contact. Assuming local thermal equilibrium at the interface, the interfacial charge carrier density in organic is given by overlap integral between the density of states in organic and occupied density of states in the metal. The trap states obviously contribute to the density of states in the organic material. If trap states have energy close to that of charge carrier in metal, while other states do not, then introduction of trap states can greatly increase the value of overlap integral, and so the contact properties.

In a microscopic view, introduction of trap states provides new charge injection path, which takes place in two steps. Firstly, charge carrier hops from metal to a trap state. Then, it is released from trap state to a conduction state. As the process takes the required energy in two parts, it might be easier than direct hop from metal to conduction state.

5.5. Conclusions

Using transient space-charge-limited current transient experiment, hole transport in newly synthetized triarylamine dendrimer was characterized, for field value up to 10^5kV/cm under

space-charge-limited current conditions. We found a mobility value of $8 \times 10^{-6} cm^2/(Vs)$, which is close to the value obtained in similar compounds[6]. Also using the same technique it was found that gold forms quasi-ohmic contact with the dendrimer, with a efficiency around $\eta \sim 0.4$. This observation is further supported by comparison between fresh and aged sample. In the case of aged sample, contact efficiency is better. This surprising result has been observed previously[7, 8]. In the case of dendrimer, it is attributed to trap formation. The formation of traps was also confirmed by the results. Other aging effects seemingly include introduction of ionic impurities, giving rise to long scale (>0.1s) current decay. Therefore, using space-charge-limited current transients, it is not only possible to obtained a relatively complete characterization of electric properties of a new material, but also to gain insight in the sample evolution.

In addition to these, we attempted observation of trapping effects by repeating space-charge-limited current transient measurements. We found that the results are in qualitative agreement with results of simulation, supporting the assumed explanation of the process. It was found that the responses are well repeatable, if consecutive measurements are separated in time by a sufficiently long waiting period (in the case considered $\sim 0.3s$). If this is satisfied, even responses to long and complex pulse trains are very well reproduced . Therefore, averaging can be used for improving signal to noise ration even in pump-probe type of transient experiments, provided that initial state is well defined.

CHAPTER 6

Comparison experiment simulation

Previous chapter was dealing with a classical analysis of experimental data obtained on triarylamine based dendrimer. Here, classical means that the approach taken for results analysis was based on the Many-Rakavy theory([9], sec. 1.7). Firstly, using formula (1.7.19), from peak position of the transient current responses mobility was extracted. Then, this mobility value was used to estimate contact efficiency based on comparison between expected and obtained steady state current magnitude(sec. 5.2). Lastly, by looking at time resolved current decay, and results of repeated measurements, it was possible to estimate trapping kinematics timescales([36, 37, 10], sec. 5.3). This is already a large amount of information obtained in one measurement.

Unfortunately, this classical way of interpreting results is not completely satisfactory, for reasons given below.

The Many-Rakavy theory, on which the analysis is based, is simplified. The prefactor in the Many-Rakavy formula (1.7.19) was calculated analytically neglecting diffusion. The assumption of ignoring diffusion is connected with another unphysical assumption which considers the sample completely devoid of charge carriers at the beginning of the measurement. Moreover, ohmic contact is assumed. In the simulation results (figs. 1.7.2, 1.7.3), it is shown that the position in time of the peak depends also on the contact barrier. In addition to this, trapping is accounted for only partially, with no release mechanism taken into account ($r_r \equiv 0$). Finally, mobility is assumed to be constant.

These simplifications raise the question: with which uncertainty is obtained the mobility estimation? Recently, it was pointed out that space-charge-limited current transient measurement[2] is less accurate than it might be expected from the formula (1.7.19), because the formula itself does not describe the experiment well. Furthermore, in the same reference, failure to estimate mobility uncertainty is reported. It must be commented that the degree of experimental inaccuracy we may expect certainly is not significant if the measurements are intended to give a coarse estimation of mobility. However, for more precise measurements intended to compare similarly performing materials, a better model of the mobility estimation based of space-charge-limited current transient is certainly necessary. In an even earlier work[35], an analysis of transient responses beyond the Many-Rakavy theory was attempted. Field dependent mobilities and diffusion were taken into account. The material under consideration seemed to behave as trapless, the long current decay was unobservable.

Semi-analytical predictions for both peak current magnitude and peak position in time were verified. Unfortunately, it was concluded that there is some significant disagreement between the theory and experimental results. This raises some questions concerning the interpretation of transient experiments.

The contact efficiency obtained in the previous chapter is a figure of merit, and not a well defined physical quantity. Unfortunately, so defined contact efficiency is not a parameter in any physically based contact model(sec. 1.4, 2.4). Therefore, knowledge of its value gives only limited possibilities to predict the performance of the contact in different device configurations (i.e. different thickness). Since obtention of real ohmic contact seems unlikely[16, 17], and quasi-ohmic contacts seem in practice to be the rule, a possibility of obtaining physically correct contact characterization is highly desirable. One approach for reaching this aim can be to combine the transient estimation of mobility with the stationary characterization, similarly to what was suggested in ref. [17]. Unfortunately, this approach ignores trapping effects.

The currents observed may be heavily influenced by charge carrier trapping. Trap distribution may be complex, greatly complicating the analysis, even if trap distribution is not of interest. As all states are localized, any density of states can be divided between conduction states and trap states. The drift-diffusion transport model augmented with a physical model of contact, by definition, does not explain long time decay of the transient responses. Therefore, in order to explain experimental responses with long decay it is mandatory to take into account the trap kinematics.

As soon as direct simulation of space-charge-limited transient responses became feasible[35, 18, 12], it was evident that a better understanding of experimental results can be obtained by comparing with simulation[35, 12]. In particular, that would permit extraction of parameters which are not measurable directly. The use of simulation therefore allows both to overcome the limitations of the Many-Rakavy theory, and to obtain a self-consistent mobility and contact efficiency characterization.

Simulation assisted approach has been very successful in organic material research. The Gaussian disorder model[42] was established by comparing time-of-flight experimental results with Monte-Carlo simulation. Recently, fitting of stationary current-voltage measurements to simulations has become popular[15]. However, limitations of the steady-state approach have been demonstrated, with regard to distinguishing space-charge-limited current and injection-limited current[17]. These limitations does not exist in the case of transient measurements. Also recently, successful fitting of simulations to CELIV experiments was published[67].

For transient fitting, a failed attempt to get even a qualitative agreement was reported in[2], fig. 6.0.1. It was concluded that the theoretical explanation based on Many-Rakavy

theory and basic drift-diffusion model is insufficient to reproduce the experimental curves. This was somewhat an inspiration for the work we present here.

Indeed, despite these negative results , we devoted some efforts in this work for fitting transient space-charge-limited current responses . The attempt was justified for several reasons. Firstly, physically plausible models of transport, including the extended Gaussian disorder model have been developed[22, 23]. This new model of bulk transport and charge injection not only is strongly justified by master equation simulation[19], but also computationally efficient. It was not used in any of the previous works. Also, the progress in simulation software and computer hardware performances makes this kind of data analysis increasingly more feasible. It is now possible to devote to treatment of experimental data computing power unavailable a few years ago.

However, it stays that transient measurements are still more difficult to be fitted than the stationary ones. Even from purely computational point of view, there is a fundamental difference between steady-state and transient fitting. In the case of stationary simulation, experimental points for different conditions can be calculated independently in parallel. In the case of transient simulation, evolution at a given time can be calculated only when the preceding state is known. Therefore, the transient simulation with self-consistent transport and electric field is essentially sequential for one current response. It also requires that the initial conditions are well defined, both experimentally during measurement and theoretically during simulation. The initial condition problem does not exist in the stationary case. Also, in the stationary case trap kinematics does not need to be taken into account directly. Steady state trapped charge concentration in thermal quasi-equilibrium can be expressed using Fermi-Dirac distribution as a function of the total charge concentration. In transient simulation, trapping kinematics for each trap level must be taken into account directly. For this reason, in the work presented here, only one well defined energetic trap depth was taken into account.

As experimental data, we selected transient responses obtained on a single triarylamine based dendrimer sample. As all the transient responses obtained in the batch of tested samples were similar, the choice of dataset was arbitrary. It is however important to mention that the chosen set was for a very fresh sample. In comparison to our other measurements, these were done most carefully with respect to the requirement of a well rested sample. Averaging was not used during experiment.

The content of this chapter has been published in ref. [68].

6.1. Initial conditions problem

Before going into details of the fitting method, it is interesting to consider what can be the reason for failure in obtaining simulation-experiment agreement as reported in ref. [2] (fig. 6.0.1). The reference is focused on the effects of measurement timing on the measurement
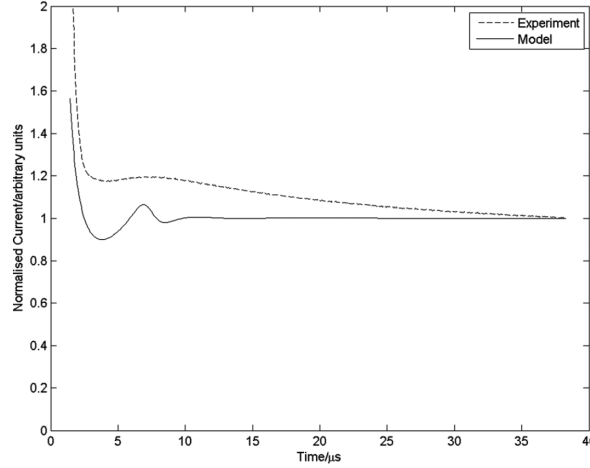
FIGURE 6.0.1. Results of fitting simulation to experimental curve, presented in ref. [2].

results. Following the theoretical and experimental arguments presented in the previous chapter(sec. 5.3), the measurement repetition frequency may affect the position in time of the space-chage-limited current transient peak. The peak position in time is altered if the sample does not equilibrate between the measurements. In such a case, each subsequent measurement is different as the sample is approaching a dynamic equilibrium state.

Very importantly, in the reference cited, averaging of subsequent measurement signals was used in order to improve signal-to-noise ratio. Therefore, only averaged evolution of the transient responses was recorded. This is a major problem for comparing with simulation. The only conceptually straightforward way to compare with dynamic averaged signal is to run the simulation for the same measurement process and average its results. This will naturally be very time consuming. Also, it may be expected that simulation errors, especially these caused by non adequacy of physical model, will accumulate and make the comparison even more difficult. Therefore, because of use of signal averaging, the data presented in ref. [2] is difficult to analyze.

Also, the sample state at the beginning of the measurement must be well defined. Physically, it means that only well equilibrated sample is being measured. In the simulation, proper initial conditions must be calculated. Such conditions can be obtained by solving the drift-diffusion equation in equilibrium to get sample state just before the measurement. Only if simulation is done in such a way, physical evolution of current on application of voltage step is explained.

It must be noticed that not all metal-organic contact models can be used to estimate the equilibrium conditions. The models defining boundary conditions for current, such as the one presented in sec. 1.4, are not suitable for calculating the equilibrium conditions. This is because, at zero applied voltage, they must predict zero current. This implies the
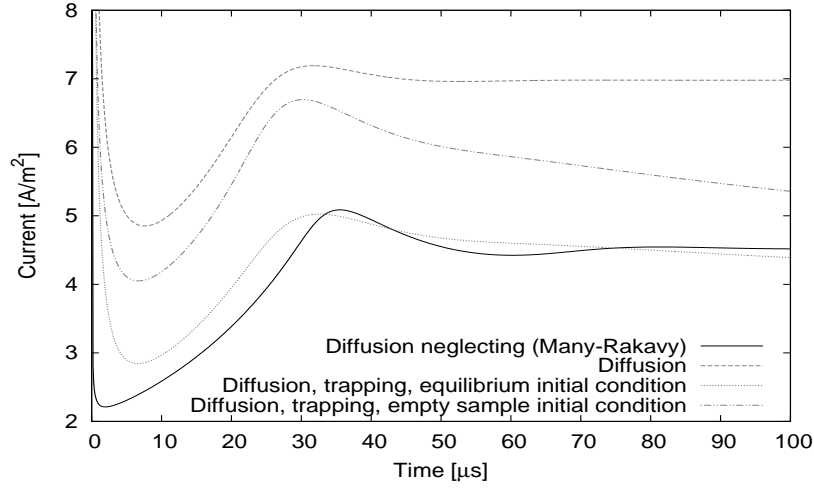
FIGURE 6.1.1. *Simulated dark injection current responses according to different models in which common simulation parameters are sample length $L = 300nm$, mobility $\mu = 10^{-5}cm^2/(Vs)$, applied voltage $2V$ and relative dielectric permittivity $\epsilon_r = 3$. . The full line corresponds to the response predicted by the analytical solution. Other lines are obtained by taking into account additional parameters as quoted in the inserted legend.*

organic layer completely devoid of charge carriers at the beginning of the measurement. The equilibrium conditions can be estimated very well using the theory outlined in sec. 2.4, based on the assumption of local thermal equilibrium at the interface. It is possible that the failure reported in ref. [2] was because the simulation method uses[50] different contact model, which may particularly fail in the case of equilibrium state calculation. Also, certainly trapping is not taken into account in the simulation as their theoretical curve is flat immediately after the current peak. This is in sharp contrast with the experimental result.

The importance of initial condition can be seen in fig. 6.1.1. There, transient responses are calculated for the same value of mobility, but for different configurations of trapping and choices of initial conditions. It can be seen that while the peak position in time is unaffected, the whole shape of the transient response depends critically on the initial conditions. In particular, the peak current magnitude is strongly affected. Addition of diffusion increases the current in comparison to Many-Rakavy theory, in absence of traps. When traps are present, some of them are pre-filled in the equilibrium. When this is taken it into account, a lower position of the current peak is predicted followed by a less profound decay. In other words, a simulation assuming an unphysical empty initial sample will converge to the same steady state current, but will predict wrongly the initial part of current response. For simulation of response curves shown in fig. 6.1.1, the traps are here characterized by the concentration $N_t = 6.2 \times 10^{15} cm^{-3}$, the trapping coefficient $r_t = 6.4 \times 10^{-13} cm^3 s^{-1}$ and

the release frequency $f_r = 400s^{-1}$. Common simulation parameters are the sample length $L = 300$nm, the mobility $\mu = 10^{-5} cm^2/(Vs)$, the applied voltage $2V$, the relative dielectric permittivity $\epsilon_r = 3$ and charge carrier density at contact plane $n_c = N_0/2 = 1.22 \times 10^{20} cm^{-3}$.

6.2. Fitting method

It is somehow natural that from comparison of simulation and experiment data value of parameters not measurable directly can be obtained. However, this kind of curve fitting deserves several words of comments explaining the basis of this approach. This is particularly important because the behavior of simulation is usually much less well understood that the behavior of an analytical theory.

When fitting to simulation, care to be taken to ensure that the parameters for which simulation is evaluated are in its range of applicability. Because the range of parameters attempted will be larger than the reasonable range, care must be taken to properly recognize the situations where the simulation failed to provide physically valid results. It may be possible that the same results are similarly reproduced with different parameter values, corresponding to different interpretations of the experiments. In order to give unique interpretation of the data, uniqueness of the final parameter set has to be checked. Furthermore, parameter error estimation based on simple assumptions may be not accurate and it requires special attention.

The problem considered here is to find a vector parameters $\mathcal{P} = [\mu, ...]$ corresponding to the unknown physical properties of the sample measured. Among them, there is charge carrier mobility μ, introduced in section 1.1 or charge carrier mobility prefactor μ_0, introduced in section 2.2. The optional components are the contact barrier Δ, introduced in section 2.4, and the trap rate r_t, release rate r_r and trap concentration N_t, all introduced in section 1.5.

Experiment is given by vector y, corresponding to the experimental results. The dataset y is built by concatenating discretized transient curves $i_0, i_1, ..., i_n, i_k$. The discretized transient responses are vectors of real numbers, the vector i_k denotes the kth experimental transient response, obtained for voltage V_k. Its components i_{kj} are current density value measured for voltage V_k at time t_j.

Since it is not useful to keep all measurement points in y, we selected a number of the same logarithmically equispaced point for each curve. Using simulation, theoretical vector corresponding to y can be calculated using parameters $\mathcal{P}$ and physical known parameters. These were in all cases the temperature $T = 300K$, sample thickness $L = 300$nm and relative dielectric permittivity $\epsilon_R=3$. In the cases involving the extended Gaussian disorder model, $a = 1.6$nm was used. It must be commented, that even in the case of constant mobility model, some disorder value must have been assumed to calculate the contact properties. This is denoted as σ_c and given along with Δ.

At this stage, no assumption about the number of estimable parameters and about their accuracy is made, a statistical approach must be sought. Recently, the Bayes theorem was recognized as one fundamental conceptual base for computer assisted data analysis. In the case considered here, the Bayes theorem states that probability $P(\mathcal{P}|y)$ of given parameter vector $\mathcal{P}$ given a measurement result y is

$$(6.2.1) \qquad P(\mathcal{P}|y) = \frac{P(y|\mathcal{P})P(\mathcal{P})}{P(y)}$$

where $P(\cdot)$ denotes probability, and $P(A|B)$ denotes conditional probability of A given B. In such a formulation, the task of parameter extraction is to finding the most likely parameters $\mathcal{P}$, by maximizing $P(\mathcal{P}|y)$. If a single region of parameter space can be found where $P(\mathcal{P}|y)$ achieves a maximum value, then this region can be presented as a measurement interpretation.

We start by noting, that the likelihood of obtaining given experimental data $P(y)$ is constant and therefore does not affect the optimization. Also, $P(\mathcal{P})$ represents the probability of given parameters. While this term is extremely useful in general case, at this moment it is hard to give to this term any concrete shape. In this term, the probability of mobility value can be introduced, taking into account the Many-Rakavy analysis. However, in the work presented here no prior assumptions are introduced explicitly at this point. Therefore, the following proportion relationship can be written:

$$(6.2.2) \qquad P(\mathcal{P}|y) \propto P(y|\mathcal{P})$$

. The above equation is in fact deeper than it may look, because it gives a proportion relating a function very hard to be calculated on its left side and one very simple on its right side. Indeed, the left side, which is to be maximized, is the probability of parameter vector $\mathcal{P}$ given the measurement y. This cannot be directly computed except for trivial or analytical cases. The right side is the probability of measurement y given parameter vector $\mathcal{P}$. With help of simulation taking the parameter vector, it is straightforward to compute it assuming only a model of experimental noise. The experimental error is most naturally assumed to be Gaussian with zero mean and one variance σ_n. Using this assumption,

$$(6.2.3) \qquad P(y|\mathcal{P}) = G(y - x(\mathcal{P}))$$

while $x(\mathcal{P})$ denotes simulated experimental result, calculated by using the parameter vector $\mathcal{P}$ and G denotes a Gaussian distribution with zero mean and variance σ_n. Therefore,

(6.2.4)
$$P(\mathcal{P}|y) \propto \prod_{ij} \frac{1}{\sqrt{2\pi}\sigma_n} \exp \frac{-\left(y_{ij} - x(\mathcal{P})_{ij}\right)^2}{2\sigma_n^2}$$

Objective function f to be minimized is obtained as the logarithm of $P(\mathcal{P}|y)$.

(6.2.5)
$$f(\mathcal{P}) = \sum_{ij} \left(y_{ij} - x(\mathcal{P})_{ij}\right)^2$$

As the function above is only minimized, the constant components arising from the proportionality and the logarithms of $1/\sqrt{2\pi}\sigma_n$ can be dropped. For the same reason, the multiplicative component $1/(2\sigma_n^2)$ was also dropped. In fact we recover here the least-squares fitting criterion. However, it was illustrated that one point to improve the procedure presented here is by introducing the $P(\mathcal{P}) \neq 1$. This is beyond the usual least-squares approach.

The equation 6.2.5 provides the mathematical definition of the function to be minimized. However, in the case of optimization problem considered here there are some difficulties to be kept in mind.

All the efficient methods for solving optimization problems use objective function derivative. Because simulation is used, the above objective function does not have an analytically defined derivative. Derivative can be estimated using finite-difference formula, but this costs additional computation time. Furthermore, when using finite difference formula, the step used for derivative calculation must be adapted to the evolution of the simulation result. Proper calculation of derivatives is thus not straightforward. However, it is possible that implementation of derivative estimation could lead to significant improvements in the fitting speed.

In a case of optimization with simulation, the objective function is noisy. For sufficiently small changes of parameters, the simulation result will differ only by noise because of finite numerical accuracy. In the case presented here, the problem is even more significant because of the adaptive timestepping(section 3.4). The simulation timesteps cannot in general correspond to the time spacing between experimental points. Also, it seems to be undesirable to manually specify fixed timestepping of the simulation. This could cause simulation failure or unphysical results for some combinations of parameters. Therefore, the simulation is permitted to use its standard adaptive timestepping and the simulated curve is then interpolated to the experimental data, This introduces additional simulation noise, because simulated points can be distributed arbitrarily with respect to experimental points. Although the decision to use automatic timestepping and interpolate simplified the program while guaranteeing reliability, it might be far from being optimal because of its effect on the optimization process.

In order the reliability and correctness of the simulation to be ensured, it must be avoided that the simulation is being evaluated from physical meaningless parameters. Negative value

of mobility should be avoided, as it they have the same effect as changing charge carrier sign or reversing voltage bias polarity. The possibility of obtaining the same result with μ and $-\mu$ introduces unnecessary ambiguity. As for contact barrier, negative values are physically possible but they may lead to optimization plateau. Barrier values too high or too low ($|\Delta| \gg 1\text{eV}$) cause numerical problems in the simulation. The trapping parameters must not be negative (N_t, t_r, r_r). Zero values of μ or r_r will make the simulation fail unconditionally because singular matrix will be encountered.

The above constraints on parameters must be imposed somehow. The simplest way is to "clip" them appropriately when evaluating the simulation. If one given parameter is too close to zero or negative, it can be replaced by a minimum value.

Unfortunately, this simple method is not satisfying because it creates a plateau in the objective function. Then, it becomes impossible to optimize parameters in the region where the objective function is independent of some of them. In order to avoid such a plateau, penalty to objective function may be added for invalid parameter values. This corresponds exactly to adding the term $P(\mathcal{P})$ in the derivation of objective function. Another possibility is to use a constrained optimization method. Because of simple form of the necessary constraints, unconstrained optimization was used working a one mapped parameter vector $\mathcal{P}'$. Internally (from point of view of optimizer), the considered parameter vector is defined as $\mathcal{P}' = log\ \mathcal{P}$, where log is taken element-wise (ie. $\mu' = \log \mu$). f' is the modified objective function

$$(6.2.6) \qquad f'(\mathcal{P}') = \sum_{ij} \left(y_{ij} - x(\exp \mathcal{P}')_{ij} \right)^2$$

By this way, the optimization problem is unconstrained because $\mathcal{P}'$ may take any real values. On the other hand, positivity of all simulation parameters is enforced since $\exp \mathcal{P}' > 0$. Again, it is not sure if this solution is optimal, especially from computational time point of view. Certainly, it makes objective function more nonlinear.

To optimize above noisy multidimensional objective function, we tested different unconstrained optimization algorithms implemented in SciPy. We started with traditional Levenberg-Marquardt algorithm, but no good results were obtained. Better results were obtained using Powell algorithm .

In order to use any computationally efficient local search method, an initial guess of the solution is required. Unfortunately, we found the local search algorithms fail frequently if too large difference exists between experimental and simulated curves at the initial guess. This is because the Many-Rakavy peak, which defines the mobility, is not very prominent. In a case of a large mismatch, it has limited influence on the value of the objective function. Then, the whole optimization is likely to fail because μ appears to affect the transient responses just similarly as the contact barrierΔ, ie. by introducing constant prefactor to current only.

As mentioned before, this behavior could be changed by introducing the prior knowledge of μ in the optimization function. For simplicity, we have chosen a different approach.

The fitting process was performed in two steps. In the first step, μ and Δ was sampled on a regular grid, and only the trapping parameters were optimized using local search methods. The values of μ were chosen to be close to that obtained from the classical analysis, and the possible values of Δ were tried with 0.01eV increments.

This way, approximate optimal solution was found. This optimal solution was then used as a initial guess for local search methods. In order to ensure uniqueness of the solution, the optimization procedure was repeated multiple times, each time starting with a slightly different initial guess. The perturbed initial points were obtained by multiplying each parameter of the approximate solution by a random number close to 1.

The procedure can be justified as follows. In a previous work on space charge limited current transients[10], it was shown that for one given mobility, trap concentration N_t and trap energetic depth, one corresponding r_r/r_t can be estimated from the shape of current-voltage characteristics only. Furthermore, in ref. [36] and [37] it has been demonstrated that the decay time constant of transient responses gives the trapping time r_t. Therefore, it may be expected that fitting all the three trapping parameters (N_t, r_r, r_t) is well defined and unique solution exists. Therefore, local search method can be used safely regardless of initial guess. It might not be true when mobility μ and contact barrier Δ are also optimized.

By looking at uniqueness of optimal solution in both stages of the optimization procedure, global uniqueness of the solution is ensured.

The simulated responses $x(\mathcal{P})$ presented here were calculated by the simulator described in chapter 3. The fitting program was also implemented in Python using Scipy.

6.3. Results

The first question to be asked, when fitting simulation to the experiment, is whether disorder affects the measurement results. The simplest way of estimating maximum disorder compatible with experimental observation is by comparing the experimental and fitted time positions of the peaks for different disorder values. This comparison is presented on fig. 6.3.1. The plot shows that the experimental time positions are well compatible with the Many-Rakavy formula (1.7.19), and therefore the constant mobility. On the other hand, the experimental results appear also to be compatible with disorder values up to $\sigma \leq 100$mV. The fit to Many-Rakavy formula gives mobility $8.25 \times 10^{-6} cm^2/(Vs)$.
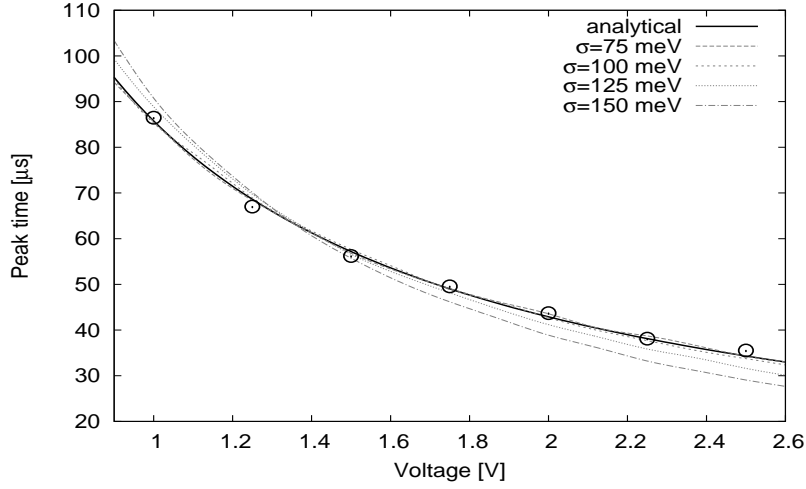
FIGURE 6.3.1. *Experimental peak times as a function of applied voltage. Lines correspond to different fits obtained with analytical model (full line) and models including different degrees of disorder (σ) (inset legend). The experimental positions are consistent both with analytical model and with extended Gaussian disorder for σ not exceeding approximately $100meV$. Fit to analytical formula (1.7.19) gives mobility $8.25 \times 10^{-6} cm^2/(Vs)$ (solid curve). Fits to extended Gaussian disorder model with inter-site distance $a = 1.6nm$ and different disorder values $\sigma = 75, 100, 125, 150 meV$ give mobility prefactors $\mu_0 = 6.32 \times 10^{-6}$, 4.53×10^{-6}, 1.99×10^{-6}, $4.25 \times 10^{-7} cm^2/(Vs)$ respectively. Sample length $L = 300nm$.*

We start with the analysis neglecting disorder, where constant mobility value is assumed. Comparison of experimental current densities calculated predicted for previously obtained value of mobility previously with experimental currents revealed that the latter are significantly lower. Therefore, in order to construct physical model of the sample, a current lowering mechanism must be included. Two current lowering mechanisms considered in this work are by contact barrier or by introduction of traps. The best fits in both cases are shown in fig. 6.3.2. It may be seen that both are inconsistent with the experimental observation.

The best fit to the model of injection limited conduction($\mathcal{P} = [\mu, \Delta]$, ref. [17]), neglecting traps, are shown in fig. 6.3.2a. The model fails to account for the long time decay of the current responses. This proves that the current observed is not purely injection limited. Nevertheless, the fit does yield the maximum barrier value. As no mechanism is expected to exist that would increase the current, the estimation of maximum barrier height is obtained. This is seen on the curve for voltage $2.5V$, where the simulated response is systematically lower or equal to the experimentally observed.

The best fit to the model of trap limited space-charge-limited conduction($\mathcal{P} = [\mu, r_t, r_r, N_t]$, ref. [10]), neglecting contact barrier, is given in fig. 6.3.2b. The model can introduce the

long time decay, but good agreement with experimental data was obtained only in the case of highest voltage (2.5V). With decrease of voltage, the agreement becomes bad. This is well explained by that arbitrary trap distribution introduces very high slope of the current voltage curve(see sec. 1.5) over extended range of fields. This is incompatible with our observation. The trap distribution compatible with experiment for the highest voltage is in evident disagreement with the other responses.
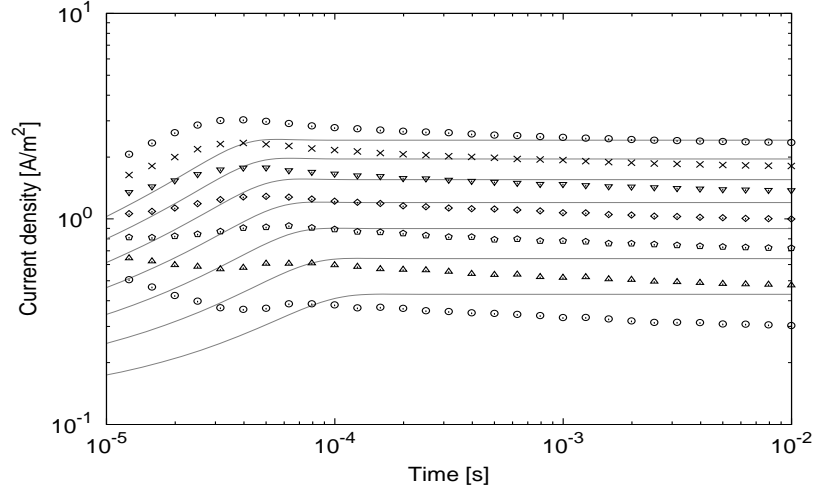

a)
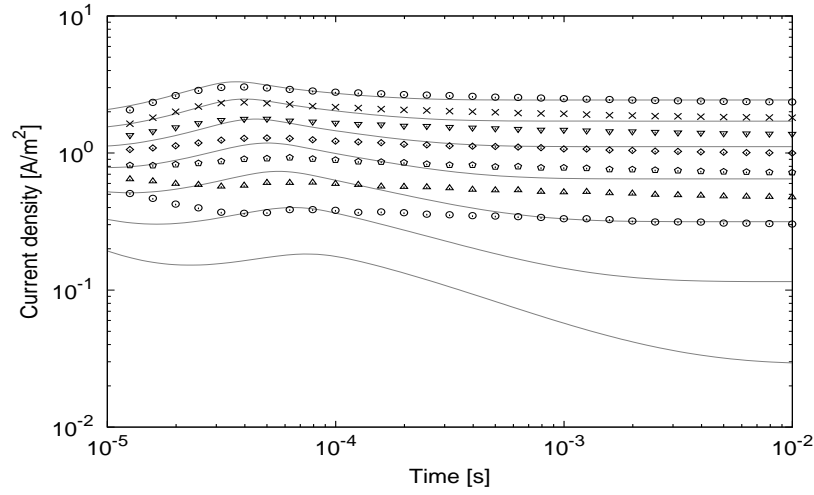
b)

FIGURE 6.3.2. *Experimental transient responses(points) fitted to basic theoretical models(curves): a) constant mobility and injection barrier[17]; b) constant mobility with trapping[10]. Common simulation parameters: $\mu = 8.25 \times 10^{-6} cm^2/(Vs)$, $\epsilon_r = 3$ a) injection barrier $\Delta = 0.456eV(\sigma_c=75meV)$; b) trap concentration $N_t = 8.14 \times 10^{15}$ cm^{-3}, trapping coefficient $r_t = 6.856 \times 10^{-12}$ $cm^3 s^{-1}$, release frequency $f_r = 12.52$.*

The failure to reproduce experimental responses justifies attempt to fit all the parameters ($\mathcal{P} = [\mu, \Delta, r_t, r_r, N_t]$) of a model taking into account both trapping effects and contact barriers. The results are presented in fig. 6.3.3. As seen on the figures, this permits reasonable agreement between simulation and experimental data. Therefore, in the case considered, both trapping and contact have important effects on transient responses, and their parameters can in principle be extracted from experimental data without overfitting.

Closer look at the results presented in fig. 6.3.3 reveals, that in fact higher mobility tend to reproduce better the transient responses obtained for higher voltages. On the other hand, to reproduce the responses obtained for lower voltages smaller mobility is preferred. This illustrated by the plot 6.3.3c, where for each voltage mobility range of the best fitting solutions are shown. This is an interesting observation, as proves that constant mobility model is inconsistent with the observation, even though the peak positions are consistent with the Many-Rakavy theory (fig. 6.3.1). Therefore, it seems obligatory to take disorder effects into account.
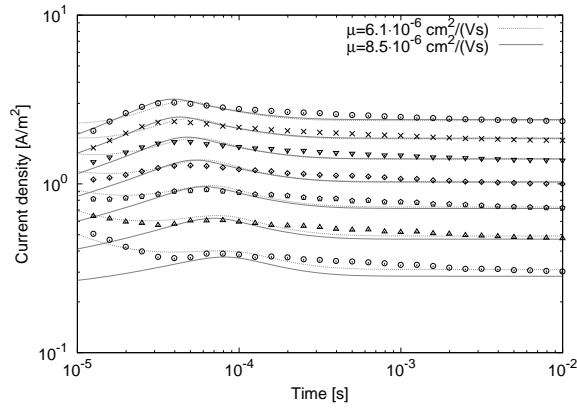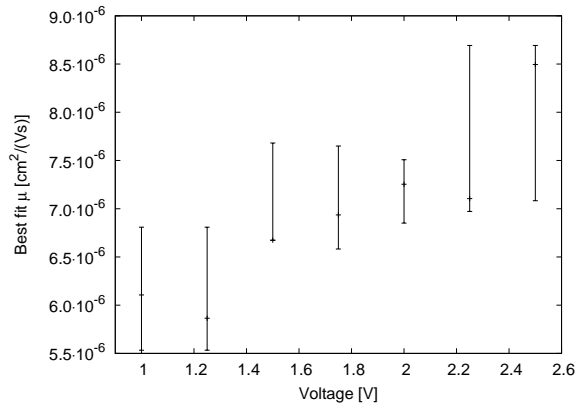
a)
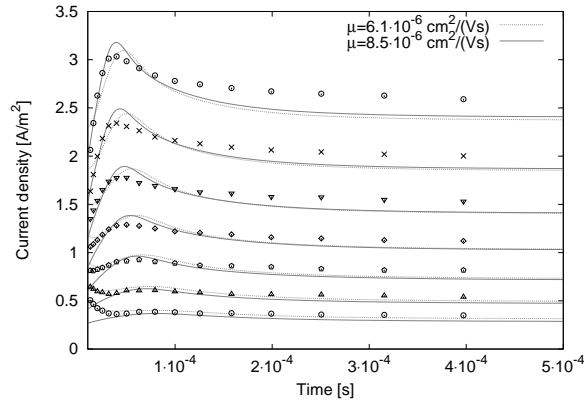
b)

c)

FIGURE 6.3.3. *Experimental transient responses (points) fitted to a model assuming constant mobility and taking into account both interfacial barrier and bulk trapping effects. . The same result is presented in logarithmic (a) and linear (b) scale for clarity. In (a), (b), two similarly good fits are shown. Simulation parameters are $\mu = 6.106 cm^2/(Vs)$: $\Delta = 0.283eV$ $(\sigma_c = 75meV)$, $N_t = 7.37 \times 10^{15} cm^{-3}$, $r_t = 3.39 \times 10^{-12} cm^3 s^{-1}$, $f_r = 2820s^{-1}$; $\mu = 8.495 cm^2/(Vs)$: $\Delta = 0.409eV$, $N_t = 5.09 \times 10^{15} cm^{-3}$, $r_t = 3.84 \times 10^{-12} cm^3 s^{-1}$, $f_r = 3067s^{-1}$. c) Best fitting mobility range in function of voltage.*

6.3. RESULTS

We verified the importance of disorder by fitting $\mathcal{P}=[\mu_0, \Delta, r_t, r_r, N_t]$, by testing disorder values $\sigma = 75\text{meV}$ and 100meV. In the case of $\sigma = 75\text{meV}$, similar results were obtained as in the case of previously considered constant mobility model. For disorder $\sigma = 100\text{meV}$, much better agreement with experimental data was found, as presented in fig. 6.3.4. Plot 6.3.4c shows curious shape of the minimum plateau of fitting function, in $\mu_0 - \Delta$ space, where dots denote numerical results of the optimization procedure. The spread of mobility prefactor is greatly reduced, as seen in tab. 1.
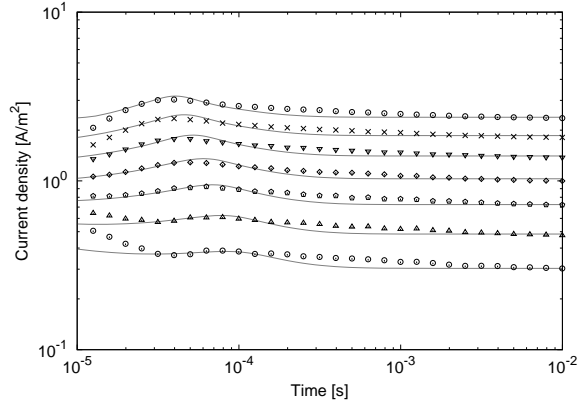
a)
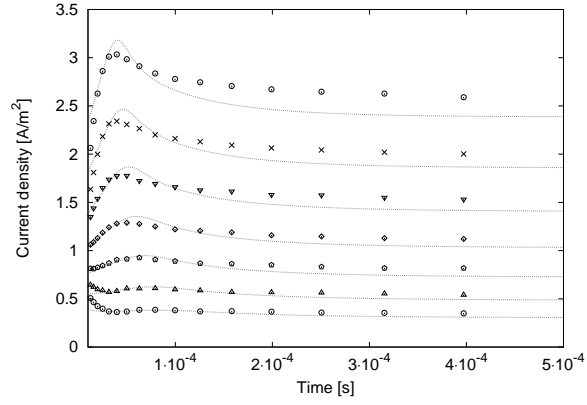
b)
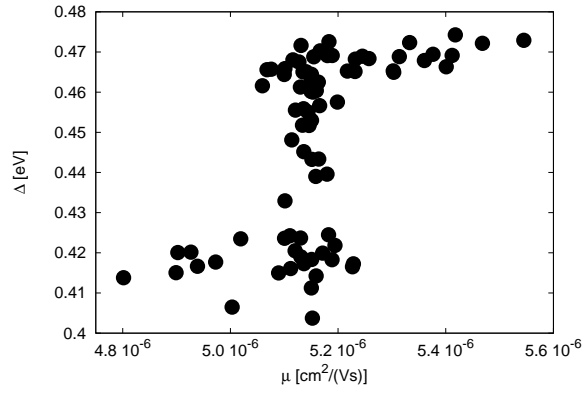
c)

FIGURE 6.3.4. *Results obtained after including the influence of effects of disorder $\sigma = 100meV$ on diffusion and mobility using extended Gaussian disorder model. a,b) Experimental (points) and simulated (curves) transient responses, in logarithmic and linear scales respectively. Simulation parameters: $\sigma = 100meV$, $\mu_0 = 5.02 \times 10^{-6} cm^2/(Vs)$, $\Delta = 0.42eV$, $N_t = 6.56 \times 10^{15} cm^{-3}$, $r_t = 3.39 \times 10^{-12} cm^3 s^{-1}$, $f_r = 2998 s^{-1}$. c) Distribution of best fit's mobility and barrier height values.*

Model	$\mu = const$	$\sigma = 100$meV
$\mu[cm^2/(Vs)]$	$(7.1\pm1.6)\times10^{-6}$	-
$\mu_0[cm^2/(Vs)]$	-	$(5.1\pm0.4)\times10^{-6}$
$\Delta[eV],\sigma_c{=}50$meV	0.31 ± 0.09	-
$\Delta[eV],\sigma_c{=}75$meV	0.37 ± 0.09	-
$\Delta[eV],\sigma_c{=}100$meV	0.44 ± 0.09	0.44 ± 0.04
$N_t[cm^{-3}]$	$(6.4\pm1.5)\times10^{15}$	$(6.9\pm1)\times10^{15}$
$r_t[cm^3s^{-1}]$	$(3.8\pm1.4)\times10^{-12}$	$(2.9\pm1.0)\times10^{-12}$
$f_r[s^{-1}]$	$(3.5\pm1.4)\times10^3$	$(4.3\pm1.3)\times10^3$
$E_t[eV]$	(0.32 ± 0.02)	(0.31 ± 0.02)
$\sigma_t[cm^2]$	$\approx 3\times10^{-12}$	$\approx 3\times10^{-12}$

TABLE 1. *Extracted model parameter values with uncertainties, for the two models considered. μ denotes charge carrier mobility (in the case of constant mobility model), μ_0 and σ denote mobility prefactor and bulk disorder (in the case of extended Gaussian disorder model), Δ denotes potential barrier, σ_c denotes Gaussian disorder of state energies at metal-organic interface, N_t denotes trap concentration, r_t is trapping coefficient, f_r is release frequency, E_t is calculated trap depth and σ_t is estimated trapping cross section. Inter-site distance is assumed to be $a = 1.6nm$ (corresponding $N{=}2.44\times10^{20}/cm^3$), sample length $L = 300nm$, relative dielectric constant $\epsilon_r{=}3$ and temperature $T = 300K$.*

6.4. Conclusions

In this chapter, several contributions were presented. Firstly, it was demonstrated that state of the art models for transport in organic materials can reproduce the experimental space-charge-limited current responses. Agreement much better than previously reported[2] was obtained. It was shown that, in order to obtain the agreement, all relevant effects must be taken into account. In our case these were the bulk transport, trapping and contact barrier. Any models missing any of these effects were in clear disagreement with the experimental data. Therefore, from the experimental dataset, the parameters regarding mobility, contact and trapping could be extracted, as shown in table 1. This shows that the space-charge-limited current transient measurements are useful not only for mobility measurements, but also for consistent characterization of metal-organic interface and trapping effects.

The analysis can be only successfully done if initial state of sample at the beginning of measurement and at the beginning of simulation are well defined. Care must be taken to ensure that sample is in equilibrium conditions at the beginning of the measurement.

It was shown, how fitting process can be done to ensure solution uniqueness. It must be commented that the procedure outlined here is rather slow and one fitting of all parameters to a set of curves took several days on Intel Core i7 2600K. This is partially because the software used was written in Python, and partially because the procedure is inefficient. Various possibilities of enhancements were suggested. Greatest amount of time is spent to ensure

uniqueness of the solution. If it can be assumed, or checked in smarter way, calculation time could be significantly reduced.

At the end, it is interesting to considered the reasons of disagreement still existing in fig. 6.3.4. Most clearly, the long time decay of the curves is not reproduced very well. This may be caused by only taking one trap level into account at a fixed energetic position. This is in particular inconsistent with the Gaussian disorder model. Even if such a level existed at well defined energetic position, its relative energetic depth with respect to transport states would be a Gaussian distribution. Deficiencies in taking trapping effects into account grow in importance for lower voltages. In fact, the agreement obtained for lowest voltage is much worse than that for the highest. Note that this may also be caused by the statement of the objective function. This deficiency can be corrected by adding more trap levels to the simulation, which is straightforward.

For simulations taking disorder into account, extended Gaussian disorder model was used. It has already been used for transient simulation[69], but developed only for stationary simulation[22, 23]. However it seems that at the moment there is no other practical way for incorporating disorder in transient space-charge-limited current simulation fast enough for fitting to experimental data.

Conclusions and outlook

This thesis work mainly concerns: the development and the verification of a simulator based on the current theories of transport in thin organic films(chapter 3); the development and the verification of a new experimental setup for space-charge-limited current transients(chapter 4); the transient characterization of a new organic semiconductor(chapter 5) and the comparison of experimental results with simulations(chapter 6). With this work we try to answer the following questions: (i) can measurement of space-charge-limited current transients be simplified and made more applicable by updating experimental setup? (ii) can current theories for transport in thin organic films reproduce the transient experiments? and (iii) can new knowledge be obtained by numerical analysis of transient measurement results? We show that all these questions can find positive answers, as explained in respective chapters and in the published work. This gives the following perspectives:

(1) Transimpedance based measurements of space-charge-limited transients allow to use lower current ranges than previously. This permits characterization of samples with smaller area and/or significantly influenced with contact barrier. At the same time, none per sample adjustment is necessary. Therefore, the technique can be more simply applied to the quasi-ohmic contact cases, to the extent limited by trapping effects in the sample rather than by the current sensitivity of the measurement setup. Extended uses for investigation of repeatability and aging effects are also possible.

(2) The contact barrier is among the parameters extracted from space-charge-limited current transient measurement. Despite that it is the fundamental physical property of an idealized metal-organic charge injecting contact, practical contact performance may be heavily influenced by other factors. These include the effects of the local structure of the sample as well as the adhesion of organic material to metal. In fact, the disorder and the density of states at metal-organic interface determines the electrical properties of the contact[70]. This is reflected by the simulation models (sec. 2.4), where the injected current is predicted to depend directly on the density of charge carrier at interface and only indirectly on the barrier height. Therefore, although we put contact barrier among fitted parameters, the density of charge carriers at interface may be a better quantity extractable from electrical characterization.

(3) Deduction of the existence of a contact barrier between gold and dendrimer is qualitatively correct, proven by the contact forming observation. However, it is very

interesting to investigate to which degree this estimation is good. This is challenging, because it is not straightforward to do independent measurement of the contact barrier . The transition from a perfectly ohmic to a non-ohmic contact takes place in a relatively small range of contact barrier values ($\approx 0.2 eV$, see figs. 1.6.1, 1.7.2, 1.7.3). In order to experimentally confirm the barrier estimation, out of reach accuracy of physical barrier height realization may be required. Possibly, the contact characterization resulting from transient measurements can be investigated more easily by experimentally adjusting the density of trap states at the metal-organic interface[71] rather than by varying the electrode work function.

(4) It would be interesting to investigate how the results of characterization involving simulation are affected by single trap level assumption of and if the technique can be extended to more detailed trapping characterization. Another question is if agreement with simulation can be obtained at different temperatures.

(5) By taking the disorder into account by using the Extended Gaussian Disorder Model[22], improvement in agreement between simulation and experiment was obtained. It would be interesting to investigate to which degree transient space-charge-limited current measurements can be useful for disorder estimation. The limitations may result from the limited temperature and electric field ranges in comparison with that of time-of-flight. The estimated disorder value can be verified by comparing with measurements performed in another device configurations (i.e. OFET).

(6) There is a fundamental question concerning the correctness of using the External Gaussian Disorder Model for transient simulation. In this work, that does not have an essential importance because the comparison with transient responses calculated using EGDM only show the deficiency of disorder neglecting model. Surely, a proper theoretical approach for transient space-charge-limited simulation would be very useful for interpretation of space-charge-limited current transients in organic films. For the moment, only limited attention is given to transient modelling of transport [72].

(7) It is worth to remark that the whole work presented here was concerned with unipolar transport in thin film diodes. However, the double injection transients also contain useful information on transport in thin organic films[73]. Furthermore, unipolar space-charge-limited current transient measurements was reported[74] in an in-plane electrode configuration. While we failed to realize this type of measurement, it is an interesting idea for example for comparing longitudal and transveral transport properties.

(8) Also useful information can be obtained by performing transient measurements in the organic field effect transistor[75] configuration[76, 77, 78]. Also in a similar device

101

configuration, displacement current measurements on long channel capacitors can be studied[79, 80]. These transient measurements also give the values of mobility and injection efficiency. Possibly many elements of approach presented here are applicable to more general classes of devices.

In conclusion, we hope that the contributions presented in the thesis will make more popular the study of transport in organic materials by performing measurements of transient space-charge-limited currents.

List of contributions

Related papers:

- Marek Z. Szymański, Irena Kulszewicz-Bajer, Jérôme Faure-Vincent, and David Djurado, Comparison of simulations to experiment for a detailed analysis of space-charge-limited transient current measurements in organic semiconductors, Phys. Rev. B 85, 195205 (2012)
- Marek Z. Szymański, Irena Kulszewicz-Bajer, Jérôme Faure-Vincent, David Djurado, Transport properties of triarylamine based dendrimers studied by space charge limited current transients, Optical Materials, Volume 34, Issue 10, August 2012, Pages 1630–1634
- Marek Z. Szymański, Beata Łuszczyńska, Jean Marie-Verilhac, Peter Reiss, David Djurado, Simplified transient space-charge-limited current measurements of mobility using transimpedance amplifier, Organic Electronics, in press, DOI: 10.1016/ j.orgel.2012.11.006
- Marek Z. Szymański, David Djurado, Fast low current level measurements, Informatyka, Automatyka, Pomiary w Gospodarce i Ochronie Środowiska, Volume 3, 2011, Pages 46-49

Deposited patents:

- Marek Z. Szymański, David Djurado, "Dispositif de mesure de courant transitoire dote de moyens de compensation en courant", deposited on 11th of July 2012, with number 12 56666

Additional papers:

- Piotr L. Makowski, Marek Z. Szymański, and Andrzej W. Domański, Lyot depolarizer in terms of the theory of coherence—description for light of any spectrum, Applied Optics, Vol. 51, Issue 5, pp. 626-634 (2012)

Related conference partitipation:

- Marek Z. Szymański, David Djurado, Electrical characterization of organic semiconductors by transient measurements, Matériaux et Nanostructures π-Conjugués (MNPC) 2011, Obernai 03-07 October 2011, France, oral
- Marek Z. Szymański, Transport properties of electroactive triarylamine based dendrimers studied by space charge limited current transients, Workshop on Organic

Electronics and Nanophotonics (WOREN) 2011, September 4-8 Angers, France, poster
- Marek Z. Szymański, David Djurado, Fast low level current measurements, International Interdisciplinary PhD Workshop (IIPhDW) 2011, Zielona Góra, August 28-31, Poland, oral

Bibliography

[1] P. Stallinga, Electrical Characterization of Organic Electronic Materials and Devices, Wiley, 2009.

[2] T. Esward, S. Knox, H. Jones, P. Brewer, C. Murphy, L. Wright, J. Williams, A metrology perspective on the dark injection transient current method for charge mobility determination in organic semiconductors, Journal of Applied Physics 109 (2011) 093707.

[3] J. C. Scott, Metal–organic interface and charge injection in organic electronic devices, Journal of Vacuum Science and Technology A: Vacuum, Surfaces, and Films 21 (2003) 521–531.

[4] Baessler, Heinz and Kohler, Anna, Charge Transport in Organic Semiconductors, in: Metzger, Robert M. (Ed.), Unimolecular and Supramolecular Electronics I, volume 312 of *Topics in Current Chemistry*, Springer Berlin, 2012, pp. 1–65.

[5] D. Scharfetter, H. Gummel, Large-signal analysis of a silicon read diode oscillator, Electron Devices, IEEE Transactions on 16 (1969) 64 – 77.

[6] C. H. Cheung, K. C. Kwok, S. C. Tse, S. K. So, Determination of carrier mobility in phenylamine by time-of-flight, dark-injection, and thin film transistor techniques, Journal of Applied Physics 103 (2008) 093705.

[7] M. Abkowitz, J. S. Facci, J. Rehm, Direct evaluation of contact injection efficiency into small molecule based transport layers: Influence of extrinsic factors, Journal of Applied Physics 83 (1998) 2670–2676.

[8] A. Ioannidis, J. S. Facci, M. A. Abkowitz, Evolution in the charge injection efficiency of evaporated au contacts on a molecularly doped polymer, Journal of Applied Physics 84 (1998) 1439–1444.

[9] A. Many, G. Rakavy, Theory of transient space-charge-limited currents in solids in the presence of trapping, Phys. Rev. 126 (1962) 1980–1988.

[10] M. A. Lampert, P. Mark, Current Injection in Solids, Academic Press Inc, 1970.

[11] M. Abkowitz, J. S. Facci, M. Stolka, Behavior of an ideal injecting contact on a trap-free polymer, Applied Physics Letters 63 (1993) 1892–1894.

[12] J. Scott, S. Ramos, G. Malliaras, Transient space-charge-limited current measurements of mobility in a luminescent polymer, Journal of Imaging Science and Technology 43 (1999) 233–236.

[13] Kazuhiko Seki and Tadaaki Tani and Hisao Ishii, Electronic structures of organic-inorganic interfaces studied by UV photoemission, Thin Solid Films 273 (1999) 20–26.

[14] Dragica Vasileska and Stephen M. Goodnick and Gerhard Klimeck, Computational Electronics: Semiclassical and Quantum Device Modeling and Simulation, CRC Press, 2010.

[15] E. Knapp, R. Hausermann, H. U. Schwarzenbach, B. Ruhstaller, Numerical simulation of charge transport in disordered organic semiconductor devices, Journal of Applied Physics 108 (2010) 054504.

[16] Z. B. Wang, M. G. Helander, M. T. Greiner, J. Qiu, Z. H. Lu, Analysis of charge-injection characteristics at electrode-organic interfaces: Case study of transition-metal oxides, Phys. Rev. B 80 (2009) 235325.

[17] Z. B. Wang, M. G. Helander, M. T. Greiner, J. Qiu, Z. H. Lu, Carrier mobility of organic semiconductors based on current-voltage characteristics, Journal of Applied Physics 107 (2010) 034506.

[18] B. Ruhstaller, S. A. Carter, S. Barth, H. Riel, W. Riess, J. C. Scott, Transient and steady-state behavior of space charges in multilayer organic light-emitting diodes, Journal of Applied Physics 89 (2001) 4575–4586.

[19] J. J. M. van der Holst, M. A. Uijttewaal, B. Ramachandhran, R. Coehoorn, P. A. Bobbert, G. A. de Wijs, R. A. de Groot, Modeling and analysis of the three-dimensional current density in sandwich-type single-carrier devices of disordered organic semiconductors, Phys. Rev. B 79 (2009) 085203.

[20] J. C. Blakesley, H. S. Clubb, N. C. Greenham, Temperature-dependent electron and hole transport in disordered semiconducting polymers: Analysis of energetic disorder, Phys. Rev. B 81 (2010) 045210.

[21] S. L. M. van Mensfoort, S. I. E. Vulto, R. A. J. Janssen, R. Coehoorn, Hole transport in polyfluorene-based sandwich-type devices: Quantitative analysis of the role of energetic disorder, Phys. Rev. B 78 (2008) 085208.

[22] W. F. Pasveer, J. Cottaar, C. Tanase, R. Coehoorn, P. A. Bobbert, P. W. M. Blom, D. M. de Leeuw, M. A. J. Michels, Unified description of charge-carrier mobilities in disordered semiconducting polymers, Phys. Rev. Lett. 94 (2005) 206601.

[23] S. L. M. van Mensfoort, R. Coehoorn, Effect of gaussian disorder on the voltage dependence of the current density in sandwich-type devices based on organic semiconductors, Phys. Rev. B 78 (2008) 085207.

[24] O. Zmeskal, S. Nespurek, M. Weiter, Space-charge-limited currents: An e-infinity cantorian approach, Chaos, Solitons and Fractals 34 (2007) 143 – 158.

[25] P N Murgatroyd, Theory of space-charge-limited current enhanced by Frenkel effect, Journal of Physics D: Applied Physics 3 (1970) 151.

[26] J. Scott, G. G. Malliaras, Charge injection and recombination at the metal-organic interface, Chemical Physics Letters 299 (1999) 115 – 119.

[27] P. R. Emtage, J. J. O'Dwyer, Richardson-schottky effect in insulators, Phys. Rev. Lett. 16 (1966) 356–358.

[28] Salleo, A. and Chen, T. W. and Volkel, A. R. and Wu, Y. and Liu, P. and Ong, B. S. and Street, R. A., Intrinsic hole mobility and trapping in a regioregular poly(thiophene), Phys. Rev. B 70 (2004) 115311.

[29] Gernot Paasch and Susanne Scheinert, Space-charge-limited currents in organics with trap distributions: Analytical approximations versus numerical simulation, Journal of Applied Physics 106 (2009) 084502.

[30] A. J. Campbell and D. D. C. Bradley and D. G. Lidzey, Space-charge limited conduction with traps in poly(phenylene vinylene) light emitting diodes, Journal of Applied Physics 82 (1997) 6326–6342.

[31] Y.-M. Koo, S.-J. Choi, T.-Y. Chu, O.-K. Song, W.-J. Shin, J.-Y. Lee, J. C. Kim, T.-H. Yoon, Ohmic contact probed by dark injection space-charge-limited current measurements, Journal of Applied Physics 104 (2008) 123707.

[32] S. C. Tse, S. W. Tsang, S. K. So, Polymeric conducting anode for small organic transporting molecules in dark injection experiments, Journal of Applied Physics 100 (2006) 063708.

[33] Alasdair J. Campbell and Donal D. C. Bradley and Homer Antoniadis and Mike Inbasekaran and Weishi W. Wu and Ed P. Woo, Transient and steady-state space-charge-limited currents in polyfluorene copolymer diode structures with ohmic hole injecting contacts, Applied Physics Letters 76 (2000) 1734–1736.

[34] M. A. Lampert, R. B. Schilling, Space-charge-limited current transient including diffusion, Phys. Rev. Lett. 18 (1967) 493–495.

[35] D. M. Goldie, Transient space-charge-limited current pulse shapes in molecularly doped polymers, Journal of Physics D: Applied Physics 32 (1999) 3058.

[36] A. Many, S. Z. Weisz, M. Simhony, Space-charge-limited currents in iodine single crystals, Phys. Rev. 126 (1962) 1989–1995.

[37] M. Simhony, A. Shaulof, Investigation of trapping in iodine single crystals by repeating carrier injection, Phys. Rev. 146 (1966) 598–600.

[38] D. Poplavskyy, J. Nelson, Nondispersive hole transport in amorphous films of methoxy-spirofluorene-arylamine organic compound, Journal of Applied Physics 93 (2003) 341–346.

[39] M. Z. Szymanski, I. Kulszewicz-Bajer, J. Faure-Vincent, D. Djurado, Transport properties of triarylamine based dendrimers studied by space charge limited current transients, Optical Materials 34 (2012) 1630 – 1634.

[40] M. Silver, P. Mark, D. Olness, W. Helfrich, R. C. Jarnagin, On the observation of transient space-charge-limited currents in insulators, Journal of Applied Physics 33 (1962) 2988–2991.

[41] Tessler, Nir and Preezant, Yevgeni and Rappaport, Noam and Roichman, Yohai, Charge Transport in Disordered Organic Materials and Its Relevance to Thin-Film Devices: A Tutorial Review, Advanced Materials 21 (2009) 2741–2761.

[42] H. Baessler, Charge transport in disordered organic photoconductors a monte carlo simulation study, physica status solidi (b) 175 (1993) 15–56.

[43] C. Tanase, E. J. Meijer, P. W. M. Blom, D. M. de Leeuw, Unification of the hole transport in polymeric field-effect transistors and light-emitting diodes, Phys. Rev. Lett. 91 (2003) 216601.

[44] Novikov, S. V. and Dunlap, D. H. and Kenkre, V. M. and Parris, P. E. and Vannikov, A. V., Essential Role of Correlations in Governing Charge Transport in Disordered Organic Materials, Phys. Rev. Lett. 81 (1998) 4472–4475.

[45] R. J. de Vries, S. L. M. van Mensfoort, V. Shabro, S. I. E. Vulto, R. A. J. Janssen, R. Coehoorn, Analysis of hole transport in a polyfluorene-based copolymer— evidence for the absence of correlated disorder, Applied Physics Letters 94 (2009) 163307.

[46] Y. Roichman, N. Tessler, Generalized einstein relation for disordered semiconductors— implications for device performance, Applied Physics Letters 80 (2002) 1948–1950.

[47] Wetzelaer, G. A. H. and Koster, L. J. A. and Blom, P. W. M., Validity of the Einstein Relation in Disordered Organic Semiconductors, Phys. Rev. Lett. 107 (2011) 066605.

[48] V. I. Arkhipov, E. V. Emelianova, Y. H. Tak, H. Baessler, Charge injection into light-emitting diodes: Theory and experiment, Journal of Applied Physics 84 (1998) 848–856.

[49] Genenko, Yu. A. and Yampolskii, S. V. and Melzer, C. and Stegmaier, K. and von Seggern, H., Charge carrier injection into insulating media: Single-particle versus mean-field approach, Phys. Rev. B 81 (2010) 125310.

[50] J. Staudigel, M. Stossel, F. Steuber, J. Simmerer, A quantitative numerical model of multilayer vapor-deposited organic light emitting diodes, Journal of Applied Physics 86 (1999) 3895–3910.

[51] M. J. Sharifi, Time-dependent simulation of organic light-emitting diodes, Semiconductor Science and Technology 24 (2009) 085019.

[52] K. Gustafsson, M. Lundh, G. Soderlind, A pi stepsize control for the numerical solution of ordinary differential equations, BIT Numerical Mathematics 28 (1988) 270–287. 10.1007/BF01934091.

[53] T. Chiba, K.-I. Nakayama, Y.-J. Pu, T. Nishina, M. Yokoyama, J. Kido, Hole mobility measurement of 4,4'-bis[n-(1-naphthyl)-n-phenylamino]- biphenyl by dark injection method, Chemical Physics Letters 502 (2011) 118–120.

[54] J. Graeme, Photodiode Amplifiers: OP AMP Solutions, McGraw-Hill, 1995.

[55] A. Szymanski, M. M. Labes, Charge carrier mobility in tetracene, The Journal of Chemical Physics 50 (1969) 1898–1899.

[56] M. Z. Szymanski, D. Djurado, Fast low current level measurements, Informatyka, Automatyka, Pomiary w Gospodarce i Ochronie Srodowiska 3 (2011) 46–49.

[57] M. Szymanski, D. Djurado, Dispositif de mesure de courant transitoire dote de moyens de compensation en courant (deposited on 11th july 2012 with number 12 56666), 2012.

[58] J. Louie, J. F. Hartwig, A. J. Fry, Discrete high molecular weight triarylamine dendrimers prepared by palladium-catalyzed amination, Journal of the American Chemical Society 119 (1997) 11695–11696.

[59] C. Cheung, W. Song, S. So, Role of air exposure in the improvement of injection efficiency of transition metal oxide/organic contact, Organic Electronics 11 (2010) 89 – 94.

[60] S. Tuladhar, D. Poplavskyy, S. A. Choulis, J. R. Durrant, D. D. C. Bradley, J. Nelson, Ambipolar charge transport in films of methanofullerene and poly(phenylenevinylene)/methanofullerene blends, Advanced Functional Materials 15 (2005) 1171–1182.

[61] K. K. Chan, S. Tsang, H. K. Lee, F. So, S. So, Charge injection and transport studies of poly(2,7-carbazole) copolymer pcdtbt and their relationship to solar cell performance, Organic Electronics 13 (2012) 850 – 855.

[62] Alasdair J. Campbell and Donal D. C. Bradley and Homer Antoniadis, Quantifying the efficiency of electrodes for positive carrier injection into poly(9,9-dioctylfluorene) and representative copolymers, Journal of Applied Physics 89 (2001) 3343–3351.

[63] Y. Shen, A. R. Hosseini, M. H. Wong, G. G. Malliaras, How to make ohmic contacts to organic semiconductors, ChemPhysChem 5 (2004) 16–25.

[64] H. S. Reehal, C. B. Thomas, Transient conduction characteristics of amorphous thin films of si 12 te 48 as 30 ge 10 in the pre-switching regime, Journal of Physics D: Applied Physics 10 (1977) 737.

[65] K. Eda, Transient conduction phenomena in non-ohmic zinc oxide ceramics, Journal of Applied Physics 50 (1979) 4436–4442.

[66] E. Knapp, B. Ruhstaller, The role of shallow traps in dynamic characterization of organic semiconductor devices, Journal of Applied Physics 112 (2012) 024519.

[67] M. Neukom, N. Reinke, B. Ruhstaller, Charge extraction with linearly increasing voltage: A numerical model for parameter extraction, Solar Energy 85 (2011) 1250 – 1256.

[68] M. Z. Szymanski, I. Kulszewicz-Bajer, J. Faure-Vincent, D. Djurado, Comparison of simulations to experiment for a detailed analysis of space-charge-limited transient current measurements in organic semiconductors, Phys. Rev. B 85 (2012) 195205.

[69] Knapp, Evelyne and Ruhstaller, Beat, Numerical analysis of steady-state and transient charge transport in organic semiconductor devices, Optical and Quantum Electronics 42 (2011) 667–677. 10.1007/s11082-011-9443-1.

[70] T. N. Ng, W. R. Silveira, J. A. Marohn, Dependence of charge injection on temperature, electric field, and energetic disorder in an organic semiconductor, Phys. Rev. Lett. 98 (2007) 066101.

[71] I. H. Campbell and B. K. Crone, Improving carrier injection in organic diodes by incorporating charge trapping molecules, Applied Physics Letters 88 (2006) 172113.

[72] Germs, W. Chr. and van der Holst, J. J. M. and van Mensfoort, S. L. M. and Bobbert, P. A. and Coehoorn, R., Modeling of the transient mobility in disordered organic semiconductors with a Gaussian density of states, Phys. Rev. B 84 (2011) 165210.

[73] G. Juska, K. GeneviCius, G. Sliauzys, A. Pivrikas, M. Scharber, R. Osterbacka, Double-injection current transients as a way of measuring transport in insulating organic films, Journal of Applied Physics 101 (2007) 114505.

[74] E. Pinotti and A. Sassella and A. Borghesi and R. Tubino, Electrical characterization of organic semiconductors by transient current methods, Synthetic Metals 122 (2001) 169–171.

[75] Horowitz, G, Organic thin film transistors: From theory to real devices, Journal of Materials Research 19 (2004) 1946–1962.

[76] Lawrence Dunn and Debarshi Basu and Liang Wang and Ananth Dodabalapur, Organic field effect transistor mobility from transient response analysis, Applied Physics Letters 88 (2006) 063507.

[77] Lawrence Dunn and Ananth Dodabalapur, Temperature dependent transient velocity and mobility studies in an organic field effect transistor, Journal of Applied Physics 107 (2010) 113714.

[78] Weis, Martin and Lin, Jack and Taguchi, Dai and Manaka, Takaaki and Iwamoto, Mitsumasa, Analysis of Transient Currents in Organic Field Effect Transistor: The Time-of-Flight Method, The Journal of Physical Chemistry C 113 (2009) 18459–18461.

[79] Yan Liang and Hsiu-Chuang Chang and P. Paul Ruden and C. Daniel Frisbie, Examination of Au, Cu, and Al contacts in organic field-effect transistors via displacement current measurements, Journal of Applied Physics 110 (2011) 064514.

[80] Satoshi Ogawa and Yasuo Kimura and Hisao Ishii and Michio Niwano, Carrier Injection Characteristics in Organic Field Effect Transistors Studied by Displacement Current Measurement, Japanese Journal of Applied Physics 42 (2003) L1275–L1278.

[81] Yan, X. Z. and Pawlas, J. and Goodson, T. and Hartwig, J. F., Polaron Delocalization in Ladder Macromolecular Systems, Journal of the American Chemical Society 127 (2005) 9105–9116.

[82] Trasatti, S, Pure Appl. Chem. 58 (1986) 955.

Electrochemical and chemical characterizations of triarylamine based dendrimer DT1Bu6

A.1. Chemical formula and synthesis

The synthesis of the triarylamine based dendrimer DT1Bu6 (formula and IUPAC name shown in fig.A.1.1) has been carried out by Prof. Irena Kulszewicz-Bajer at The Polytechnical University of Warsaw (Poland). This synthesis is highly inspired by the procedure published by J. Louie *et al*[58] with some noticeable modifications in order to provide the dendrimer with the six butyl peripheral groups. The synthesis is made in two steps the Di-(4-butylphenyl)amine is first prepared and the second step leads to the formation of the dendrimer.

Synthesis of Di-(4-butylphenyl)amine. 67.3 mg (0.3 mmol) of palladium acetate and 0.56g (0.9 mmol) of BINAP were dissolved in 2 ml of dry toluene under argon atmosphere and stirred for 30 min. at room temperature. Then, 2.34 mg (11 mmol) of 1-bromo-4-butylbenzene, 1.49g (10mmol) of 4-butylaniline, 1.44g (15mmol) of sodium *tert*-butoxide and 18 ml of toluene were added to the reactional flask. The mixture was heated up at 110°C and stirred for 4 hours. After cooling down the solution to room temperature, 30 ml of water are added and the organic phase was separated. The remaining aqueous phase was extracted three times with diethyl ether. The organic phases were combined and dried over MgSO4. The crude product was purified by chromatography on silica gel using a mixture CH2Cl2/hexanes (1:2) as an eluent to give 2.51g (8.9 mmol) of transparent oil (89% yield).

Synthesis of dendrimer DT1bu6. 0.927 g (3.3 mmol) of di(4-butylphenyl)amine (prepared as described above), 0.482 g (1mmol) of *tris*-4-butyl-phenyl)amine, 0.346g (3.6 mmol) of sodium *tert*-butoxide, 20.2 mg (0.09mmol) of palladium acetate and 54.6 mg (0.27 mmol) of *tert*-Bu3P were dissolved under an argon atmosphere. The reactional mixture was then heated up to 110°c and stirred for 12 h. The solution was cooled down to room temperature and washed with 30 ml of distilled water. The aqueous phase was extracted three 5 ml portions of diethyl ether. Then the combined organic phases were dried over MgSO4. After the removal of solvents, the crude product was purified by chromatography eluting with CH2Cl2/hexanes 1:2 wit 1%v/v of Et3N. Removal of the solvents followed by crystallization
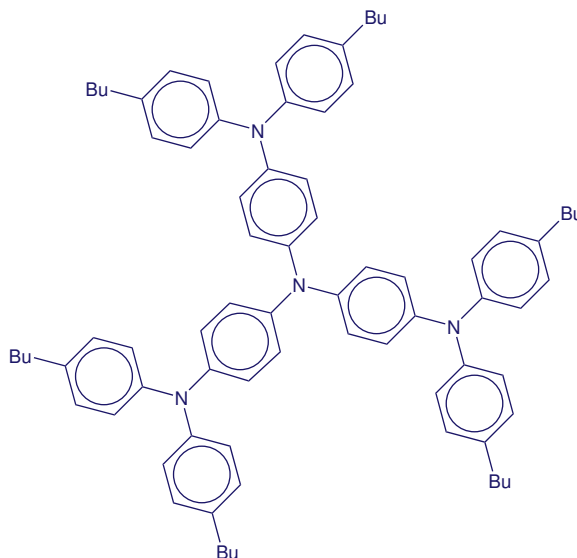
FIGURE A.1.1. *Chemical formula of N1,N1-bis(4-(bis(4-butylphenyl)amino)phenyl)-N4,N4-bis(4-butylphenyl)benzene-1,4-diamine (abbreviated as DT1Bu6)*

from THF/EtOH afforded titled compound as pale yellow powder (0.95g, 0.88 mmol, 88% yield).

A.2. Optical spectroscopy

Analysis by mass spectroscopy. The *analysis* of the dendrimer by mass spectroscopy without fragmentation revealed a very strong peak at 1082.8 g/mol for molecular ion M+. That well corresponds to the expected molar mass of the product. We should however note the presence of a second peak with a non negligible abundance for one mass of 1026.3 g/mol which indicate a weak presence of dendrimers on which is lacking one butyl chain.

IR spectroscopy. IR spectra were obtained by using a Perkin Elmer Paragon500 spectrophotometer. The IR spectrum recorded at room temperature is shown in fig. A.2.1. On this spectrum characteristic vibrational IR bands are evidenced.

UV-vis-NIR spectroscopy analysis as a function of oxidation degree.
Preparation of chemically oxidized material. One 0.041 mol.l-1 solution of DT1Bu6 in THF and one 0.041 mol.l-1 solution of Tris(4-bromophenyl)ammoniumyl hexachloroantimonate (BrC6H4)3NSbCl6 inacetonitrile were prepared. from these two solutions, one series of five samples are then prepared with successively from 0 to 4 equivalents in oxydizer. To do so, 20µl of the dendrimer solution are poured in five containers containing respectively 180 µl, 160 µl, 140 µl, 120 µl and 100µl of THF. The first container is the oxydizer free solution. The oxidizer solution is then added to the containers 2 to 5 per 20µl increments in order the desired equivalencies in oxidizer to be obtained.
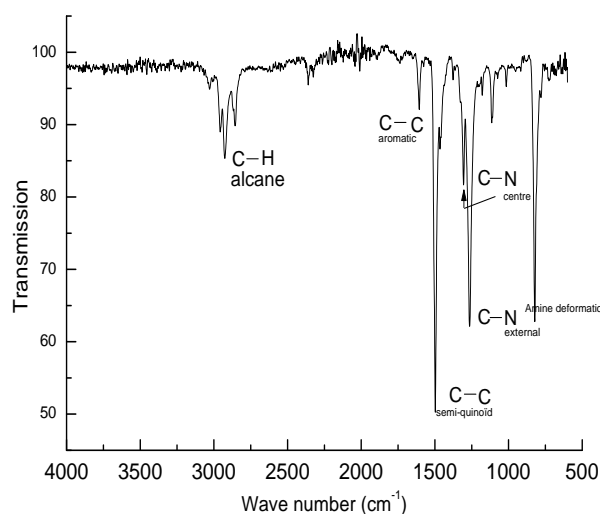
FIGURE A.2.1. *IR spectrum of DT1Bu6 recorded at room temperature with assignments of main vibrational modes*

UV-vis-NIR spectroscopy and electronic structure. The UV-vis-NIR spectra were recorded by using a Perkin Elmer Lambda900 spectrophotometer.

The obtained spectra as a function of the oxidation rate are shown in figA.2.2. First of all the intensity of the absorption band centered at 310 nm decreases and its position is slightly shifted towards towards UV when the oxidation rate is increased. The band centres at 345 nm disappears after the second oxidation only. By contrast a new absorption bands grows at 440 nm upon oxidation. The intensity of this band increases first for oxidation 2 and 3 and then decreases again. This band has already been observed in a triarylamine polymer[81]. In addition to this band another new relatively broad band grows in IR region (1110 - 1125 nm) upon oxidation. As previously a shift towards higher energies is observed when oxidation rate is increased. these features are fully consistent when considering DT1Bu6 as a semiconducting material. Thus the bands centered around 310 nm correspond to the pi-pistar transition. Upon oxidation some excited states are formed in the gap (likely polaronic like states according to an energetic diagrams schematized in fig. A.2.3. We have drawn a polaronic like band energy distribution in the gap because the band arising in IR region is quite broad and its shift towards high energies upon oxidation indication that populating these states induces an upward shift in the gap.

A.3. Electrochemical measurements

The electrochemical study was done on one 10-4M solution of dendrimer in anhydrous THF with Bu4NClO4 at 0.2M as the background salt. Cyclic voltammetry scans as a function of the width of potential window and of the sweeping rate have been carried out by using an
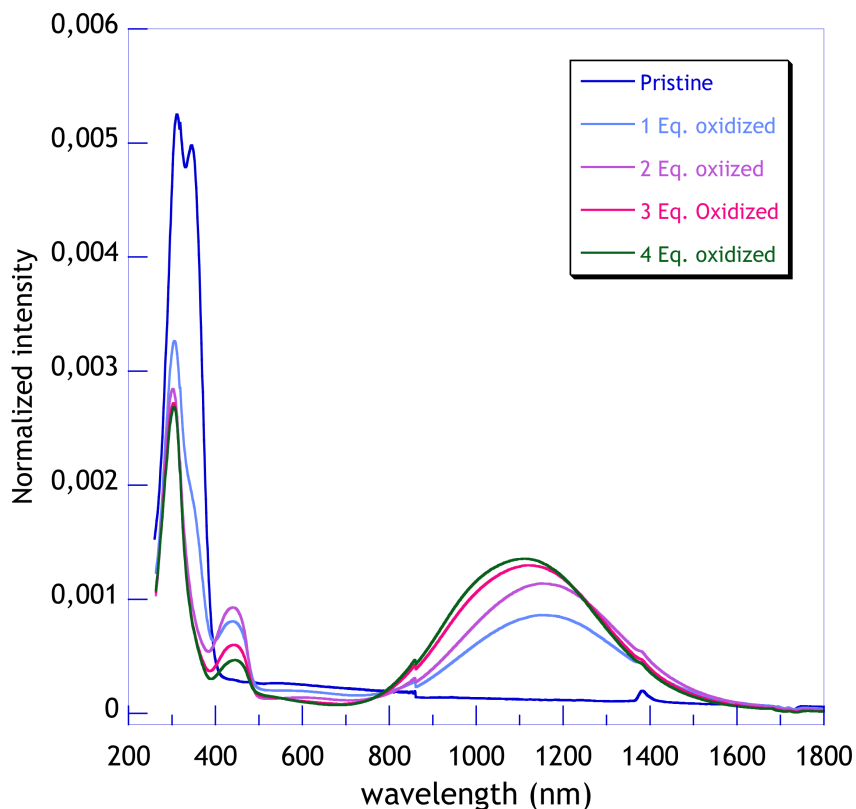
FIGURE A.2.2. *Room temperature UV-vis-NIR absorption spectrum of DT1Bu6 for different oxidation rates. (1Eq. Oxidized means 1oxidizer molecule per nitrogen atom)*
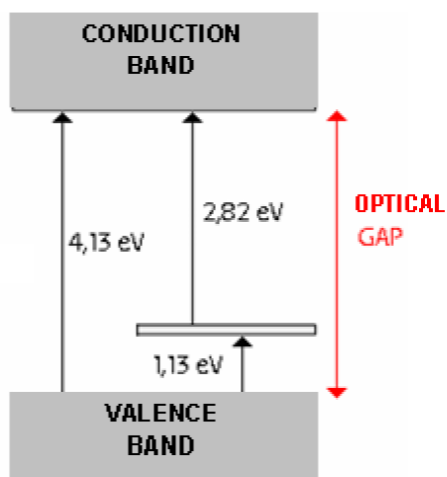

FIGURE A.2.3. *Electronic structure of DT1Bu6 as deduced from UV-vis-NIR spectroscopy.*

AUTOLAB potentiostat. We used a so-called three-electrode electrochemical cell provided with a Ag/AgCl reference electrode, one platinum wire as the working electrode and also one platinum wire as the counter-electrode.
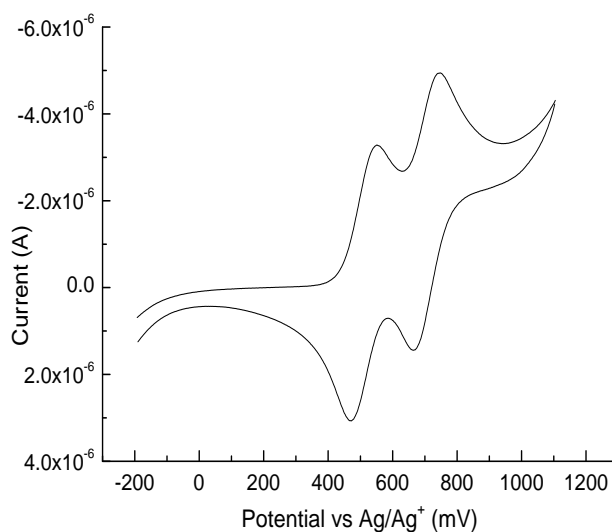
FIGURE A.3.1. *Cyclic voltammogram of DT1Bu6 (scan rate 15 mV/s)*

A typical cyclic voltammogram is shown in fig.A.3.1. It can be seen from this result that in these experimental conditions the dendrimer exhibits two reversible oxidation-reduction waves. the obtained oxidation potentials are E°1=487 mV and E°2=690 mV vs Ag/AgCl. We have checked that these potentials do not shift as a function of the scanning rate. From this result it is then possible to estimate the energetic positions of the HOMO level of DT1Bu6. To calculate the position of this level with respect to the vacuum level one must express the onset potential values on the absolute potential scale[82]. If the potentials are given with respect to the Ag/AgCl reference electrode the following expression can be used:

EHOMO = -(Eox onset + 4.4) eV

That gives -4.9 eV for the position of HOMO level of DT1Bu6.

APPENDIX B

Simulation program (dd2)

All of the simulated results presented in this thesis were obtained using dd2 drift-diffusion transport simulator, which was developed as a part of this work. This appendix is intended as a short introduction to dd2. The mathematical details of the simulator were already described in the chapter 3, and the physical models in use are described in chapters 1 and 2. Here, the program is shown from user's perspective on examples of some plots produced for the thesis.

The purpose of dd2 is unidimensional drift-diffusion simulation of electrical transport in thin organic films. The program is designed to calculate stationary and transient current responses reliably while being as simple and extensible as possible. Consequently, dd2 is written in Python and does not attempt to replicate any easily found functionality such as plotting and has no graphical user interface. This is compensated by the ease of combining it with any software for simulation, graphing or numerical optimization. Currently, only unipolar transport is supported, but can be generalized to bipolar transport easily. Any extension fitting in the framework of the unidimensional drift-diffusion approach is straightforward.

dd2 has been developed while working in CEA Grenoble and the author is in progress of obtaining a permission to distribute it. As soon as permission is obtained, information on how to get the program will be posted on

<div align="center">http://www.marekszymanski.com/dd2</div>

B.1. Running dd2

The dd2 can be used either as a standalone program or as a library. In the first case, it is executed using python interpreter

```
python dd2.py <inputfile>
```

where <inputfile> contains description of the requested calculations and the requested output. In order to avoid implementing yet another scripting language, the input file is a Python program itself. It is executed like any Python program, except that it has some conveniently set global symbols. Alternatively, dd2 can be used as an imported module.

In the fig. B.1.1, a comparison of standalone and module use are presented on a minimalistic example. In both cases, stationary space-charge-limited curve of 500nm thick sample is calculated. When dd2 input file is executed, useful symbols are set in the global space,

LISTING B.1. basic/minimum.inp

```
1  # Running:
2  # python dd2.py minimum.inp
3  Global(nx=500,dx=1e-9)
4  Param(HoleModel=ConstantMobility(mu=1e-9))
5  HoleContact(LocalThermalEquilibrium())
6  Output(file=stdout)
7  IVScan(linspace(0.,10.,11))
```

LISTING B.2. basic/minimum.py

```
1   # Running:
2   # python minimum.py
3   import dd2
4   from sys import stdout
5   from numpy import savetxt,linspace
6   c=dd2.Context()
7   c.Global(nx=500,dx=1e-9)
8   c.Param(HoleModel=c.ConstantMobility(mu=1e-9))
9   c.HoleContact(c.LocalThermalEquilibrium())
10  res=c.IVScan(linspace(0.,10.,11))
11  savetxt(stdout,res)
```

FIGURE B.1.1. Comparison of standalone (minimum.inp) and library (minimum.py) use of dd2.

including numpy and an instance of dd2.Context. When dd2 is used as library, dd2.Context, the internal object factory, must be handled manually.

B.2. Parameters

In dd2, coherent parameter naming is maintained. Parameters can be given in arbitrary case. Values are given for many parameters for illustration purposes, but they should not be relied on except for numerical paramaters. The parameters are set using the following functions:

Global(**kwargs). Sets global parameters. Once set, the values cannot be changed.

Param(**kwargs). General parameter setting function.

Tolerance(**kwargs). Function reserved for setting numerical parameters.

Output(**kwargs). Function reserved for settings output parameters.

Debug(**kwargs). Function reserved for troubleshooting options.

B.2.1. Physical parameters.

a. Intersite distance in meters, defining density of conduction states as a^{-3}. Used universally.

barriereV. Contact barrier in eV.

```
 1   #; −∗−Python−∗−
 2
 3   nx=1000
 4
 5   # Set number of points in the simulation grid. Note that currently
 6   # dd2 does not permit to change this parameter.
 7   Global(NX=nx)
 8
 9   # Set output file to 'scl.out'
10   Output(file='scl.out')
11
12   # Calculate IV curves for different sample thickness, which is
13   # set by the resolution of the computational grid, ...
14   for dx in [ 1e−10,1e−9 ]:
15       # ... and for different temperatures
16       for temperature in [ 3., 30., 300. ]:
17
18           # Set the parameters in dd2
19           Param(DX=dx,TEMPERATURE=temp)
20
21           # In the output, 'scl.out', precede each line by sample thickness
22           # (dx*nx) and by temperature
23           Output(prefix=[dx*nx,temp])
24
25           # Set the transport model for holes to constant mobility
26           # 10^−5 cm2/(Vs).
27           Param(HoleModel=ConstantMobility(mu=1e−9))
28
29           # Set contact model to ohmic contact
30           HoleContact(LocalThermalEquilibrium())
31
32           # Calculate IV curve for 121 geometrically spaced voltages
33           # from 1mV to 10V
34           IVScan(logspace(1e−3,10.,121))
```

FIGURE B.1.2. dd2 input file for simulation of stationary space-charge-limited current-voltage curves including diffusion. The results of this simulation are used in fig. 1.3.1.

epsi_r. Relative dielectric permittivity ϵ_r of the film.

holeelectrode0. Model of electrode at $x = 0$.

holeelectrode1. Model of electrode at $x = L$.

holelevels. Hole trapping levels.

holemodel. Transport model for holes (functional forms of μ and D).

noimage. Controls whether image potential contribution is taken into account in the local thermal equilibrium contact model.

B.2. PARAMETERS

LISTING B.4. trap/iv.inp

```python
1  #; -*-Python-*-
2
3  # Set sample thickness to 200nm, mobility to 10^-5 cm^2/(Vs) and
4  # ohmic contact.
5  Global(nx=200,dx=1e-9)
6  Param(HoleModel=ConstantMobility(mu=1e-9))
7  HoleContact(LocalThermalEquilibrium())
8
9  # Write calculated points to file instead of standard output
10 Output(file='iv.out')
11
12 # Calculate IV curves for several trap configurations.
13 for Npercm3,deptheV in [(1e-20,1.),(6.2e16,0.21),(6.2e16,0.33),(6.2e16,0.45)]:
14     # Define trap level. For stationary simulation, arbitrary trapping
15     # rate can be given.
16     Param(HoleLevels=[TrapLevel(Npercm3=Npercm3,deptheV=deptheV,trate=1.)])
17
18     # Calculate and output the IV curve
19     IVScan(logspace(1e-3,20,101))
```

FIGURE B.1.3. dd2 input file for simulation of stationary trap-controlled space-charge-limited current-voltage curves. The results of this simulation are shown in fig. 1.5.1.

mu. Mobility in $m^2/(Vs)$ for the constant mobility model.

mu0. Mobility prefactor in $m^2/(Vs)$ for the EGDM model.

sigmaeV. Gaussian disorder in eV.

temperature. Temperature in K.

v0. Value of potential $\phi(x = 0)$, in volts.

v1. Value of potential $\phi(x = L)$, in volts.

B.2.2. Numerical parameters.

abstolq. Absolute tolerance for charge density, in C/m^3. Set using Tolerance function.

abstolv. Absolute tolerance for voltage, in V. Set using Tolerance function.

dx. Resolution of computation grid in meters (Δx in fig. 3.2.1). Currently, this parameter can be set only once using Global function.

maxiter. Maximum number of iterations in Newton-Rhapson loop.

nx. Size of computational grid. Sample length $L = nx * dx$.

reltolq. Relative tolerance for charge carrier density. Set using Tolerance function.

```
1   #; −∗−Python−∗−
2
3   Global (NX=200,DX=1e−9)
4
5   # Calculate IV curves from 1mV to 10V for room temperature (default), constant
6   # mobility 10^−5 cm2/(Vs) and barrier values 0,0.1,0.2,...,0.7 eV using the
7   # Scott−Malliaras contact model defining current at boundary.
8   Output ( file='contact−scott .out ')
9   for bar in linspace (0. ,0.7 ,8):
10      Output ( prefix =[bar ])
11      Param (HoleModel=ConstantMobility (mu=1e−9))
12      HoleContact ( ScottMalliaras ( barriereV=bar ))
13      IVScan ( logspace (1e−3,10. ,121))
14
15  # Do the same thing using local thermal equilibrium model assuming Gaussian
16  # density of states. Note that in LocalThermalEquilibrium (...) only contact
17  # barrier is given and for the rest of parameters the default values are used.
18  Output ( file='contact−lte .out ')
19  for bar in linspace (0. ,0.7 ,8):
20      Output ( prefix =[bar ])
21      Param (HoleModel=ConstantMobility (mu=1e−9))
22      HoleContact ( LocalThermalEquilibrium ( barriereV=bar ))
23      IVScan ( logspace (1e−3,10. ,121))
```

FIGURE B.1.4. dd2 input file for simulation of injection-limited current voltage curves, using the Scott-Malliaras contact model(section 1.4) and the local thermal equilibrium model(section 2.4). The results of this simulation are used in fig. 1.6.1.

reltolv. Relative tolerance for voltage. Set using Tolerance function.

B.2.3. Output parameters. These parameters are set using Output function.

file. Output of simulation results. Can be None, stream or file name.

prefix. Additional columns to prepend to output rows.

B.2.4. Debug parameters.

printiterations. Controls if Newton-Rhapson iterations should be printed to stderr.

B.3. Models

When a model is created, it uses the currently set parameters (for example: temperarature) as the default values for unspecified parameters.

ConstantMobility(mu,temperature). $\mu = const$ transport model

EGDM(mu0,temperature,sigmaeV,a). Transport model given by eqs. (3.5.1) and (3.5.6).

121

```python
1   #; -*-Python-*-
2
3   # Set sample length to 1um, and temperature to 1K to minimize the diffusion.
4   Global(nx=1000,dx=1e-9,temperature=1.0)
5   # Mobility value and voltage are chosen so that L^2/(mu*V)=1
6   Param(HoleModel=ConstantMobility(mu=1e-15))
7   Voltage(1e3)
8
9   HoleContact(LocalThermalEquilibrium())
10  Output(file='many-rakavy.out')
11
12  for tau in [ 1e100, 10., 5., 3.0,2.0,1.5,1.25,1.0,0.75,0.5,0.25 ]:
13      Output(prefix=[tau])
14
15      # Constant average trapping time equal to tau is simulated by assuming
16      # large trap concentration. Detrapping is neglected by assuming very low
17      # trap release frequency.
18      Qperm3=1e6
19      trate=1.0/(Qperm3*tau)
20      Param(HoleLevels=[TrapLevel(Qperm3=Qperm3,trate=trate,rfreq=1e-50)])
21
22      # Use empty sample initial conditions
23      Zero()
24
25      # In order to avoid convergence problems, initial timesteps are shorter.
26      Transient(times=hstack((logspace(1e-10,0.01,20),linspace(0.01,5.,1001))))
```

FIGURE B.1.5. dd2 input file for reproduction of the classical Many-Rakavy illustration of transient space-charge-limited responses in the presence of trapping. The results of this simulation are used in fig. 1.7.1.

ScottMalliaras(epsi_r,barriereV,temperature,a). Contact model from ref. [26] (see section 1.4).

LocalThermalEquilibrium(epsi_r,barriereV,sigmaeV,a,noimage,temperature). Contact model given by eq. (2.4.1).

B.4. Functions

In addition to the previously explained parameter setting functions, the following functions are defined.

B.4.1. State function. The state of the simulation is the solution vector $\mathbf{x}$ as used in the section 3.3. The state is used and modified by the simulation functions. Otherwise, it is noramlly remembered.

Zero(). Loads zero state vector (corresponding to empty sample initial condition).

LISTING B.7. tran/barrier.inp

```
1   #; −∗−Python−∗−
2
3   Global (NX=200,DX=1e−9)
4   Output ( file ='barrier.out ')
5   Param(HoleModel=ConstantMobility (mu=1e−9))
6   Voltage (2.)
7   for bar in [ 0., .1, .2, .3, .4, .5 ]:
8       HoleContact(ScottMalliaras (barriereV=bar))
9       Output ( prefix =[bar])
10      Zero ()
11      Transient (times=linspace (1e−200,5e−5,201))
12  Output ( file ='barrier2.out ')
13  Param(HoleModel=ConstantMobility (mu=1e−9))
14  for bar in [ 0., .4 ]:
15      for v in [ 1., 2., 5., 10. ]:
16          HoleContact(ScottMalliaras (barriereV=bar))
17          Output ( prefix =[bar,v])
18          Zero ()
19          Transient (times=linspace (1e−200,5e−5,201))
```

FIGURE B.1.6. dd2 input file for simulation of space-charge-limited current transient responses in presence of contact barrier. The results of this simulation are used in figs. 1.7.2, 1.7.3.

Save(). Returns copy of current state vector.

Restore(x). Sets current state vector.

B.4.2. Simulation functions. All simulation functions use and alter the state vector. The results of simulation are returned as numpy array and can also be written according to output setup.

Stationary(). Calculates single stationary response.

IVScan(voltages). Calculates stationary responses for given set of voltages.

Transient(times). Calculated transient responses at given instants of time.

B.4.3. Utility functions.

Voltage(v). Sets external applied voltage to v. Parameter set: v0=0, v1=v.

HoleContact(c). Sets symmetrical hole injection contacts. Parameters set: holeelectrode0=c,holeelectrode1=c.

B.5. Usage examples

In the figs. B.1.2,B.1.3, B.1.4, B.1.5, B.1.6, B.1.7 input files used to generate various illustrations in the thesis are shown.

B.5. USAGE EXAMPLES

LISTING B.8. egdm/hostfig.py

```
1  def fig1iv(sigmaeV=None,mu0=None,maxv=None,n=81,barev=linspace(0.,1.,4)):
2      T=298.
3      Param(temperature=T)
4      Param(sigmaeV=sigmaeV,a=1.6e-9)
5      Param(HoleModel=EGDM(mu0=mu0))
6      for bar in barev:
7          HoleContact(LocalThermalEquilibrium(barriereV=bar))
8          Output(prefix=[bar])
9          IVScan(logspace(maxv*1e-4,maxv,n))
10
11 def fig2iv(sigmaeV=None,mu0=None,barev=linspace(0.,1.5,160)):
12     T=298.
13     Param(temperature=T)
14     Param(sigmaeV=sigmaeV,a=1.6e-9)
15     Param(HoleModel=EGDM(mu0=mu0))
16     Voltage(2.)
17     for noimage in [ False, True ]:
18         for bar in barev:
19             HoleContact(LocalThermalEquilibrium(barriereV=bar,noimage=noimage)
                   )
20             Output(prefix=[noimage,bar])
21             Stationary()
```

LISTING B.9. egdm/hostfig.inp

```
1  execfile('holstfig.py')
2
3  Global(NX=100)
4
5  Param(dx=1.02e-9)
6  Output(file='holstfig1a.out')
7  fig1iv(sigmaeV=0.075,mu0=4.8e-14,maxv=10.)
8  Output(file='holstfig1b.out')
9  fig1iv(sigmaeV=0.150,mu0=1.6e-16,maxv=10.)
10
11 Param(dx=0.22e-9)
12 Output(file='holstfig1c.out')
13 fig1iv(sigmaeV=0.075,mu0=4.8e-14,maxv=2.5)
14 Output(file='holstfig1d.out')
15 fig1iv(sigmaeV=0.150,mu0=1.6e-16,maxv=2.5)
16
17 Param(dx=0.22e-9)
18 Output(file='holstfig2a.out')
19 fig2iv(sigmaeV=0.075,mu0=4.8e-14)
20 Output(file='holstfig2b.out')
21 fig2iv(sigmaeV=0.150,mu0=1.6e-16)
```

FIGURE B.1.7. dd2 input files for reproduction of 1D continuum equation results presented in figs. 1 and 2 of reference [19].

124